FERMILAB-THESIS-1990-11
CDF/ANAL/MET/GROUP/1148
ANL-HEP-TR-90-30

A Measurement of the W Boson Mass in 1.8 TeV Proton–Antiproton Collisions

A thesis presented

by

William Trischuk

to

The Department of Physics

in partial fulfillment of the requirements

for the degree of

Doctor of Philosophy

in the subject of

Physics

Harvard University

Cambridge, Massachusetts

April, 1990

Abstract

I describe the measurement of the W mass using the electron data sample of the CDF detector's $1988-89$ $p\bar{p}$ collider run at the Fermilab Tevatron. I describe the calibration of the CDF detectors used in this measurement. I outline the extraction of the W mass, its statistical uncertainty and studies of the systematic uncertainties involved. The electron data yields: $m_W = 79.78 \pm 0.34(\text{stat.}) \pm 0.36(\text{sys.})$ GeV/c^2. When combined with other CDF measurements of the W and Z masses we measure $\sin^2\theta_W = 0.233 \pm 0.008$. I discuss the implications of this measurement on the Minimal Standard Model.

Contents

List of Tables

List of Figures

Acknowledgements

First of all I would like to thank Roy, whose position in the CDF collaboration gave me the opportunity to become involved with all aspects of the experiment. Then, there is Larry who gave me a home while Roy was building his accelerator. More than that he interested me in what, at first, seemed like a mundane measurement, but has become more interesting the harder we have looked. Of course there is George, who has taught me more about airline travel than I had ever imagined there was to know.

I thank Marge for teaching me about academic curiosity. Although we were always moving in opposite directions, she maintained an interest in my work no matter how far removed from her own. There is Rick who got me involved in the day-to-day operation of CDF and Steve (H.) who got me uninvolved again. Barry and Jimmy who always asked probing questions about my investigations, while asking the same hard questions of their own work and answering them. I thank Drew for teaching me the proper (lack of) respect for computers, Ed for the yearly basketball pool, Dave who kept me honest in physics and on a bike and Phil (S.) who was one of the few to help down to the wire.

It is impossible to properly thank all 250 members of CDF collaboration who have affected me in one way or another. From the collaboration management, all the way down to the guys on the trip to Texas, they have all played a role in this work. I wish to thank the University of Chicago High Energy Physics group for the use of their computers in doing the W mass simulation. Finally, I wish to thank the Natural Science and Engineering Research Council of Canada for funding much of my work at Harvard and on CDF.

I thank my parents for encouraging my independence. John for focusing my academic interests and steering me away from a career in management. Most of all, I thank Katey, for her understanding through all of the long hours that went into this work. She, more than anyone else, kept me believing that, despite all outward appearances to the contrary, I was enjoying myself.

THE CDF COLLABORATION

F.Abe[p], D.Amidei[d], G.Apollinari[k], G.Ascoli[g], M.Atac[d], P.Auchincloss[n], A.R.Baden[f], A.Bamberger[1], A. Barbaro-Galtieri[i], V.E.Barnes[l], T.Baumann[f], F.Bedeschi[k], S.Behrends[b], S.Belforte[k], G.Bellettini[k], J.Bellinger[r], J.Bensinger[b], A.Beretvas[n], P.Berge[d], S.Bertolucci[e],S.Bhadra[g], M.Binkley[d], R.Blair[a], C.Blocker[b], A.W.Booth[d], G.Brandenburg[f], D.Brown[f], A.Byon[l], K. L. Byrum[r], C. Campagnari[c], M. Campbell[c], R.Carey[f], W.Carithers[i], D.Carlsmith[r], J.T.Carroll[d], R.Cashmore[1], F.Cervelli[k], K.Chadwick[d], T.Chapin[m], G.Chiarelli[k], W.Chinowsky[i], A.Clark[d], S.Cihangir[o], D.Connor[j],M. Contreras[b], J.Cooper[d], M.Cordelli[e], M.Curatolo[e], C.Day[d], R.DelFabbro[k], M.Dell'Orso[k], L.DeMortier[b], P Derwent[c], T.Devlin[n], D.DiBitonto[o], F.Dittus[d], A.DiVirgilio[k], R. Drucker[i], J.E.Elias[d], R.Ely[i], S.Errede[g], B.Esposito[e], A. Feldman[f], B.Flaugher[n], E.Focardi[k], G.W.Foster[d], M.Franklin[f], J.Freeman[d], H.Frisch[c], Y.Fukui[h], A.Gauthier g, A.F.Garfinkel[l], S.Geer[f], P.Giannetti [k], N.Giokaris[m], P.Giromini[e], L.Gladney[j], M.Gold[i], K.Goulianos[m], H.Grassman[k], C.Grosso-Pilcher[c], C.Haber[i], S.R.Hahn[d], R.Handler[r], R.M.Harris[d], J.Hauser[d], T.Hessing[o], R.Hollebeek[j], L.Holloway[g], P.Hu[n], B.Hubbard[i], P.Hurst[g], J.Huth[d], H.Jensen[d], C.Jessop[f], R.P.Johnson[d], U.Joshi[n], R.W.Kadel[i], T.Kamon[o], S.Kanda[p], D.A.Kardelis[g], I.Karliner[g], E.Kearns[f], R.Kephart[d], P.Kesten[b], H.Keutelian[g], S.Kim[p], L.Kirsch[b], K.Kondo[p], U. Kruse[g], S.E.Kuhlmann[a], A.T.Laasanen[l], W.Li[a], T.Liss[g], N.Lockyer[j], F.Marchetto[o], R.Markeloff[r], L. A. Markosky[r], P.Maas[1], P.McIntyre[o], A.Menzione[k], T.Meyer[o],S.Mikamo[h], M.Miller[c], T.Mimashi[p],S.Miscetti[e], M.Mishina[h], S.Miyashita[p], S.Mori[p], Y.Morita[p], A.Mukherjee[d], L.Nakae[b], C.Newman-Holmes[d],J. Ng[f], L.Nodulman[a], R.Paoletti[k], A.Para[d], J.Patrick[d], T.J.Phillips[f], F.Photos[f], R.Plunkett[d], L.Pondrom[r], J.Proudfoot[a], G.Punzi[k], S.Ogawa[p], D.Quarrie[d], K.Ragan[j], G.Redlinger[c], J.Rhoades[r], F.Rimondi[d], L.Ristori[k], T.Rohaly[j], A.Roodman[c], A.Sansoni[e], A.Savoy-Navarro[1], V.Scarpine[g], P.Schlabach[g], E.E.Schmidt[d], M.H.Schub[l], R.Schwitters[f], A.Scribano[k], S.Segler[d], M.Sekiguchi[p], P.Sestini[k], M.Shapiro[f], M.Sheaff[r], M.Shibata[p], M.Shochet[c], J.Siegrist[i], P.Sinervo[j], J.Skarha[r], K.Sliwa[q], D.A.Smith[k], F.D.Snider[c], R.St.Denis[f], A.Stefanini[k], M.Takano[p], Y.Takaiwa[p], K.Takikawa[p], D.Theriot[d], P.Tipton[i], A.Tollestrup[d], G.Tonelli[k], W. Trischuk[f], Y.Tsay[c], F.Ukegawa[p], D.Underwood[a], R.Vidal[d], R.G.Wagner[a], R.L.Wagner[d], J.Walsh[j], T.Watts[n], R.Webb[o], T.Westhusing[k], C.Wendt[r], W.Wester[i], S.White[m], A.Wicklund[a], H.H.Williams[j], B. Winer[i], A.Yagil[d], A.Yamashita[p], K.Yasuoka[p], G.P.Yeh[d], J.Yoh[d], F.Zetti[k]

[a] Argonne National Laboratory- [b] Brandeis University- [c] University of Chicago
[d] Fermi National Accelerator Laboratory- [e] INFN, Laboratori Nazionali di Frascati, Italy
[f] Harvard University- [g] University of Illinois- [h] KEK, Japan
[i] Lawrence Berkeley Laboratory-[j] University of Pennsylvania
[k] INFN, University and Scuola Normale Superiore of Pisa, Italy- [l] Purdue University
[m] Rockefeller University- [n] Rutgers University- [o] Texas A&M University
[p] University of Tsukuba, Japan- [q] Tufts University- [q] University of Wisconsin
[1] Visitiors

Work supported by the U.S. Department of Energy, Division of High Energy Physics, Argonne National Lab, Contract W-31-109-ENG-38, and Harvard University, Contract DE-AC02-76ER03064.

Chapter 1

Introduction

This thesis describes the study of W bosons and their decay into electrons and neutrinos. We study the W bosons produced at the Fermilab Tevatron — a proton anti-proton ($p\bar{p}$) collider — during 1988 – 89. We measure the electrons from W decay with the Collider Detector at Fermilab (CDF). The key to the measurement is our understanding of the systematic uncertainties involved in measuring both the electron (e) and neutrino (ν) from the W decay. Our result is:

$$m_W = 79.78 \pm 0.34(\text{stat.}) \pm 0.19(\text{sys.}) \pm 0.30(\text{calib.}) \quad \text{GeV/c}^2. \tag{1.1}$$

where the second uncertainty is primarily on the neutrino measurement, while the third is the electron energy calibration uncertainty. The calibration uncertainty cancels in the ratio of W to Z masses when both are measured with the CDF detector. We improve the precision of the W mass measurement significantly when compared with previous measurements.

In some sense Fermi invented the W boson when he formulated weak interactions in the early 1930s. Pauli postulated the existence of a non-interacting particle, the neutrino, in the process of β decay and Fermi incorporated it in a theory of weak interaction currents inspired by electrodynamics. This included Fermi's introduction of a 4-point interaction responsible for nuclear β decay [1]. That such four point interactions are non-renormalizable led Schwinger and others (in the late 1950s) to propose massive charged bosons, which

eventually became the $W^{\pm}$, to mediate the interaction. The large mass was responsible for the apparent point-like interaction in β decay. Shortly thereafter Glashow incorporated these new particles (and one neutral partner — which became the Z^o) in a gauge theory, unifying the weak interactions with electromagnetism [2]. Unfortunately, the symmetry of Glashow's original theory required massless bosons. This was fixed in the late 1960s when Weinberg [3] and Salam [4] showed that massive bosons could be incorporated through the use of the Higgs mechanism [5].

At that time the model made definite predictions. The charged bosons were to have a mass of $70-80$ GeV/c^2, while their neutral partner was to have a mass of $80-90$ GeV/c^2. This mass scale was beyond the reach of any accelerators existing or planned in the early 1970s. Proposals were made, in the mid-1970s, to turn the large hadron accelerators (the SpS at CERN and the accelerator at Fermilab) into colliders. The European project, the $Sp\bar{p}S$ collider, was commissioned in late 1981 and shortly thereafter the UA1 experiment reported the discovery of the $W^{\pm}$ bosons [6]. The Tevatron collider was completed three years later with the commissioning of the accelerator and CDF in 1985. The first observation of W bosons, with CDF, occurred in 1987 [7] and a first high statistics investigation of electroweak physics took place in $1988-89$. This last run provides the data for this thesis.

Along with the discovery of the W boson came the first measurement of its mass: 81 ± 5 GeV/c^2 [6]. Subsequent running resulted in better determinations of the W mass coming from both CERN experiments. UA1 reports [8] :

$$m_W = 83.5 \pm 1.0(\text{stat.}) \pm 2.7(\text{sys.}) \quad \text{GeV/c}^2. \tag{1.2}$$

UA2 reports [9] :

$$m_W = 80.79 \pm 0.31(\text{stat.}) \pm 0.21(\text{sys.}) \pm 0.81(\text{calib.}) \quad \text{GeV/c}^2. \tag{1.3}$$

These can to be compared with the CDF electron result quoted in equation 1.1.

Figure 1.1 shows a typical W boson candidate decaying into an electron and neutrino. This picture illustrates the way we isolate a sample of W decays. The figure shows a high

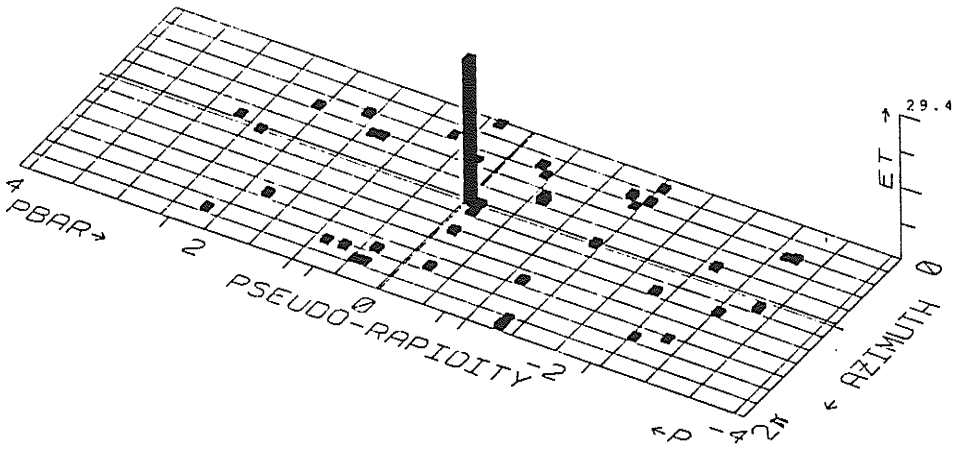

Figure 1.1: A W boson decaying into an electron and neutrino in the Collider Detector at Fermilab (CDF). The plot shows pseudorapidity ($\eta \equiv -ln\tan(\theta/2)$) vs. azimuth (ϕ) in the plane and transverse energy on the vertical scale. One signature of an electronic W decay is the apparent energy imbalance created by the escape of a neutrino with large transverse energy.

energy electron, contained in a single cell of the calorimeter, with no opposite activity to balance its momentum. W and Z decays are the primary source of electrons with energies above 20 GeV. Furthermore, the neutrino, from W decay, escapes undetected leaving an apparent transverse energy flow imbalance *. Figure 1.2 illustrates this, showing the correlation between electron and neutrino transverse energy, characteristic of the two body W decay candidates. We pursue this further in chapter 4 when the extraction of a W sample is described.

This thesis is organized as follows. Chapter 2 describes the theoretical predictions for the W mass as well as the Standard Model physics that can be inferred from its mass. Included there is a review of W production and decay at a $p\bar{p}$ collider. Chapter 3 describes the CDF detector, during the $1988-89$ data collection period, as it related to measuring W electron decays. Chapter 4 outlines the W event selection, reconstruction as well as the calibration of the tracking chamber and calorimeters used in the measurement of the W

*Although the conserved quantity is the momentum perpendicular to the beam direction the calorimeter measures the energies of particles, hence this effect is commonly referred to as missing transverse energy, $\not\!\!E_t$.

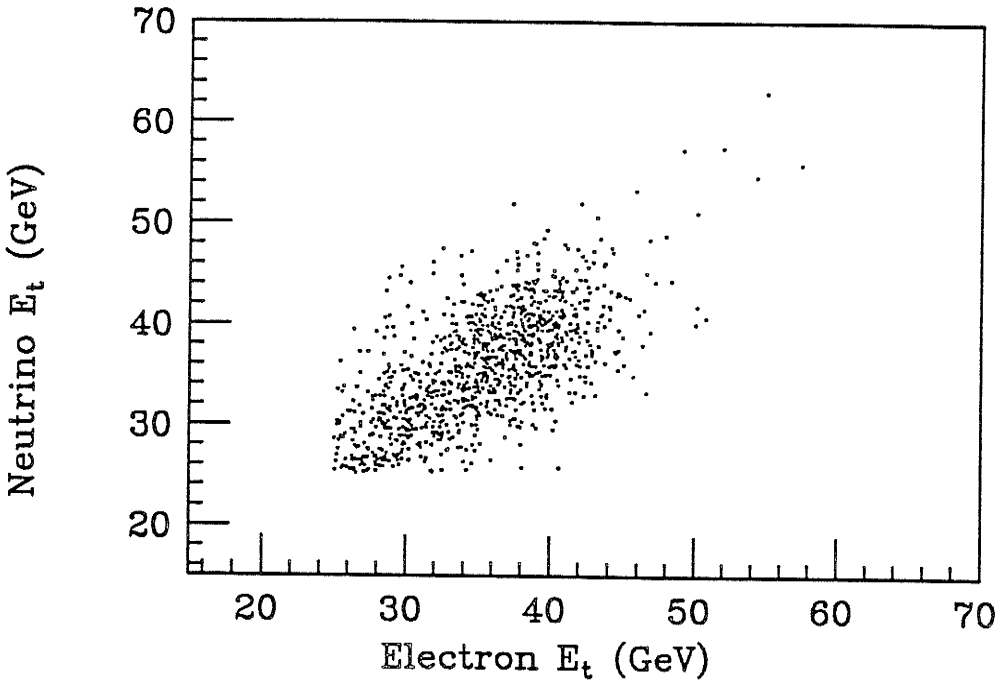

Figure 1.2: Correlation of electron transverse (to the beam direction) energy to the inferred transverse energy of the neutrino. The spectrum is cut at 20 GeV in both electron and neutrino transverse energy eliminating most of the background to W decay.

mass. Chapter 5 details the extraction of the mass value by comparing the data to Monte Carlo predictions. Emphasis is placed on the aspects of the model tuned using CDF data, as well as the details of the fitting procedure. The systematic uncertainties of the W mass measurement are described in Chapter 6. The work is summarized in Chapter 7, where Standard Model parameters (and their uncertainties) are extracted from this measurement and the Z boson mass.

Chapter 2

Standard Model Predictions for the W Mass

After Pauli introduced the neutrino to account for the distribution of electron energies seen in nuclear β decay Fermi postulated that the process could be described by a four point interaction [1] with coupling G_F. G_F has become known as the 'weak' coupling constant. Today the best determination of G_F comes from the decay of the muon [10] where it is found to be $G_F = 1.16632(4) \times 10^{-5}$ GeV^{-2}. When the four point interaction was replaced by the exchange of a W boson, the coupling, G_F, was replaced by: $g_W^2/(q^2 + m_W^2)$. For $q^2 \ll m_W^2$ (typical of β decay) this reduces to the relation:

$$m_W^2 = \frac{\sqrt{2} g_W^2}{8\, G_F}. \tag{2.1}$$

The electroweak unification ([2], [3] and [4]) led to relation:

$$g_W^2 = \frac{e^2}{\sin^2 \theta_W} \qquad [2]. \tag{2.2}$$

The electroweak mixing angle, θ_W, was measured in the middle 1970s in neutrino scattering experiments by comparing the rate of neutral current to charged current interactions (for a recent review see [11]). Early experiments [12, 13, 14] measured $\sin^2 \theta_W = 0.29 \pm 0.06$.

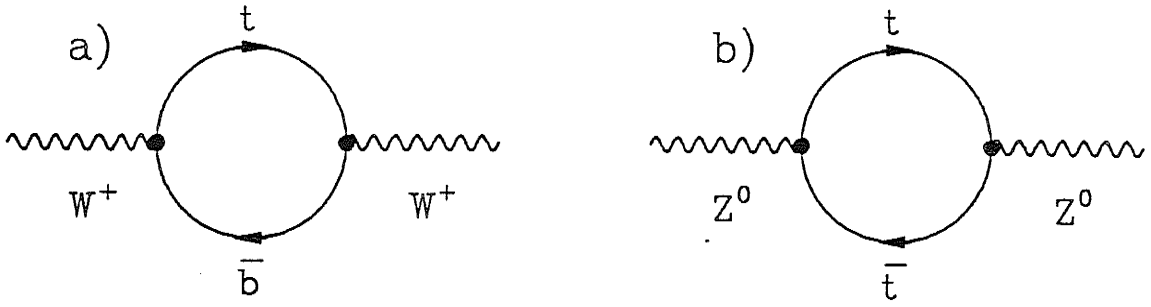

Figure 2.1: Feynman diagrams showing the first order corrections to the a) W and b) Z propagators introduced by the unknown top quark mass. The unknown top quark mass, m_t, emerges as a quadratic splitting between these two diagrams and changes the mass ratio $\frac{m_W}{m_Z}$.

Knowing this and the electromagnetic coupling ($\alpha^{-1} = 137.0359895(61)$ measured in atomic experiments) the GSW model predicted:

$$m_W^2 = \frac{\pi\alpha}{\sqrt{2}G_F \sin^2\theta_W} = (70 \pm 8\,\mathrm{GeV/c^2})^2. \tag{2.3}$$

Since the discovery of the W and Z bosons it has become customary [15] to express the weak mixing angle $\sin^2\theta_W$ as the ratio of the weak boson masses:

$$\sin^2\theta_W \equiv 1 - \left(\frac{m_W}{m_Z}\right)^2. \tag{2.4}$$

Such a definition is important when considering radiative corrections to the masses and couplings in the theory. The running of the electromagnetic coupling, α, contributes a sizeable correction to the predicted the W mass. Electrodynamics predicts that $\alpha(Q^2 = 100^2\,\mathrm{GeV}^2) \simeq 128^{-1}$ [16], a 7% correction from its value measured at $Q^2 \simeq 0$. Until recently these radiative corrections have been small compared to the experimental uncertainties associated with measuring them. Measurements are now sufficiently precise to make these corrections necessary [17].

Two first order corrections to the W and Z propagators are shown in figures 2.1 and 2.2. The top quark has not been found, its unknown mass appears in the evaluation of diagrams 2.1a and b and differentiates between the W and Z propagators. The dependence on

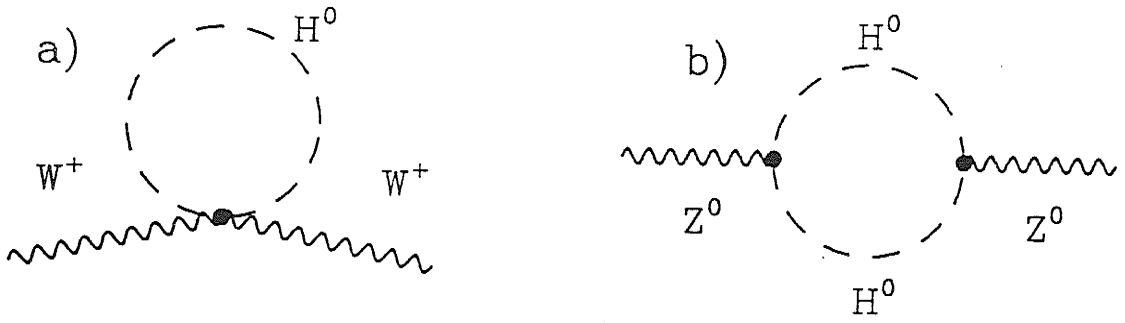

Figure 2.2: Feynman diagrams showing first order corrections to the a) W and b) Z propagators introduced by the unknown Higgs mass. Here the splitting is only logarithmic in the ratio $m_H/m_{W,Z}$ [18].

the top mass is quadratic [18]. The Higgs boson mass is also unknown *, but the coupling of a scalar to the vector bosons, shown in figures 2.2a and b, results in only logarithmic corrections to the couplings [18].

These radiative corrections can be expressed as a relationship between the W mass and three fundamental quantities of the electroweak theory α, G_F, and $\sin^2\theta_W$. The lowest order expression in equation 2.3 becomes:

$$m_W^2 = \frac{\pi\alpha}{\sqrt{2}G_F \sin^2\theta_W}\frac{1}{(1-\Delta r)} = \frac{(37.281\ \mathrm{GeV/c^2})^2}{\sin^2\theta_W(1-\Delta r)}. \qquad (2.5)$$

Δr accounts for the radiative corrections arising from the comparison of the W mass to the electroweak coupling constants α and G_F measured at low energy. The predicted dependence of these corrections on the top quark mass and the Higgs mass is shown in figure 2.3. The 7% shift, due to electromagnetic radiative corrections alone, is apparent as $m_{top} \to 0$. This is followed by the progressive, quadratic, cancellation of this correction (vanishing as $m_{top} \to 250$ GeV/c^2) along with the minor perturbation made by varying the Higgs mass from 30 GeV/c^2 to 1 TeV/c^2. Recent calculations, including the effect of higher order corrections, are discussed in [20].

*Recent experimental limits exclude a Standard Model Higgs with mass less than 24 GeV/c^2 [19]and the mathematical consistency of the Standard Model demands that the Higgs have a mass smaller than about 1 TeV/c^2.

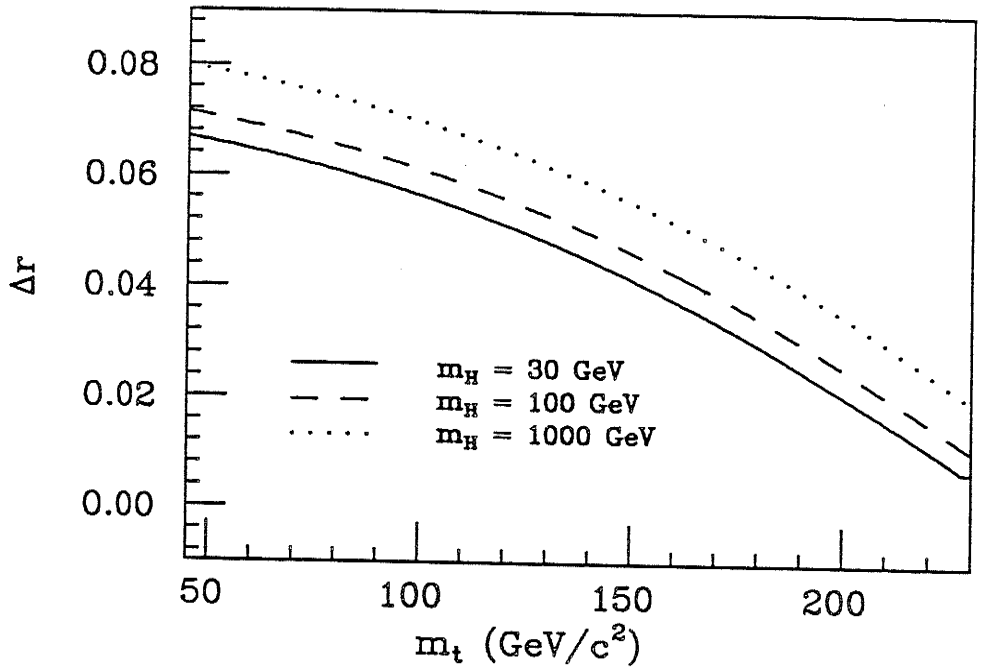

Figure 2.3: The quadratic dependence of Δr on the top quark mass, along with the logarithmic dependence on the Higgs mass gives one way of interpreting the measurement of the W mass within the context of the Standard Model.

In summary, we test the consistency of the Standard Model by comparing different measurements of the electroweak mixing angle. The contribution of this thesis is a precise determination of the $W^{\pm}$ boson mass and its comparison to other measurements of the electroweak coupling constants and Z boson mass. With reduced experimental uncertainties on the boson masses these comparisons constrain the Standard Model.

2.1 W Production in $p\bar{p}$ Collisions

To lowest order (in α_s) Ws produced in $p\bar{p}$ collisions come from the annihilation of a quark and an anti-quark. Figure 2.4a shows the Feynman diagram for the process:

$$q\bar{q} \rightarrow W. \tag{2.6}$$

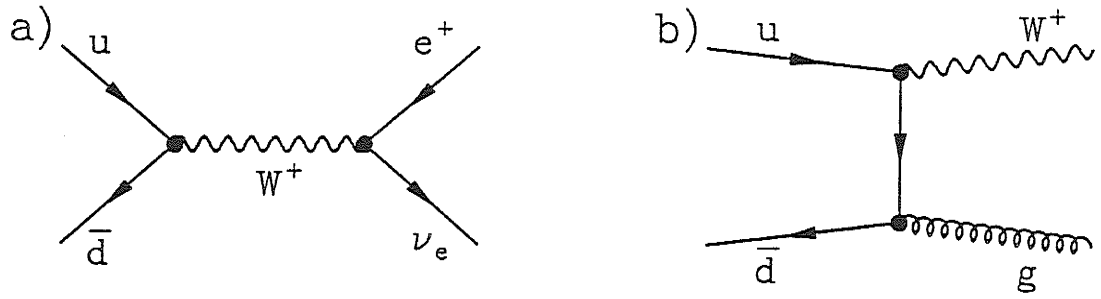

Figure 2.4: a) Feynman diagram from lowest order W production in $p\bar{p}$ collisions. Here a u quark from the proton and a $\bar{d}$ quark from the anti-proton annihilate to form a W^+ boson which subsequently decays into a positron and neutrino. b) One of many diagrams for higher order (in α_s) production of Ws in $p\bar{p}$ collisions. Here the W is produced in association with a single gluon (g).

This is complicated by the presence of several species of quarks in $p\bar{p}$ collisions. The differential cross-section can be written as a sum over quark species:

$$\hat{\sigma}(x_a, x_b) = \sigma_o \, x_a x_b \{\cos^2\theta_C[u(x_a)\bar{d}(x_b) + \bar{d}(x_a)u(x_b)] + \sin^2\theta_C[u(x_a)\bar{s}(x_b) + \bar{s}(x_a)u(x_b)]\}. \tag{2.7}$$

Here the u, d and s are the quark number densities in the proton ($\bar{u}$, $\bar{d}$ and $\bar{s}$ are similar quantities for the anti-proton), the x_i are the fraction of the (anti-)proton's momentum carried by the quarks and θ_C is the Cabbibo quark mass state mixing angle. The total W production cross section can then be written as:

$$\sigma(p\bar{p} \to W) = \int_0^1 dx_a \int_0^1 dx_b \, \hat{\sigma}(x_a, x_b) \quad \delta(x_a x_b - \frac{m_W^2}{s}). \tag{2.8}$$

Here the only constraints on the momentum fractions, x_i, are that they lie between 0 and 1, and they combine to give the W mass. They are inevitably unequal, giving the W a net longitudinal momentum: $p_{\text{long.}} = (x_a - x_b)\sqrt{s}$. This can be a large momentum, and in the case of $W \to e\nu$ unmeasured. Thus we concentrate on the event kinematics perpendicular to the beam. There is little motion in this direction before the collision (what there is comes from the Fermi motion of quarks inside the proton and initial state QCD radiation), so that after the collision the net transverse momentum should be small.

At low energies (for example $\sqrt{s} = 630$ GeV of the CERN collider) most Ws are produced in the collision of valence quarks from the proton and anti-proton. Only the valence quarks carry a sufficient fraction of the proton's momentum to produce an object with $m \sim 80$ GeV/c^2 (on average 1/8 of the proton's momentum is required of each quark). At the Tevatron the same is not true. The average momentum fraction carried by the quarks producing Ws is about 1/20. At these small fractions the relative abundance of sea quarks allows a larger portion of the Ws produced to come from the interaction of one or more sea quarks. The relative abundances are studied in reference [21] and shown in figure 2.5.

The primary effect of the admixture is on the polarization of the Ws. The W^+ boson (for example) is a spin one object decaying with an angular distribution of:

$$\frac{d\sigma}{d\cos\hat{\theta}} = \sigma_o\,(1-\cos\hat{\theta})^2. \tag{2.9}$$

Here $\hat{\theta}$ refers to the angle measured in the W centre of momentum frame (see figure 2.6) between the decay positron and the $\bar{d}$ quark in the collision. The u quark can come from either the proton (most likely) or the anti-proton (less likely). It is the relative importance of the sea quarks in the W production cross-section at the Tevatron which makes this an issue. Thus we include the resultant decay angular distribution:

$$\frac{d\sigma}{d\cos\hat{\theta}} = \sigma_o\,\{\,f(u_p)\,(1-\cos\hat{\theta})^2 + f(u_{\bar{p}})\,(1+\cos\hat{\theta})^2\,\}, \tag{2.10}$$

in our model of W production, where $f(u_p)$ $[f(u_{\bar{p}})]$ is the fraction of W^+s made from u quarks coming from the [anti-] proton. We define the ratio $f(u_{\bar{p}})$ / $[f(u_p)+f(u_{\bar{p}})]$ to be the "polarization", P, for later use in our W production model (see section 5.1). The relative importance of the sea quarks and their effect on the W decay angular distribution (via equation 2.10) is one of the differences seen between fit masses depending on the choice of proton parton distribution function (see section 6.2).

So far we have only described lowest order W production. One of the principle complications of the W mass measurement is the W transverse motion, p_t. We restrict ourselves to the study of Ws with small p_t. The production of Ws with finite transverse momentum

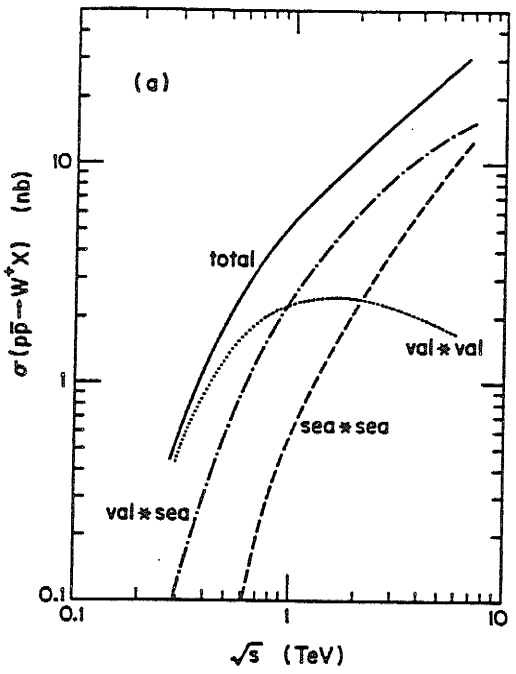

Figure 2.5: The W production cross section as a function of the $p\bar{p}$ centre of mass energy. The contributions from valence-valence, valence-sea sea-sea quark interactions are shown separately (from [21]).

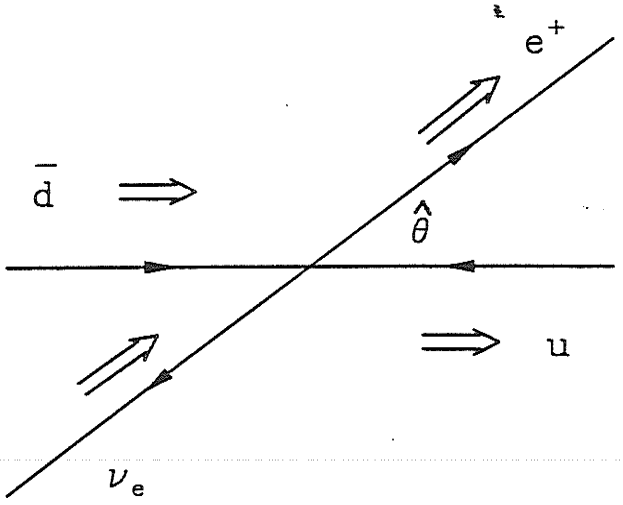

Figure 2.6: The polarization of the W resulting from valence quark production. Single arrows indicate the particle momenta and double arrows indicate the particle helicities. When $\hat{\theta}$ is measured as shown, equation 2.9 describes the W decay angular distributions.

is described by diagrams, like that in figure 2.4b, where one or more gluons are radiated as the W is produced. In principle, this process is calculable within the context of QCD, the theory of strong interactions. However, at low transverse momenta the gluons radiated are very soft and QCD calculations become unreliable [22]. Since detector resolution introduces effects at least as big as the uncertainties in such calculations we treat the study of W p_t phenomenologically. Here we make no attempt to relate our observations back to the QCD physics that produced the W p_t.

We study the W p_t to determine its effect on the energy distribution of the observed decay electrons. The W p_t can also effect W polarization, but this is of lesser importance to the mass determination. The decay angular distribution (averaged over charges [†]) is altered as follows:

$$\frac{d\sigma}{d\cos\theta} = \sigma_0\,(1+\cos^2\theta) \;+\; \sigma_1\,(1-3\cos^2\theta). \tag{2.11}$$

However, we expect only a 1% admixture ($\sigma_1 \simeq 0.01\,\sigma_0$) of this form. We conclude this from our predicted W p_t distribution (see chapter 5) and the calculations in reference [23]. Given that we study 10% variations of P (see equation 2.10 and subsequent text) by changing proton parton distributions (see section 6.2) and see no measurable effect on the W mass. Thus we ignore the effect of this depolarization.

Having produced the W, we now describe its decay into an electron and neutrino. As we have seen the electrons are produced with a distinctive decay angular distribution (equation 2.9). Averaging over charges (taking equation 2.11), and ignoring the complications of the W p_t we have:

$$\frac{d\sigma}{d\cos\hat{\theta}} = \sigma_0\,(1+\cos^2\hat{\theta}). \tag{2.12}$$

Our detection of W decay depends on the observation of a high E_t decay electron. We can re-write equation 2.12 in terms of E_t^e making use of the Jacobian for the change of variables from $\cos\hat{\theta}$ to E_t^e. Since the electron and neutrino are back-to-back, and of equal

[†]Oppositely charged Ws have opposite decay angular distributions. Averaging over charges we get: $\frac{1}{2}(1-\cos\hat{\theta})^2 + \frac{1}{2}(1+\cos\hat{\theta})^2 = 1+\cos^2\hat{\theta}$.

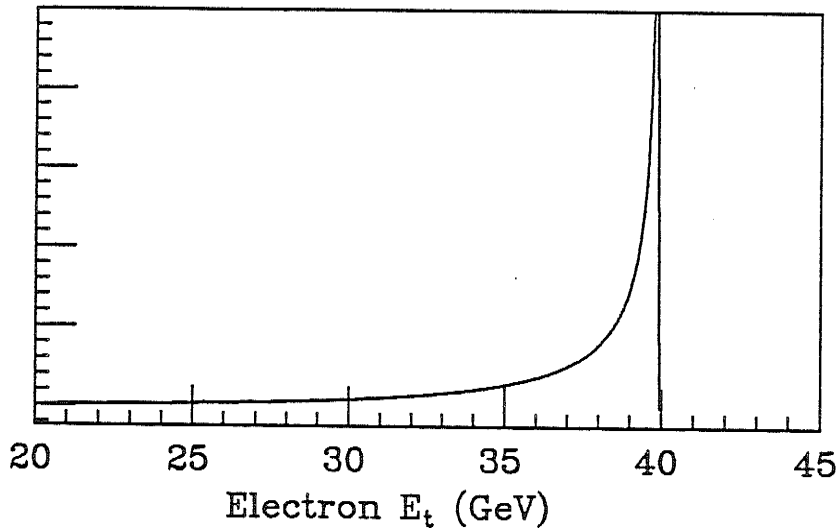

Figure 2.7: The ideal Jacobian distribution resulting from the two body decay of a vector particle.

momentum, in the W frame — a two body decay — we have (neglecting the rest mass of the electron):

$$\begin{aligned} \hat{E}^2 &= \frac{m_W^2}{4}, \\ \Rightarrow \hat{E}_t^2 &= \frac{m_W^2}{4}\sin^2\hat{\theta}. \end{aligned} \tag{2.13}$$

This leads to the Jacobian:

$$\frac{d\cos\hat{\theta}}{d\hat{E}_t^2} = \frac{-2}{m_W^2\cos\hat{\theta}}. \tag{2.14}$$

If we define v_t to be $\frac{2\hat{E}_t}{m_W}$ we are left with the familiar expression for the v_t:

$$\frac{d\sigma}{dv_t{}^2} = \frac{1}{2}\,\sigma_o\,\frac{2-v_t^2}{\sqrt{1-v_t^2}}, \tag{2.15}$$

which is shown in figure 2.7. This is the decay energy spectrum in the W frame. For Ws produced with no transverse motion we have $\hat{E}_t = E_t$ preserving the "Jacobian" shape in the lab frame. The finite W p_t, detector resolution and spread of generated masses over the Breit-Wigner resonance (see equation 5.1) smear out the singularity at $v_t = 1$ leaving a Jacobian peak of finite height. These effects are described, as they are built into our W model, in chapter 5.

While the E_t^e spectrum displays a Jacobian edge, it is smeared by the W p_t. By exploiting the inferred measurement of the neutrino, $\not\!\!E_t^\nu$, we can limit our sensitivity to this motion. We construct the transverse mass, m_t, of the electron-neutrino system:

$$m_t = \sqrt{2 \cdot E_t^e \cdot \not\!\!E_t^\nu \, [\, 1 - \cos(\phi^e - \phi^\nu)\,]}. \tag{2.16}$$

This is the three dimensional analog of the product of 4 vectors which give the full invariant mass. Since the neutrino's momentum along the beam is not measured [‡], the z components of the scalar product for the invariant mass are left out. To first order $m_t = 2E_t^e$ preserving the Jacobian nature of the E_t^e distribution. We exploit this feature to measure the W mass.

[‡]If a mass is assumed then p_z^ν can be determined up to the possible ambiguity of the two quadratic solutions the mass constraint implies.

Chapter 3

Detector and Data Collection

This chapter describes the CDF detector paying particular attention to the tracking chambers and calorimeters we use in the W mass measurement. The $1988-89$ data collection period is also described focussing on the triggers used to collect the W data.

The Collider Detector at Fermilab (CDF) is a 5000 T detector (shown in figure 3.1) built to study $p\bar{p}$ collisions [24]. The detector provides magnetic analysis of charged particles in the central region ($40^o < \theta < 140^o$), and hermetic calorimeter coverage to within 2^o of the beamlines ($2^o < \theta < 178^o$, $-4.2 < \eta < 4.2$) *.

3.1 Tracking Detectors

Closest to the beam pipe and nominal interaction point were a series of 8 Vertex Time Projection Chambers (VTPCs). These chambers measured charged particle tracks in the R-Z plane to within 3.5^o of the beam line. Covering a total length of 2.8 m along the beamline these chambers were used to identify the interaction vertex (or vertices) of the $p\bar{p}$ collision. In events with only one vertex its position was measured with σ = 1mm resolution [26].

*The CDF coordinate system defines the positive z-axis along the direction travelled by the protons. ϕ is the azimuthal angle around this axis and θ is the polar angle measured from the beam direction. Differences in $\eta(\equiv -ln\tan[\theta/2])$ are approximately Lorentz invariant, applicable to distributions in the polar angle variable (see also the caption of figure 1.1).

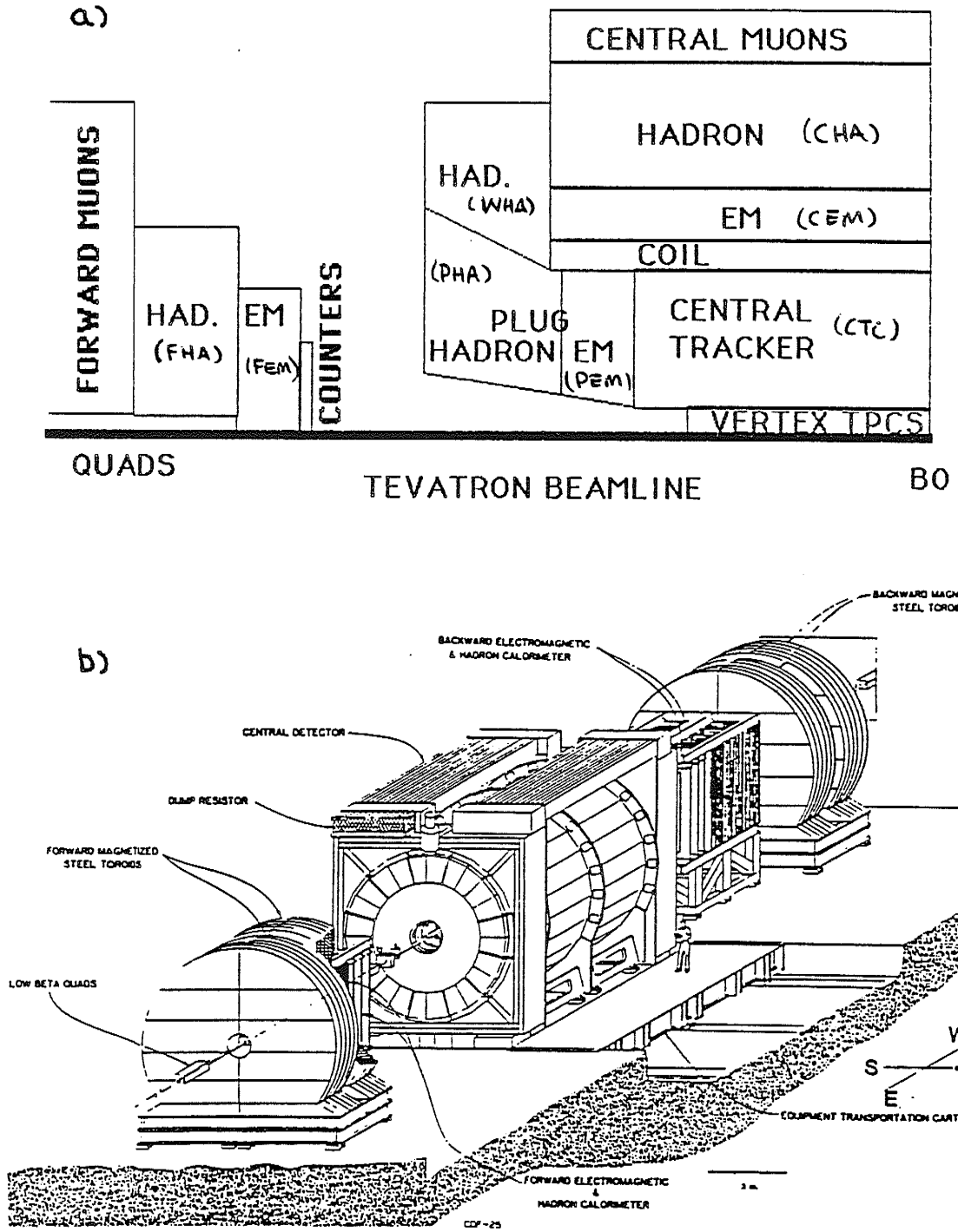

Figure 3.1: The CDF detector as configured during the 1988 – 89 run. The top figure is a cut away view of half of the detector. Closest to the interaction point (at the far right) are the VTPCs, surrounded by the CTC, the solenoid coil, and central EM and Hadron calorimeters. To the left are forward gas calorimeters and muon toroids. Below is an isometric view of the detector (from [25]).

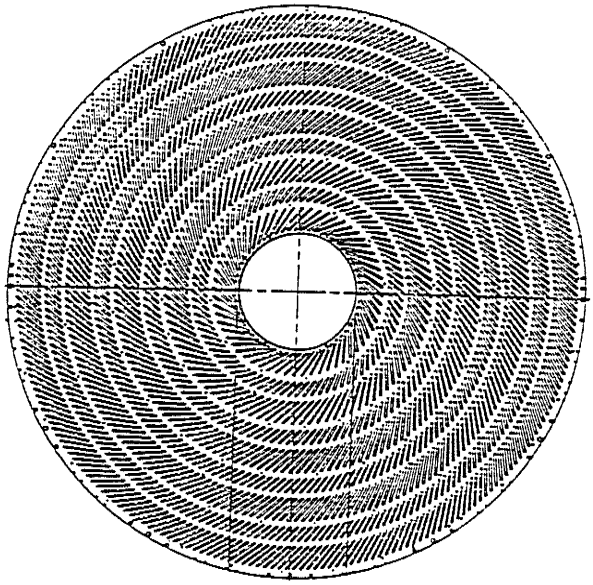

Figure 3.2: The layout of wires at the end of the central tracking chamber (CTC). The grouping into 9 superlayers, and the 45^o Lorentz angle can be seen.

In W events the vertex position is used as a reference to compute the transverse energy ($E_t \equiv E \sin[\theta]$) deposited in each calorimeter cell. The distribution of reconstructed vertices in candidate W events (figure 4.2) is well approximated by a Gaussian of mean 0 cm and sigma 30 cm. The spread in vertices reflects the beam's bunch length and collider β function, hence the collision point dispersion.

The Central Tracking Chamber (CTC) [27] surrounded the VTPCs. Both resided in a 1.4 T solenoidal magnetic field. The CTC was designed to measure charged particle tracks in the $R-\phi$ plane, to determine their curvature in the magnetic field, and thereby measure their transverse momentum. The CTC has 84 layers of wires grouped together in nine "superlayers" (see figure 3.2). Five of the nine have twelve sense wires parallel to the beam direction. These axial layers are used to determine the track curvature. The other four layers have 6 wires with 3^o stereo to provide the information necessary to determine the θ of the tracks. All superlayers have cells tilted at a 45^o angle with (see figure 3.2) respect to the radial direction. This compensates for the Lorentz angle of electron drift in the

magnetic field, allowing track ionization (electrons) to drift nearly azimuthally, simplifying the time-to-distance relationship.

The CTC alone provides a momentum resolution of $\frac{\delta p_t}{p_t} = 0.0020 \times p_t$ (where p_t is measured in GeV/c) for isolated tracks (such as W electrons). The addition of a vertex point ("beam constraint") extends the effective tracking radius from 1 m to 1.3 m, almost halving the effective resolution (which scales as $1/(B\,l^2)$) to $\frac{\delta p_t}{p_t} = 0.0011 \times p_t$. This improvement in resolution is important for the calibration of the calorimeters described in section 4.2. Complete tracking information is only available for $40^o < \theta < 140^o$, thereafter tracks do not pass through all layers of the chamber and the momentum resolution is degraded.

3.2 Calorimeters

The CDF detector includes three calorimeter systems (Central, Plug and Forward, see figure 3.1) to cover most of the solid angle around the interaction point. The central region ($-1.1 < \eta < 1.1$) of the calorimeter is made up of lead-scintillator electromagnetic shower counters (CEM) followed by an iron-scintillator hadron calorimeter (CHA and WHA). The desire to maintain constant angular sampling in η, as well as covering as much of the solid angle as possible led to the use of gas-proportional chambers as sampling devices outside the central region. Two systems — the plug electromagnetic (PEM) and hadronic (PHA) calorimeters (covering from $1.1 < |\eta| < 2.4$) and the forward electromagnetic (FEM) and hadronic (FHA) calorimeters (covering from $2.2 < |\eta| < 4.2$) — are installed in this region.

The Central Electromagnetic calorimeter (CEM) [24] is used to measure the energy of the W decay electron in this analysis. It consists of 31 layers of polystyrene scintillator interleaved with 30 layers of lead absorber. Including the outer tracking chamber wall, coil and calorimeter, 19 radiation lengths of material are presented to electrons. The calorimeter is broken up into 15^o wedges in ϕ (see figure 3.3). Light from the scintillators is read out through wavelength shifters on both sides of a wedge, in projective slices of the calorimeter

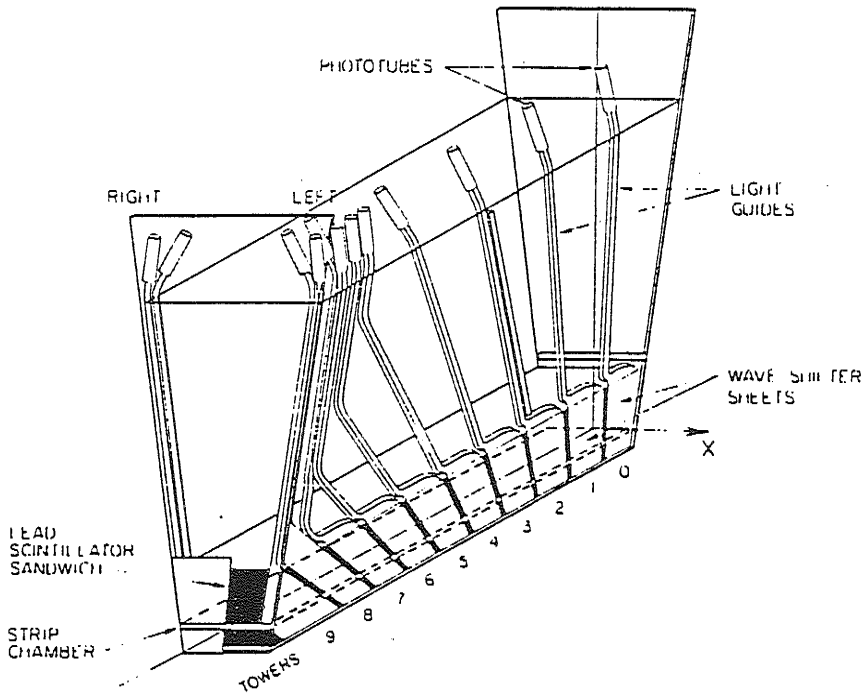

Figure 3.3: A cutaway view of a central electromagnetic calorimeter wedge. The wavelength shifters collect the light from the layers of scintillators delineate the tower structure in eta. Each wedge subtends 15^o in ϕ.

that cover 0.1 units of η. At a depth of 6 radiation lengths, a proportional chamber with fine grained (1.5 cm spacing) strip and wire readout helps localise electromagnetic showers. W electron showers are measured with 3 mm accuracy.

We initially calibrated each of the 478 CEM cells † with 50 GeV electrons in a test-beam. We preserved these calibrations by referring them to Cs^{137} source signals [28]. This provided a set of calibrations that was good to about 2.5% after many years (see figure 4.8a). We calibrate *in-situ* using electrons in the CDF $p\bar{p}$ collision data. These calibrations are the subject of section 4.2.

We use the entire CDF calorimeter to the infer the measurement of the neutrino coming from W decay. In this regard the central and wall hadron, plug and forward calorimeters play an important role. We calibrate these calorimeters in test-beams with electrons and pions. We tune the energy scales of the gas electromagnetic calorimeters with electrons available

†There are 48 wedges — giving 24 segments in ϕ and equivalent structures on each side of the collision point (see figure 3.1) — each having 10 individual cells. Two cells are not active to allow entry of the solenoid cryogenics.

from Z decay. We study the central hadron calorimeter with isolated charged pions in our $p\bar{p}$ data [29] (and see below in section 4.3). We study the other hadron calorimeters' response with jet data. In di-jet events little or no energy imbalance is expected. By studying di-jet events with one jet in the central calorimeter and the other in a gas calorimeter the relatively well known central energy scales are transferred to the gas. Jet fragmentation studies provide predictions for the fraction of jet energy that should be observed in the hadron calorimeters. Having previously tuned the electromagnetic calorimeters with Z data these predictions provide another check of relative hadron calorimeter calibrations. Finally, studies of spurious energy deposition in the gas calorimeters led to the implementation of software filters [30]. The measurement of the neutrino is improved by these "clean up" procedures [31] (see section 4.3 for further details).

3.3 Trigger

The interaction rate during the $1988-89$ run at the Tevatron collider was 10^5 times higher than the CDF data recording capability. It is important to be able to sift the interesting events from a plethora of "uninteresting" minimum bias events. We accomplished this with a four level trigger system during the $1988-89$ run [32]. A description of the triggers relevant to the collection of W candidates follows. The logic behind these triggers is shown schematically in figure 3.4.

The lowest level of the trigger — level 0 — selected potentially interesting crossings by requiring that time of flight counters on either side of the interaction region be hit. This trigger's decision was available within 100 ns of the beam crossing and inhibited data taking during the next beam crossing (one occurred every 3.5 μs) while the next trigger level finished its decision.

The level 1 trigger system computed the energy flow in both the electromagnetic and hadronic compartments of the calorimeter. For W electron candidates, all events fulfilled

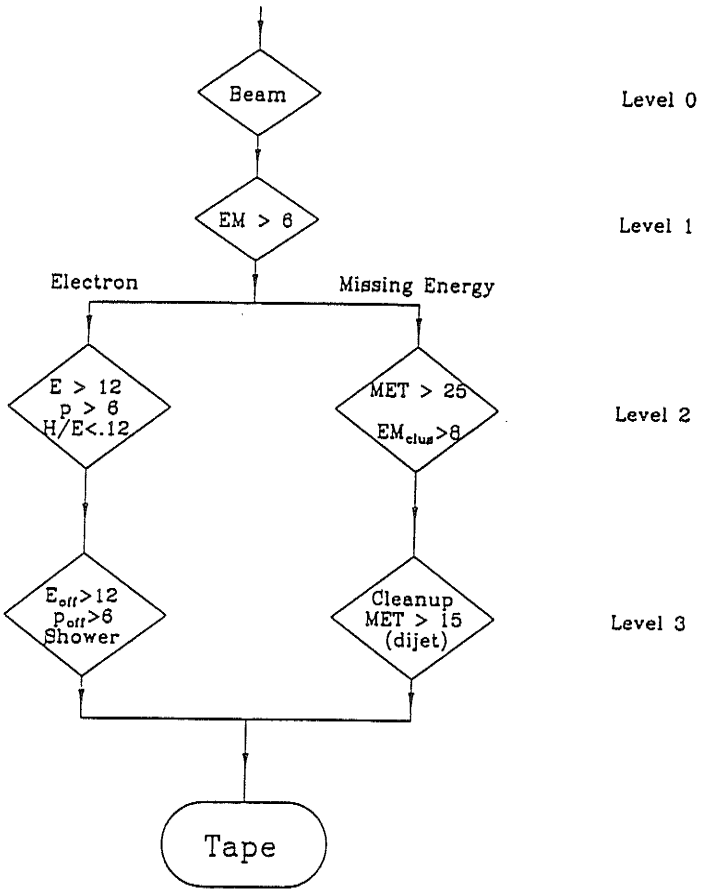

Figure 3.4: The logic behind the electron and $\not\!\!E_t$ triggers. The different trigger levels are highlighted. Note the prerequisite nature of the triggers from one level to the next.

the requirement that there be 6 GeV in a single trigger tower [‡] of the central electromagnetic calorimeter. This decision was made within 7μs. If no interesting physics emerged the front end electronics were reset, in time for the second crossing after the initial level 0 decision.

The level 2 trigger system was more sophisticated. It was first implemented at the beginning of the $1988-89$ run but evolved during that time. The triggers upon which this analysis relies were present for all of the data taking. With an average of 20μs, to make a decision, more analysis was possible at level 2. The electron and missing energy ($\not\!\!E_t$) triggers used to record W events are described in more detail.

[‡] A trigger tower covers two cells of the central calorimeter in the same wedge, 0.2 units of η and 15° in ϕ.

The second level trigger selected central electrons if: 1) a cluster of transverse energy [§] was found above 12 GeV, 2) a ϕ matched track (from a track processor [33]) pointed towards the cluster with $p_t > 6$ GeV/c, and 3) less than 12.5% of the energy in the cluster was in the hadronic compartment of the calorimeter. By studying events passing other triggers (such as the $\not\!\!E_t$ trigger described below) we found this trigger to be 98% efficient for central W electrons [34]. Comparisons of this trigger to lower threshold electron triggers revealled that it was fully efficient for $E_t > 15$ GeV [35]. The fact that the trigger exhibits no energy dependence thereafter leads us to conclude that this selection did not induce a bias in the W mass measurement which uses only electrons with $E_t > 25$ GeV.

We designed a backup trigger for W decay electrons to exploit the energy imbalance, characteristic of the escaping neutrino [36]. The net energy flow, computed at level 1, was required at level 2 to be greater than 25 GeV. There was also a requirement that there be at least one non-forward cluster ($|\eta| < 2.5$) with more than 8 GeV of the transverse energy in the electromagnetic compartment of the calorimeter. This last requirement removed spurious $\not\!\!E_t$ sources, which left apparent depositions of energy in the hadron calorimeters. All central W electrons satisfy the 8 GeV requirement. The $\not\!\!E_t$ requirement was too high to make this an inclusive trigger for W electrons — only 78% of W events are expected to have $\not\!\!E_t > 25$ GeV, and the effect of resolution on the trigger threshold reduced this acceptance even further — but the $\not\!\!E_t$ trigger provided an important check of the electron trigger's efficiency in regions of phase space where both should be very efficient ($E_t, \not\!\!E_t > 35$ GeV). The primary goal of the $\not\!\!E_t$ trigger was to search for non-Standard Model physics which are expected to leave large $\not\!\!E_t$ such as supersymmetry [37].

A level 3 trigger system was implemented during the 1988 – 89 running period. This consisted of a farm of sixty Motorola 68020 processors, each capable of running the complete CDF event reconstruction program. All of the raw data was available for decision making.

[§] An electron trigger cluster was formed by grouping the transverse energy in adjacent trigger towers of the EM calorimeter starting with a seed (of more than 4 GeV in a single tower) and stopping when the transverse energy of all neighboring towers fell below 3.6 GeV.

Due to execution time constraints we used streamlined versions of the reconstruction code to filter the events before they were written on tape. As the accelerator intensity grew over the course of the run, we added more filters to the level 3 system. By the end of the running period level 3 rejected about 60% of the events passing level 2.

The electron trigger ran for much of the data collection period with no level 3 requirement. During the latter part of the run we added the requirement that the electron cluster, identified in level 2, survive the offline reconstruction. With all the raw data available reconstruction occurred with more granularity than was available in the hardware trigger [¶]. The filter also required that there continue to be a 6 GeV/c track associated with the cluster after more sophisticated, but still two-dimensional, tracking.

The $\not\!\!E_t$ trigger was the first to include level 3 requirements. We discovered several sources of spurious energy imbalance in the 1987 CDF run. We fixed many of these, to some extent, in the hardware but they remained a non-negligible source of $\not\!\!E_t$ triggers. We developed filters to recognise depositions of energy likely due to noise in the detector and to remove this spurious energy. These procedures were executed in level 3 and the $\not\!\!E_t$ [‖] required to remain greater than 15 GeV. In this way only one $\not\!\!E_t$ threshold — the level 2 threshold – was imposed by the trigger. During the last third of the run we enhanced the $\not\!\!E_t$ filter to reject events with back-to-back jets; a significant source of $\not\!\!E_t$. If we detected the remnants of a second cluster within 30^o of back-to-back with the leading cluster, and it had more than 10 GeV of transverse energy, the event was removed as a likely di-jet mismeasurement. If the $\not\!\!E_t$ was greater than 40 GeV no di-jet veto was made. For W events this results in a small loss of data. The transverse energy distribution of jets associated with W decays shown below reveals that only 3% have the necessary energy and back-to-back configuration to fail this requirement. This will be discussed in more detail in section 4.3.

[¶]Signals from the two phototubes of each CEM cell quadruple the information available over what was available to the hardware trigger at levels 1 and 2. This allowed the energy sharing among cells (within the wedge) to be compared to that expected for electrons.

[‖]Like the level 2 $\not\!\!E_t$ computation, no event vertex was used, all events were assumed to come from $z = 0$ for the purpose of the trigger.

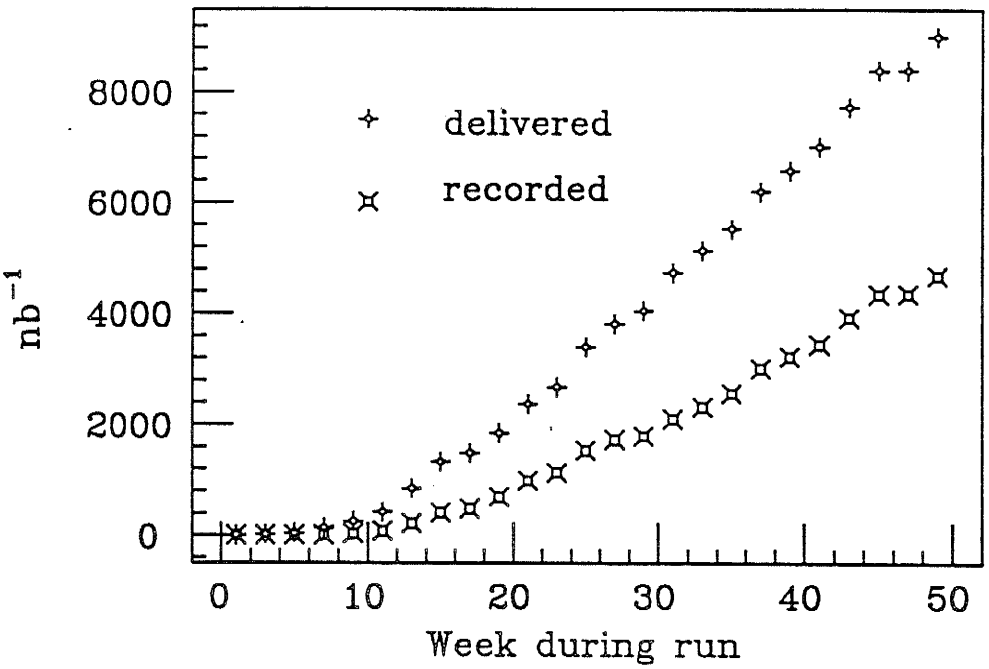

Figure 3.5: The integrated luminosity delivered by the accelerator (upper curve) and collected by the CDF experiment (lower curve). The difference reflects the data collection inefficiency of the experiment.

3.4 Data Collection

We collected the data used in this analysis over a 12 month period from June 1988 through May 1989. The peak machine intensity grew from initial value of 3×10^{29} cm^{-2} s^{-1} to over 2×10^{30} cm^{-2} s^{-1}. We used the first two months of operation to commission the first and second level triggers. The data used in this analysis comes from the last 10 months of the run, after the level 2 trigger was stable. The complexity of the detector and data acquisition systems limited the overall data collection efficiency to about 50% (see figure 3.5). We attribute some of this ($15 - 20\%$) to the higher than expected peak luminosities. At luminosities above 10^{30} collisions occur with significant probability ($10 - 15\%$) in consecutive beam crossings (every 3.5μs) while the level 1 trigger was only capable of making a decision in 7μs. The commissioning of the level 3 trigger and the data pipeline necessary to make it operational also contributed to the loss of efficiency, but the eventual rejection it provided made up for these losses.

Our overall trigger rate was limited to $1-2$ Hz by the speed we were able to transfer data to tape. Each event record contained 150 kbytes of information. Our final 4.4 pb^{-1} sample consists of 4×10^6 events recorded on 5 500 magnetic tapes. We followed data collection almost immediately by low-rate filtering which stripped out 1% of the most "interesting" events providing rapid feedback on trigger and detector performance as well as much of the physics analysis, including this measurement. This selection is the subject of section 4.1.1.

Chapter 4

Event Reconstruction and Detector Calibration

The selection of our $W \rightarrow e\nu$ event sample and the event reconstruction is discussed in this chapter. We include a description of the calibration of the detectors used to measure the W mass. This description is broken up into two parts: the calibration of the detectors we use to measure the electron's energy, and those we use to measure the underlying event – an important part of the neutrino's momentum.

4.1 Event Selection

Although we could not trigger solely on the $\not\!\!E_t$ signature of the neutrinos * from W decay, we based our final W event selection on the $\not\!\!E_t$ signature. The selection was a three pass process. During the first pass reconstruction and data filtering we selected an inclusive $\not\!\!E_t$ sample from the raw data-tapes. Next, we selected an inclusive W sample, by placing loose electron criteria on the $\not\!\!E_t$ events. Finally we selected those events used to measure the W mass, applying stricter criteria to improve our understanding of their measurement.

*At the trigger level the $\not\!\!E_t$ threshold was too high to allow for an inclusive W $\rightarrow$ e ν trigger. Offline we lower this threshold by adding other criteria.

4.1.1 Inclusive $\not\!\!E_t$ Sample

We reconstruct the energy flow in all raw data events to include the event vertex information, and require 1) the $\not\!\!E_t$ [†] be greater than 20 GeV. A Monte Carlo simulation shows that 95% of W events with an electron in our central detector satisfy this $\not\!\!E_t$ requirement[7], leaving only a small fraction of the original background. We further require 2) that the $\not\!\!E_t$ significance ($\not\!\!E_t/\sqrt{sum\ E_t}$) be greater than 2.4, a cut of more than 4σ in azimuthally symmetric ("minimum bias") events where the $\not\!\!E_t$ comes from measurement resolution alone (see figure 4.11 and discussion). Here "$sum\ E_t$" refers to the scalar sum of all the transverse energy in the event. This cut helps eliminate poorly measured di-jet events. Having a much larger cross section ($\approx 100\times$) than W production, di-jet events can have an apparent imbalance but will also have a relatively large $sum\ E_t$, reducing the significance (see figure 4.1).

We require 3) the events to have at least one cluster of energy with E_t greater than 15 GeV. Our "jet" clustering algorithm starts with seeds, single cells of the calorimeter, with energy greater than 3 GeV. It then adds to the cluster all cells within a cone of 0.7 radians (opening angle = $\sqrt{\Delta\eta^2 + \Delta\phi^2}$) having energy greater than 0.1 GeV, computing the energy weighted centroid of the cluster. The procedure iterates (starting with the centroid rather than seed cell) grouping energy inside the cone until the centroid stabilizes. Further details can be found in [31]. We require 4) the leading cluster to have at least 5% of its energy in the electromagnetic calorimeter to reduce the number of noise-like events with energy confined to a single detector. Finally, a requirement that there be 5) no cluster opposite the leading one, with $E_t \geq 5$ GeV, within 30° of azimuth reduces the residual di-jet background. Even when mismeasured, di-jet events generally leave some jet activity opposite the leading cluster of energy. We use these criteria to begin the selection of potential W candidates. We achieve a factor of 60 reduction from our initial data-sample. We are left with 65 000 events (from 4.4 pb^{-1}) and remain about 80% efficient for selecting W candidates which

[†] The details of the $\not\!\!E_t$ calculation are found in section 4.3, below.

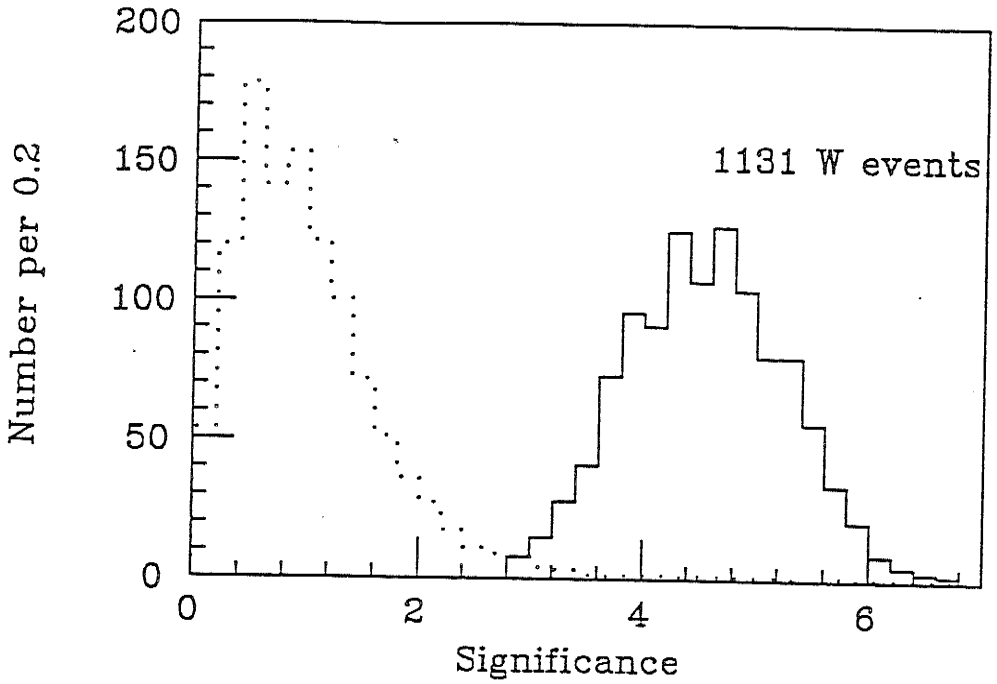

Figure 4.1: The $\not\!\!E_t$ significance (described in the text) for a sample of di-jet events (dotted histogram) and our W sample (solid histogram). This comparison shows how we remove events which have substantial $\not\!\!E_t$, but also a large *sum* E_t. The relative normalizations of the samples is arbitrary.

leave an electron in our central detector [7]. This event sample also lends itself to searches for exotic physics processes which leave large $\not\!\!E_t$ [37].

4.1.2 Inclusive W Sample

To isolate a W sample from the inclusive $\not\!\!E_t$ events we make some requirements on the electron. To ensure that we have a well measured electron we restrict ourselves to events with electron candidates depositing their energy in the central calorimeter. Our requirements are as follows. 1) We only accept events whose highest energy cluster is located in the central detector ($|\eta| \leq 1.0$). 2) The fraction of that cluster's energy in the electromagnetic compartment must be greater than 85%. Finally, 3) we require a track of momentum, P, pointing at the cluster with E/P $\leq$ 2. These last two requirements are easily satisfied by real electrons (see for example figure 4.3a and figure 4.9). These requirements produce our inclusive central W electron sample of 3400 events. Figure 4.2 shows the vertex distribution

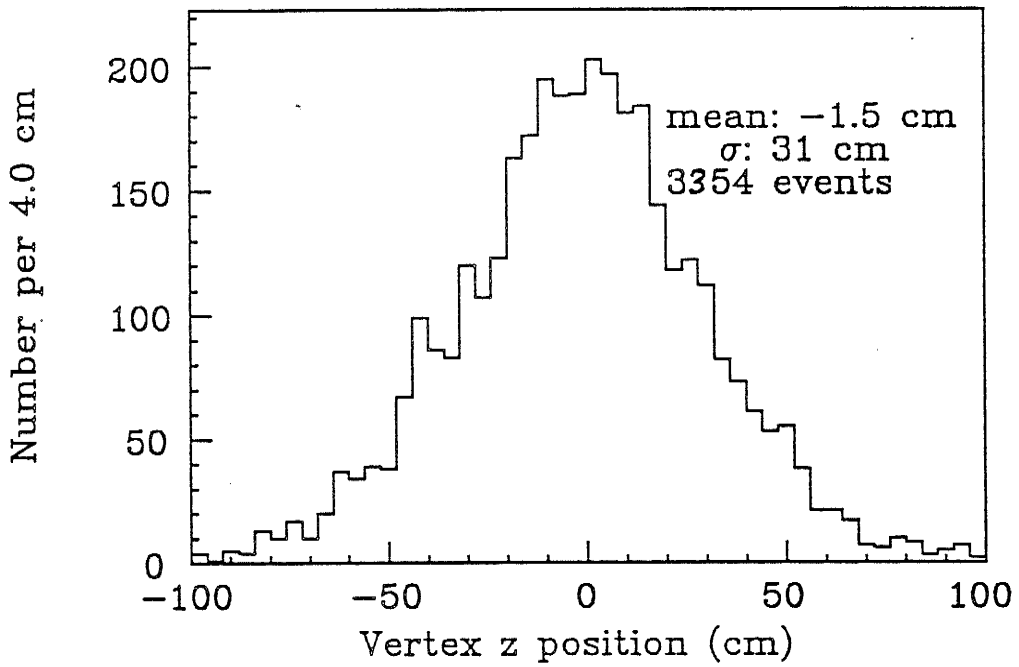

Figure 4.2: The event vertex distribution (along the beam line; z) for the inclusive W decay candidates. Note that interactions can occur up to one meter from the nominal interaction point. These events are not hermetically contained by the calorimeter and must be removed from the final event sample, we require $|z| \leq 60$ cm.

for these events.

4.1.3 W Mass Sample

We apply further cuts to obtain a sample suitable for measuring the W mass. Because significant QCD backgrounds persist at low E_t, we make more stringent cuts of 1) $E_t^e \geq 25$ GeV and 2) $\not\!\!E_t^\nu \geq 25$ GeV. Doing this we lose 20% of the inclusive Ws. Being at low E_t^e these do not contribute significantly to the measurement of the W mass (see section 6.5). Restricting ourselves to higher energy electrons reduces residual backgrounds. By studying the fraction of photon conversion candidates which pass these cuts we deduce that background in our mass sample was reduced from 4% to less than 1% [38]. We make fiducial cuts on the electron to ensure that its shower is well within the active part of the calorimeter. We require the centroid of the strip chamber shower associated with the electron be 3) more than 1.5^o away from central wedge boundaries, 4) 12 cm or further from the arch

separation at 90° and 45 cm away from the central-plug boundary of the calorimeter. To reduce the probability of a high p_t parton escaping detection completely we 5) accept only events whose vertex is within 60 cm (2σ) of the nominal interaction point (see figure 4.2). We reduce backgrounds further by rejecting events where 6) a soft track accompanies the candidate electron track making an apparent low mass pair (indicative of a photon conversion). We also demand that electron candidate tracks have sufficient hits in the VTPC (inside the CTC) to further reduce the background from photon conversions in the material between VTPC and CTC. This costs us less than 3% of the candidates. Studies of identified conversions in parts of the detector where there is little or no material (to cause real conversions) [39] indicate that our loss is consistent with all of these events being good electrons. 7) The requirement that one, and only one, track be pointing at the electron seed cell reduces the sample a further 3%. Finally, we 8) require that there be no stiff tracks (other than the electron track), with $p_t \geq 10$ GeV/c, in the event. We find two such tracks (in different events) with $p_t \geq 40$ GeV/c and no others. These are consistent with being $Z \rightarrow e^+e^-$ candidates where one of the electrons was lost in a crack of the calorimeter. This leaves us with 1 700 events in our sample. The electron characteristics of these events are shown in figure 4.3.

We make two other cuts to get the final mass sample. After studying the effects of internal and external radiation (see section 4.2) on the energy-momentum matching of electrons [42] we restrict further study to electrons with E/P $\leq$ 1.4. This limits the radiative correction in the energy scale (see section 4.2). Further, we choose to study a sample of W electrons which has little or no other coherent energy flow (ideally no other energetic prompt partons). To reduce our sensitivity to such partons we restrict ourselves to events with no calorimeter energy clusters (other than the electron) with E_t(jet) > 7 GeV (see figure 4.4). Even with this cut our measurement of this additional energy is one of the limiting factors in the W mass precision. This is discussed in section 6.3.

We are left with 1131 electron events after applying these last two cuts. We also have

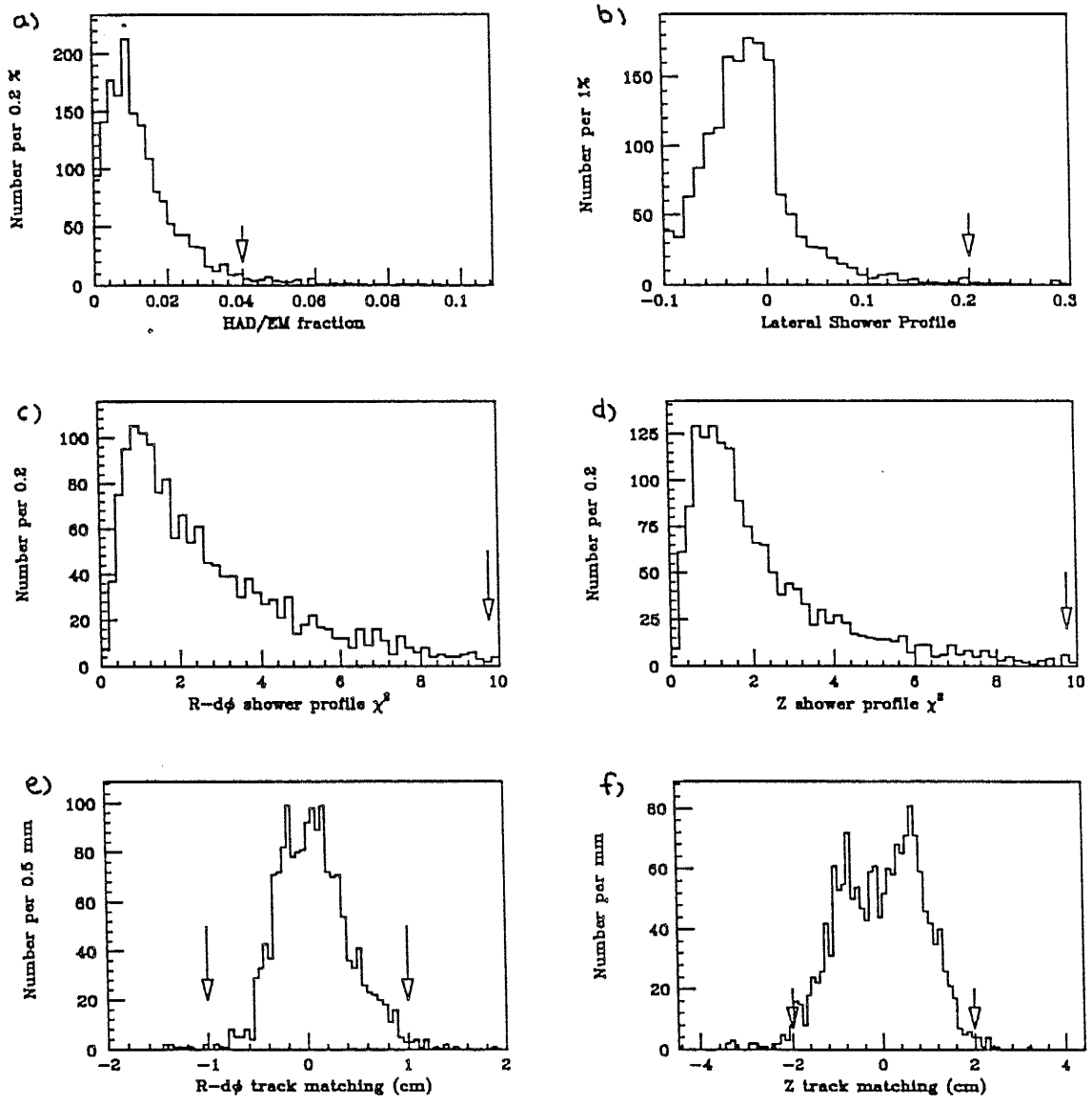

Figure 4.3: Six different variables used in the inclusive electron search plotted for our $W \rightarrow e\nu$ mass sample. The arrow in each figure shows a typical cut in each variable. The $\not\!\!E_t$ signature along with very "loose" electron cuts (E/P $\leq$ 2, and HAD/EM $\leq$ 0.15) are sufficient to produce this sample. We use distributions like these to determine the efficiency of these cuts when applied in other analyses [35, 40, 41].

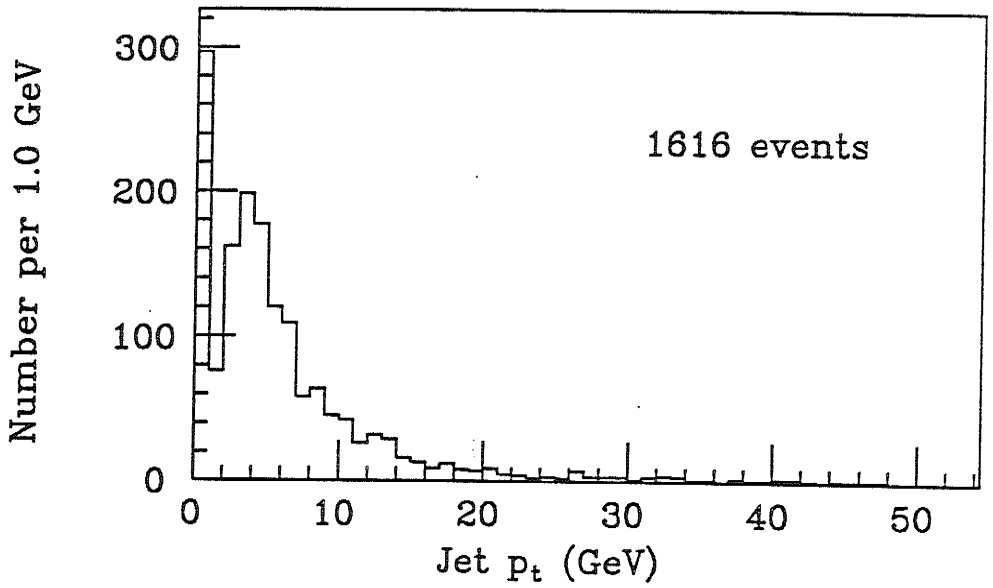

Figure 4.4: The "jet" p_t spectrum associated with electron W candidates. Attempting to measure extra partons (responsible for such jets) degrades the neutrino resolution. We cut out all W candidates with associated jets above 7 GeV/c p_t. Our jet clustering threshold is about 5 GeV, the spike at 0 represents W events where no jet cluster is found.

a sample of $W \rightarrow \mu\nu_\mu$ candidate events. The detailed selection of these events [43] is different from the electron candidates, however the final kinematic selections ($p_t^\mu > 25$ GeV/c, $\not\!\!E_t > 25$ GeV and $E_t(\text{jet}) < 7$) are the same, producing a comparable sample and allowing a parallel mass analysis. These are the event samples we use to measure the mass of the W boson. The calibrations done to improve the electron and neutrino energy measurements are described in the next two sections.

4.2 Electron Energy Corrections

We use the central electromagnetic calorimeter to measure the energy of the electrons in our sample. The testbeam calibration [28] provides a good starting point for the calibration of the calorimeter, but further fine tuning is possible with the sample of electrons in our data. Our aim is to use electrons in our data as a source of well measured particles with which to calibrate the detector. Although we set the energy scale with the electrons in the W sample,

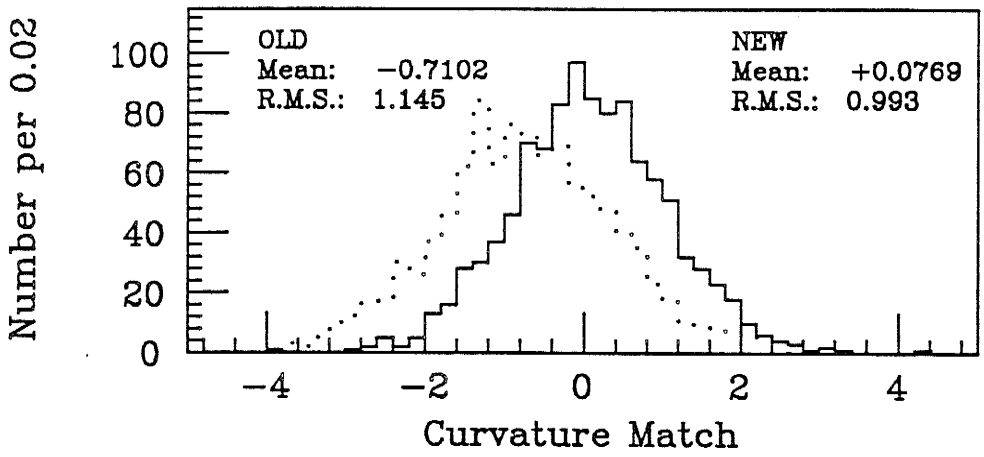

Figure 4.5: The difference in curvature between the incoming and outgoing branches of cosmic rays passing through our detector. These branches leave tracks of equal, but oppositely signed, curvature. The solid (dotted) histogram shows the matching after (before) chamber alignment. The matching variable plotted is normalized to the curvature uncertainties. It should have mean 0.0 and sigma 1.0. The residual charge asymmetry is 0.3% for a 35 GeV/c track.

in doing so we make no use of the kinematics of W decay. The W sample provides a pure ($> 99\%$) sample of electrons with well known production properties. The calibration relies on the comparison of two independent measurements of the electron (tracking chamber and calorimeter) and is reasonably independent of the kinematic distribution of the electrons [‡]. After adjusting cell-to-cell variations with the inclusive electron sample, we use the W electron sample itself to set the overall calorimeter energy scale, making it agree with the tracking chamber scale (see figure 4.9).

First, we calibrate the tracking chamber. This begins with the determination of timing offsets, drift velocities and a beam position on a run by run basis. The beam centre is determined with $5\,\mu$m accuracy for a $50\,\mu$m beam size. We align the chamber using charged particle tracks in minimum bias events. The tilted geometry of the drift chamber cells means that each track provides a measurement of the drift-time relationship. This data is collected online and provides calibration parameters for the first pass reconstruction. Having reconstructed tracks with this alignment we find $180\,\mu$m average axial residuals and

[‡]One exception to this statement is that possible calorimeter non-linearities (of O(0.015 %)/GeV) can effect electrons of different energies. The ramifications of this are discussed below.

average stereo residuals of 225 μm.

Remaining tracking chamber distortions fall into two categories: 1) overall magnification due, for example, to mechanical loading and 2) azimuthal misalignments introduced in the assembly of the chamber. An overall dilatation of the chamber is equivalent to an error in the magnetic field strength. Surveying the nominal wire locations with 50μm precision and mapping the absolute magnetic field to $\pm 0.05\%$ allows the tracking chamber's mass scale [§] to be set very accurately *a-priori*. We check for residual chamber dilatations using our sample of J/ψ and Υ di-muons (see figure 4.6). The J/ψ mass agrees perfectly, within its 0.03% statistical error and the Υ mass is $0.1 \pm 0.1\%$ high. The consistency of these measurements leads us to conclude that the tracking chamber mass scale is known to 0.2% [44].

The other concern, azimuthal alignment errors, can affect the chamber's resolution at high momenta, and can lead to charge dependent sagitta errors of the type:

$$\frac{1}{P} = \frac{1}{P_{\rm true}} + \frac{1}{\Lambda} \qquad (e^+, \mu^+) \tag{4.1}$$

$$\frac{1}{P} = \frac{1}{P_{\rm true}} - \frac{1}{\Lambda} \qquad (e^-, \mu^-) \tag{4.2}$$

By comparing energy to momentum for electrons and positrons (comparing equations 4.1 and 4.2, to equation 4.4 (below) for the electron energies and keeping only first order small quantities) we get:

$$\frac{1}{\Lambda} = \frac{1}{2 < E >} \left(\frac{E}{P}(e^+) - \frac{E}{P}(e^-) \right). \tag{4.3}$$

By equalizing E/P for electrons and positrons and requiring that they emanate from a common beam spot, we determine 166 wire-layer azimuth offsets (one for each wire-layer at each end of the chamber less two overall phases). We use cosmic rays, which provide branches of equal momenta but opposite charge, to verify the alignment. Figure 4.5 shows the improvement in curvature matching of cosmic ray branches after the alignment. The

[§] The measurement of the mass of a neutral particle (like J/ψ, Υ or Z) involves measuring both a positive and negative decay lepton's momentum. This leads to a cancelation of charge dependent momentum scale errors, without affecting the mass scale. The mass scale is applicable to measuring the average momentum of any sample of tracks have an equal number of positives and negatives, such as the Ws.

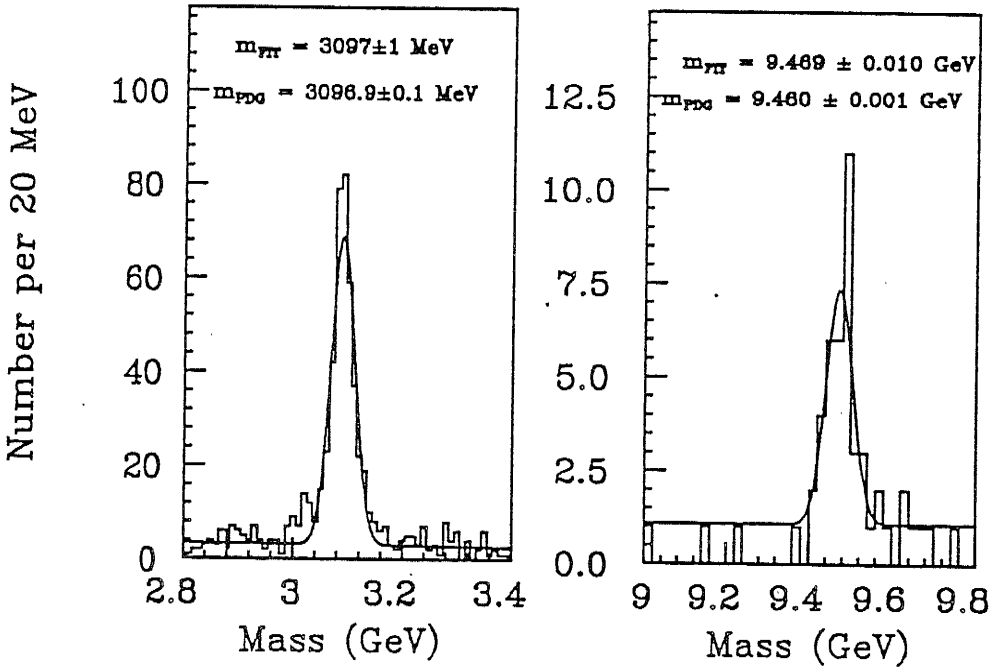

Figure 4.6: a) A sample of J/ψ and b) Υ di-muons which we use as a check of our tracking chamber's mass scale. From the agreement between our measured masses and the world's average masses we conclude that our tracking chamber is absolutely calibrated to 0.2%.

alignment does not change the mass scale of the chamber, it only improves the resolution at high momentum. When a beam constraint point is included on a track the chamber's resolution — after the alignment — is $\frac{\delta p_t}{p_t} = 0.0011 \times p_t$ (for p_t in GeV/c), or about 1.3 GeV/c for a 35 GeV/c track typical of W decay electrons.

As a check of the tracking chamber calibration we compare the Z mass we measure with our $Z \rightarrow \mu^+\mu^-$ sample to that measured at LEP. Our result is: $m_Z(\mu\mu) = 90.71 \pm 0.45$ GeV/c^2 [44]. For comparison we average the measurements of the four LEP experiments ([45, 46, 47, 48]) to get: $m_Z = 91.10 \pm 0.06$ GeV/c^2. This is consistent with our assertion that the chamber mass scale is known to 0.2%. We do not use this information to refine the tracking chamber mass scale.

Having calibrated the tracking chamber we transfer this calibration to the calorimeter. There are several subtleties in the reconstruction of electron energies. Electron showers, in the central calorimeter, span 1 to 3 calorimeter cells in a single wedge. For a cluster to expand beyond one cell the neighboring cell must have more than 100 MeV of E_t. To

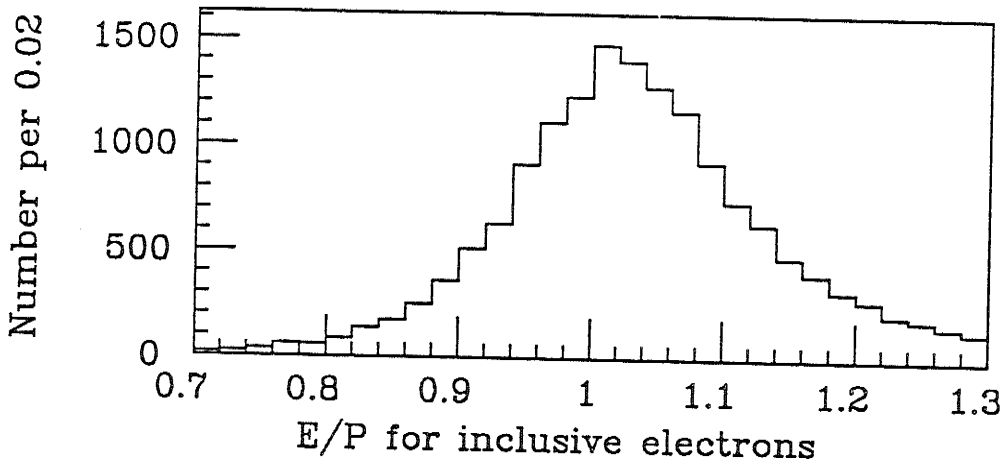

Figure 4.7: The E/P distribution for 17 000 inclusive electrons which we use to correct cell-to-cell miscalibrations in the central electromagnetic calorimeter.

compute an electron energy we use at most two cells of the electromagnetic calorimeter [¶]. These choices are a matter of definition. Here we calibrate the calorimeter using these conventions. A response map across the face of each cell, determined in the testbeam [49], gives a correction based on the shower position measured by the strip chambers. This correction accounts for light attenuation, the effect of cracks and shower leakage. It is accurate to $\pm 1\%$ over the fiducial volume we use.

Calorimeter cell miscalibrations can lead to offsets of the form:

$$E = E_{\text{true}} \quad (1+\epsilon) \qquad (e^+, e^-), \tag{4.4}$$

Here the offset, ϵ, is common to electrons and positrons. We combine 4.1,4.2 and 4.4 to solve for ϵ:

$$(1+\epsilon) \quad = \quad \frac{1}{2} \quad \left(\frac{E}{P}(e^+) + \frac{E}{P}(e^-) \right). \tag{4.5}$$

We exploit equation 4.5 for ϵ, both to correct cell-to-cell miscalibrations (see figure 4.8a) and to tie the overall energy scale of the calorimeter to the tracking chamber's mass scale (see figure 4.9). We adjust the gains in individual calorimeter cells by equalizing the average E/P in each cell, using a sample of inclusive electrons with $E_t > 15$ GeV. E/P for this sample

[¶] The third cell contains very little energy from the electron shower and has, on average, more underlying event energy.

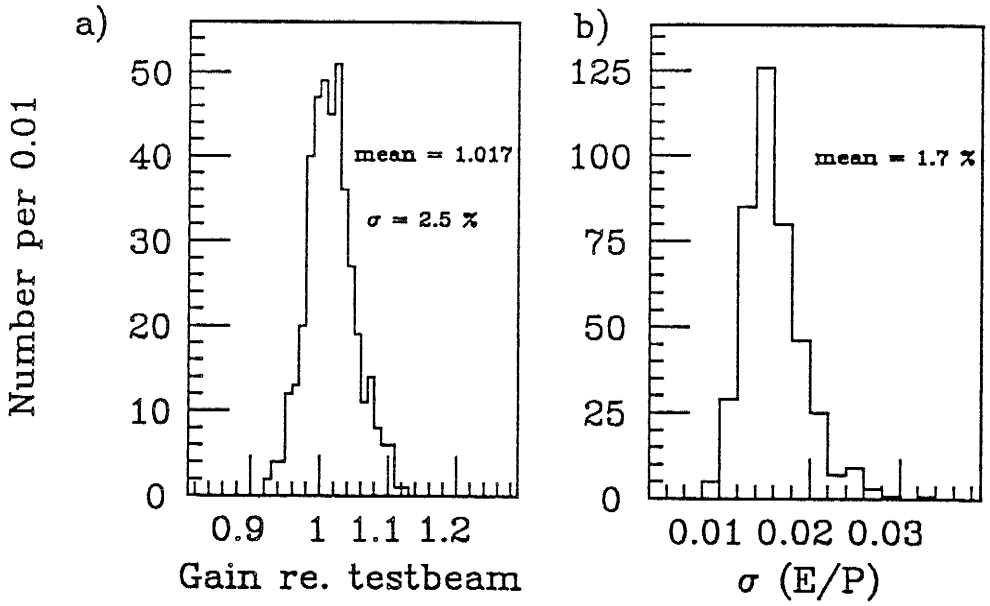

Figure 4.8: a) The cell-to-cell corrections we apply relative to the testbeam calibrated and source monitored gains. There is an overall shift of 1.7% in the average calibration of the calorimeter with a spread of 2.5%. b) The statistical uncertainty on setting each of the cells. The average setting error of the individual cells is 1.7%.

is shown in figure 4.7. We require the fraction of the electron candidate's energy leaking into the hadron calorimeter (HAD/EM) be less than 0.04 (see figure 4.3a), the energy sharing among cells in the cluster be consistent with the sharing observed at the testbeam ($LSHR$ [‖] < 0.2 see figure 4.3b), the showers seen in the strip chamber be consistent with testbeam showers ($\chi^2 < 10$ for 9 degrees of freedom in each view (x and z) see figures 4.3c,d) and the track and shower positions match ($\delta x \leq 1$ cm; $\delta z \sin\theta \leq 8$ mm) to select a sample of inclusive electrons. We further require track momentum to shower energy matching, $0.7 \leq E/P \leq 1.3$, and the pulse height ratio, r, between the two views of the strip chamber be within 40% of nominal. This results in the selection of 17 000 electron candidates. The selection is not highly restrictive, leaving 4% background. These background hadrons can shift the mean E/P, but influence all cells similarly. The rapid convergence in the comparison of equations 4.1 and 4.2 to equation 4.4 (we iterate only once as a check)

[‖]The variable used to make the comparison, $LSHR$, is a sum over neighbouring calorimeter cells: $\sum[E_i(\text{obs.}) - E_i(\text{pred.})]/\sigma$ normalised to the measurement uncertainty, where the predictions come from the testbeam. Since the measurement can fluctuate above or below the prediction it is possible for $LSHR$ to be positive or negative. More details can be found in reference [50].

reflects the precision of our intial calibrations and alignments (figure 4.8a shows typical ϵs).

Remaining contributions to the CEM resolution include the uncertainty in the response map and time variations in the cell gains over the course of the run (averaged over in the inclusive electron E/P study). We expect these effects taken together to add less than 1% in quadrature to the 1.7% statistical cell setting uncertainty from the inclusive electrons (see figure 4.8b). We use a 2% energy independent contribution to the CEM resolution in our model of the electromagnetic calorimeter (see section 5.1 and equation 5.2).

The absolute setting of CEM energies comes from a comparison of E/P for W electrons to a prediction which includes radiative effects. The energy does not exactly match the momentum because electrons radiate in the detector lowering the observed momentum. The W decay can also have associated internal radiation. While the calorimeter measures most of the radiated photons (see section 6.1), the tracking chamber measures only the momentum of the charged track. Thus $E/P \geq 1$ on average. We compare the W data to a radiative W decay Monte Carlo [51] along with a full detector simulation. The agreement in shape is good (see figure 4.9).

We tried several methods of extracting the absolute scale, all of which yielded similar results. From the integral distribution (figure 4.10) we choose to consider only electrons with $E/P \leq 1.4$. This ensures that at the cutoff our measurement is not dominated by detector resolution. Truncating at 1.4, we find that the simulation predicts a 2.5% shift in the mean E/P. To reproduce this in the data requires re-scaling all CEM energies by 1.017 (a 1.7% adjustment in the overall calibration).

The tracking chamber mass scale is known to 0.2%. The tracking chamber and calorimeter resolutions lead to a measurement uncertainty in E/P. With 1800 W electron candidates we are left with an 0.23% statistical E/P matching uncertainty. Studies of the simulation and radiative calculation, including the loss of photons in the magnet coil and the amount of material present in front of the tracking chamber lead us to assign an 0.25% systematic uncertainty to our prediction of the radiation. Thus we are left with an overall systematic

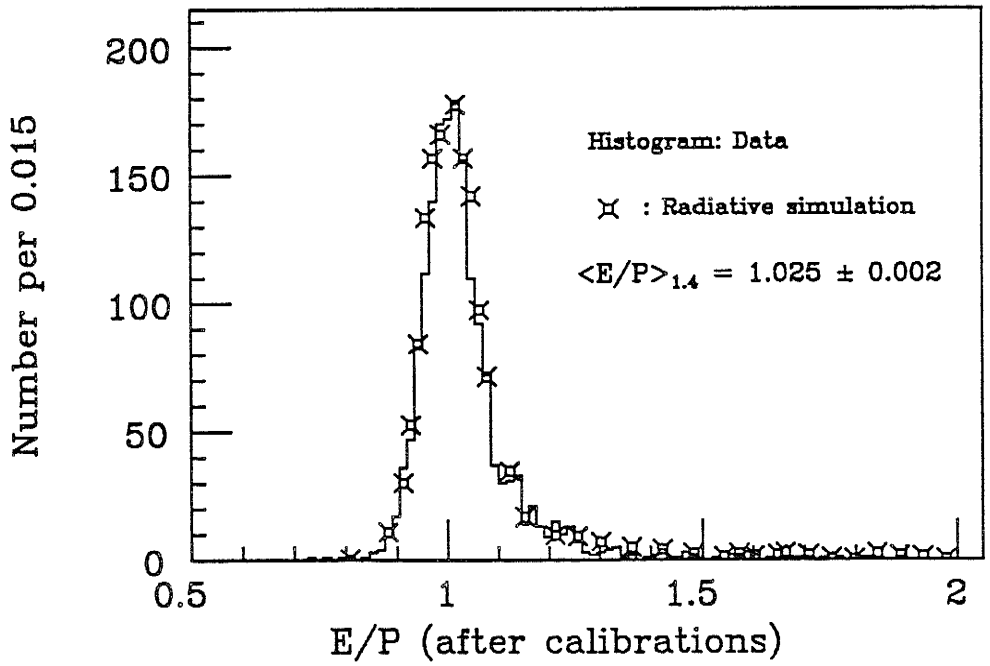

Figure 4.9: The E/P distribution for W decay electrons compared to the radiative simulation. We use this to set the overall scale of the central electromagnetic calorimeter.

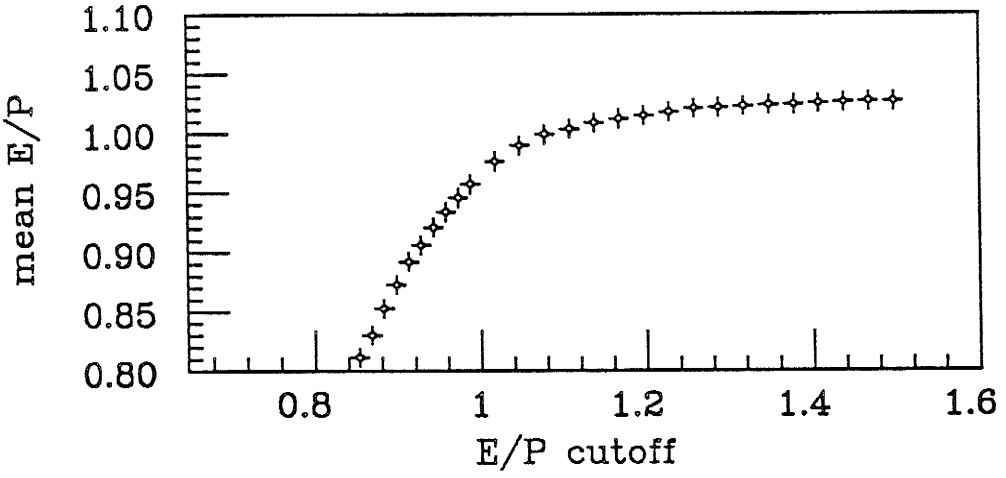

Figure 4.10: The integral distribution of E/P for the data, distinguishing between the resolution dominated bulk of the E/P distribution and the primarily radiative tail. This distinction leads to the choice of truncation at 1.4 well out of the resolution regime.

uncertainty on the energy scale of:

$$\sqrt{0.20^2_{\text{(tracking)}} + 0.23^2_{\text{(E/P stat.)}} + 0.25^2_{\text{(Rad.corrections)}}} = 0.39\%. \quad (4.6)$$

We consider two further complications. First, some of the energy from the event underlying the W ends up in the same cell(s) as the electron being measured. Estimates of the size of this effect reveal that on average of 50 MeV ends up in each electromagnetic cell **. We choose to leave the underlying event contribution when we match E to P. Knowing that the underlying event contributes $O(0.2\%)$ to the electron energies in vector boson decay we ignore it both in the calibration and the mass measurement — it cancels to first order. We note that the underlying event energy contribution to W and Z electrons is similar and thus also cancels in the measurement of the mass ratio.

Second, calorimeter non-linearities can effect the measurement of W and Z electrons differently. We calibrate with W electrons which have an average energy of 40 GeV. Our Z electrons have a slightly higher average energy: 45 GeV. Testbeam studies indicate that the CEM response as a function of energy is linear to better than 0.02%/GeV. This means that we might suffer an 0.15% calibration difference in measuring electrons from Ws and Zs. The data shows no evidence for any systematic shift in calibration, but we take this potential 0.3% calibration shift as a systematic uncertainty on the measurement of the mass ratio, m_W/m_Z.

Again, we can check the calorimeter calibration by comparing the Z mass we measure in our calorimeter to that measured at LEP. Our calorimeter result is: $m_Z(ee) = 91.18 \pm 0.52$ GeV/c^2 ††. This compares favourably with the LEP result of 91.10 ± 0.06 GeV/c^2. The details of this comparison are left to chapter 7 where implications of extracting the mass ratio, m_W/m_Z, are discussed in detail.

**Here the electron energy will cause the calorimeter cell to be readout and any energy present from the underlying event will shift the observation. If the electron energy were not present the underlying event energy would often be insufficient to cause a cell to be readout — the readout threshold is $\approx$ 50 MeV. With this in mind several studies of the underlying event in the CDF data [52] come to the similar conclusions.

††This number is adjusted by 0.08% relative to the CDF published value of the Z mass [44] to reflect subsequent improvement of the calorimeter calibrations.

4.3 Neutrino Energy Corrections

A neutrino's transverse energy can be inferred from the transverse energy imbalance in an event. We define this imbalance by the vector:

$$\vec{E}_t = \sum_i E_{ti} \cdot \hat{\mathbf{n}}_i, \tag{4.7}$$

$$\vec{\not{E}}_t = -\vec{E}_t, \tag{4.8}$$

where the sum is over cells of the calorimeter and the $\hat{\mathbf{n}}_i$ are two dimensional unit vectors pointing to the cell centres. Because the low-β quadrupole magnets obscure part of the forward hadron calorimeter, the sum extends only over cells with $|\eta| < 3.6$. To be included the sum individual cell energies (not E_ts) must exceed detector dependent thresholds [†]. We study the $\not{E}_t$ resolution in minimum bias events – events where no imbalance is expected [53]. We observe offsets (of -250 ± 40 MeV in x and 100 ± 40 MeV in y) in the projections of the $\not{E}_t$ of these events. We correct for these average shifts in the reconstruction of the W events. The resolution can be parametrized by a constant times the square-root of the total scalar E_t observed in the event (see figure 4.11):

$$\sigma_{\not{E}_{x,y}} = 0.47\sqrt{\sum_i E_{ti}}, \tag{4.9}$$

where the scalar sum is over the same calorimeter cells as the vector sum in equation 4.8. The scaling behaviour is a reflection of the individual calorimeter's resolution on the total energy they measure. The model we use to extract the W mass assumes that the energy underlying a W decay can be factored into two pieces. The recoil of the W appears as directed energy flow in our detector, while the measurement resolution is dominated by the event underlying the W decay. We assume that this resolution is described by equation 4.9 when the $\sum E_t$ appropriate to W events is inserted. For more details see section 5.1.

When measuring the $\not{E}_t$ in a W decay we must cleanly separate the electron from the rest of the event. In particular, the electron reconstruction uses only electromagnetic cells

[†] These thresholds are 100 MeV in the CEM, CHA and WHA, 300 MeV in the PEM, 500 MeV in the PHA and FEM and 800 MeV in the FHA.

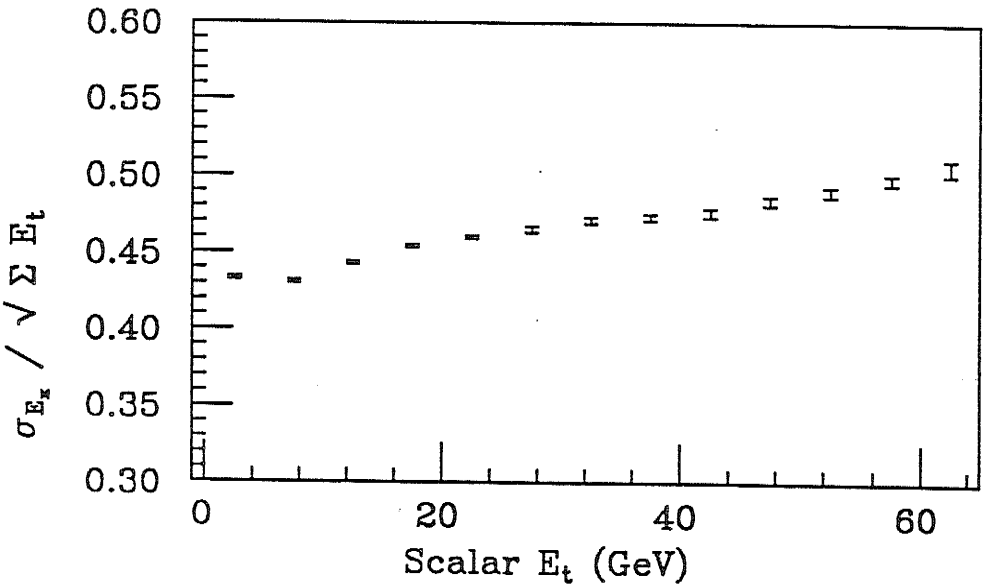

Figure 4.11: The dependence $\sigma_{\not E_x}/\sqrt{\sum E_t}$, a neutrino-resolution variable, on the total scalar E_t observed in minimum bias events. This plot shows that the constant of proportionality between $\sigma_{\not E_x}$ and $\sqrt{\sum E_t}$ is 0.47 approximately constant over the range of $\sum E_t$s covered by the W decay candidates (see figure 5.5).

of the calorimeter. We calibrate out shower leakage, but this leakage is observed in the surrounding calorimeter and should not be included in the underlying event. To avoid this over counting we measure the $\not E_t$ in all of the calorimeter except the three cells in the same wedge (electromagnetic and hadronic) centred on the electron cluster. This is a measurement of the missing transverse energy of the rest of the event, $\vec{\not\mu}$. The neutrino can then be reconstructed as:

$$\vec{\nu} = \vec{\not\mu} - \vec{e}. \tag{4.10}$$

The measurement of $\not\mu_{||}$ (parallel to the electron direction) is sensitive to the way we separate the electron from the "rest" of the event. If the subtraction is not done judiciously a systematic shift can result. Three effects complicate this separation. 1) The electron shower and accompanying radiation can extend beyond three calorimeter cells. 2) The electron receives the boost of the decaying W, resulting in a small correlation between the electron direction and the hadronic activity in the event. 3) Our back-to-back jet veto biases our sample, removing events with energy opposite the electron cluster, resulting in

an anti-correlation. By removing the energy found, in the electromagnetic and hadronic compartments of the calorimeter, in the electron seed cell and its two neighbours in η, $\not\!\!\mu_{||}$ is centred to first order. A study of the energy flow elsewhere in the W event reveals that we remove an average of 60 ± 5 MeV of underlying event energy from the nominal electron cells [‡]. On average 260 ± 20 MeV of electron shower energy leaks outside the nominal three cell cluster. We make a 200 MeV average correction (260 – 60 MeV) to $\not\!\!\mu_{||}$ to correct for these two effects. We are left with a -76 ± 115 MeV bias in the $\not\!\!\mu_{||}$ distribution shown in figure 4.12. $\not\!\!\mu_{\perp}$, the projection of the underlying event perpendicular to the electron direction, is less complicated. No correlation between the measurement of the electron of the residual event activity is possible. We see none — the distribution of $\not\!\!\mu_{\perp}$ is centred (see figure 4.13).

The study of the underlying event energy flow in $W \rightarrow \mu\nu$ decays is instructive. There is little activity associated with the passage of a muon through the calorimeter. This simplifies the accounting for leakage providing an interesting cross-check. The size of the muon sample (600 events) makes it difficult to sharpen the conclusions arrived at with the electron data, but it provides a different sample against which we check our assumptions. Our understanding of the behaviour displayed in the electron data is born out by the muon data [43].

Another correction compensates for our detector's non-linear response at low energies. Several effects reduce the calorimeters' response to charged particles at energies below 10 GeV. Since most of the Ws we are measuring have $p_t \leq 10$ GeV we are sensitive to this behaviour. Charged hadrons below 5 GeV deposit only about 60% of the signal expected from our calorimeter calibrations (see figure 4.14 [29]). Our calorimeters are not compensating, leading to this fall-off in response at low energies. Worse, the magnetic field traps charged particles below 400 MeV, never allowing them to reach the calorimeters. Charged

[‡] Here we are concerned with the bias on the neutrino measurement. Thus we are only interested shifts that appear above the thresholds used in equation 4.8. The average E_t seen per cell, in the events underlying Ws, in the central calorimeter is 20 MeV

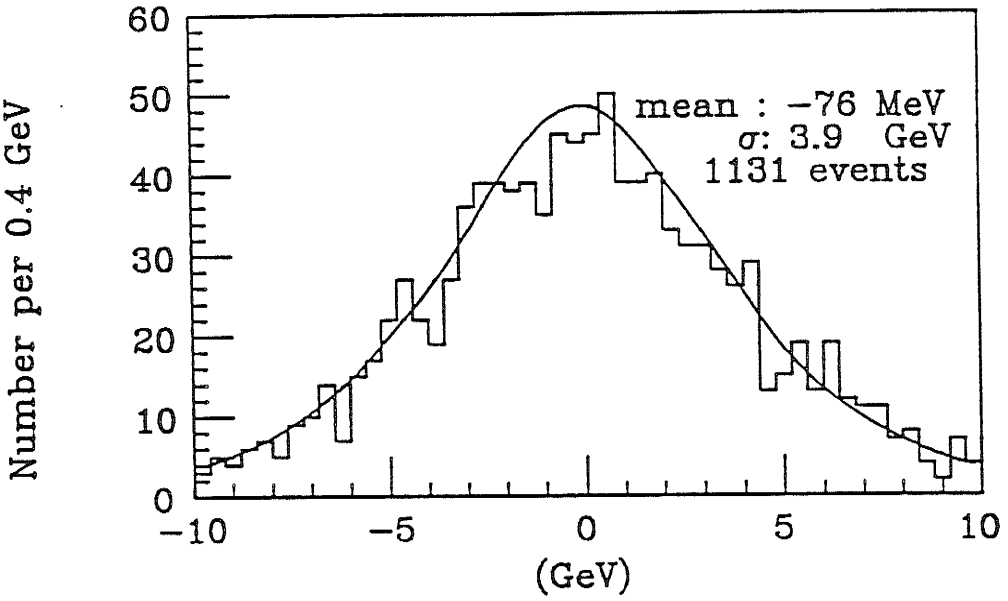

Figure 4.12: The projection of the underlying event $\not\!\!E_t$ onto the electron direction, $\not\!\!p_{\parallel}$. This distribution is used to study the details of distinguishing the electron from the underlying event. The curve overlaid is our model's prediction. This projection provides a measure of the correlation between underlying event and the electron.

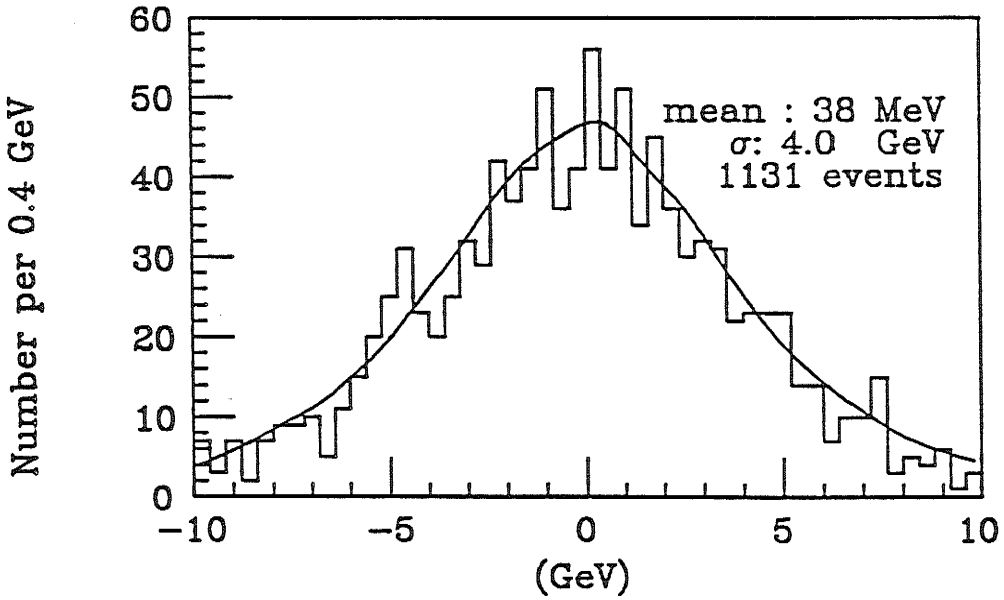

Figure 4.13: The projection of the underlying event $\not\!\!E_t$ perpendicular to the electron direction, $\not\!\!p_{\perp}$. The curve overlaid is our model's prediction. There is no physics which can bias this distribution; unbiased, it serves as a prototype for $\not\!\!p_{\parallel}$.

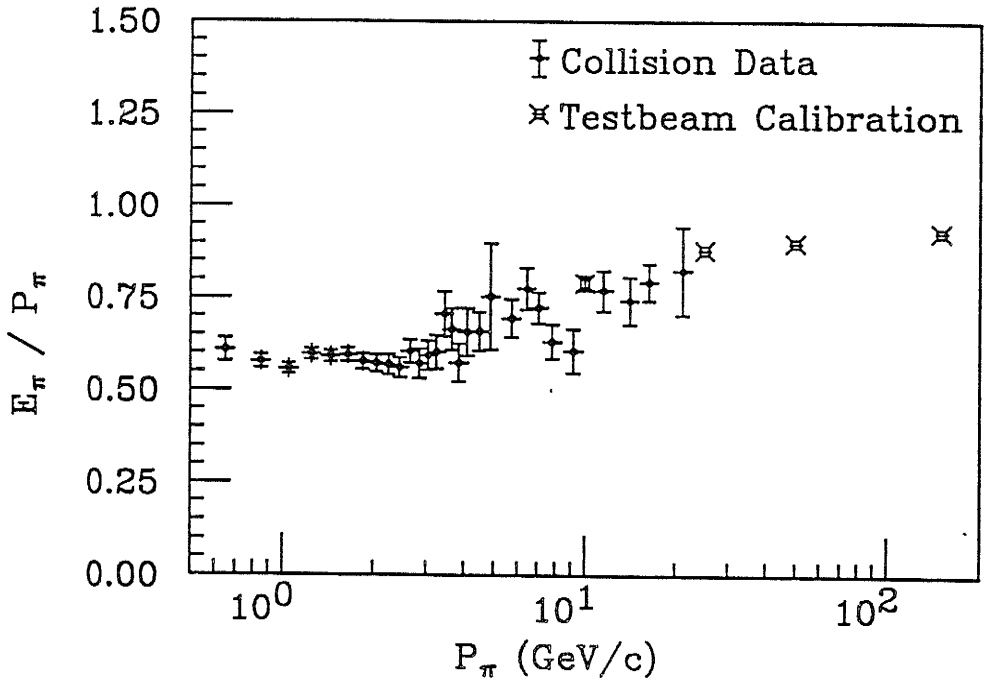

Figure 4.14: The ratio of the energy observed in the combined hadronic and electromagnetic calorimeter — using the nominal testbeam calibrations — compared to the track momentum for isolated charged pions. The response at low energies falls because our calorimeters are non-compensating.

particles with 400 – 800 MeV arrive at significantly different azimuth, thereby diluting the directional information provided by the calorimeters.

We measure these effects with our Z data. There we measure both decay leptons determining — relatively precisely — the Z transverse momentum. By removing the decay leptons from the event we can study the recoil energy in the calorimeters. In order to minimize the effect of our lepton measurement resolution we study p_η of the Z (see figure 4.15a). Electron energy resolution smears the measured p_ξ of the di-lepton system. By scaling up the energy observed in the calorimeters, recoiling against the Z, until the calorimeter measurement of p_η matches that of the di-leptons, we conclude that our calorimeter only measures about half of the recoil momentum in Z events (see figure 4.16).

This degradation in p_t observed by the calorimeter compared to the true p_t (as measured by the di-leptons in Z decays) also occurs in W decays. In a W event we measure only one lepton; the degradation results in a mismeasurement of the neutrino (inferred from all other

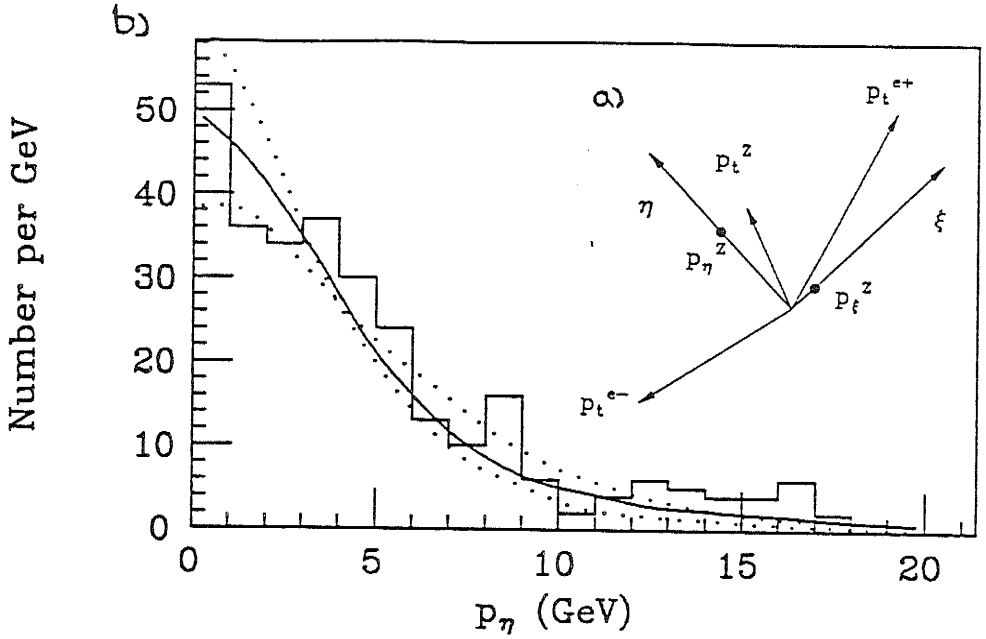

Figure 4.15: a) (inset) The η-ξ coordinate system. Since the leptons tend to be back-to-back the largest contribution from measurement uncertainty is in the ξ direction. p_η is more directly related to the "true" Z motion. b) The di-lepton p_η observed in Z events compared to our model's prediction (solid line). To the extent that the W and Z p_t distributions should be the same at low p_t this shows that our model includes an appropriate W p_t. The dotted lines show the 1σ limits on the degradation derived from this data (see section 5.2.3 for details).

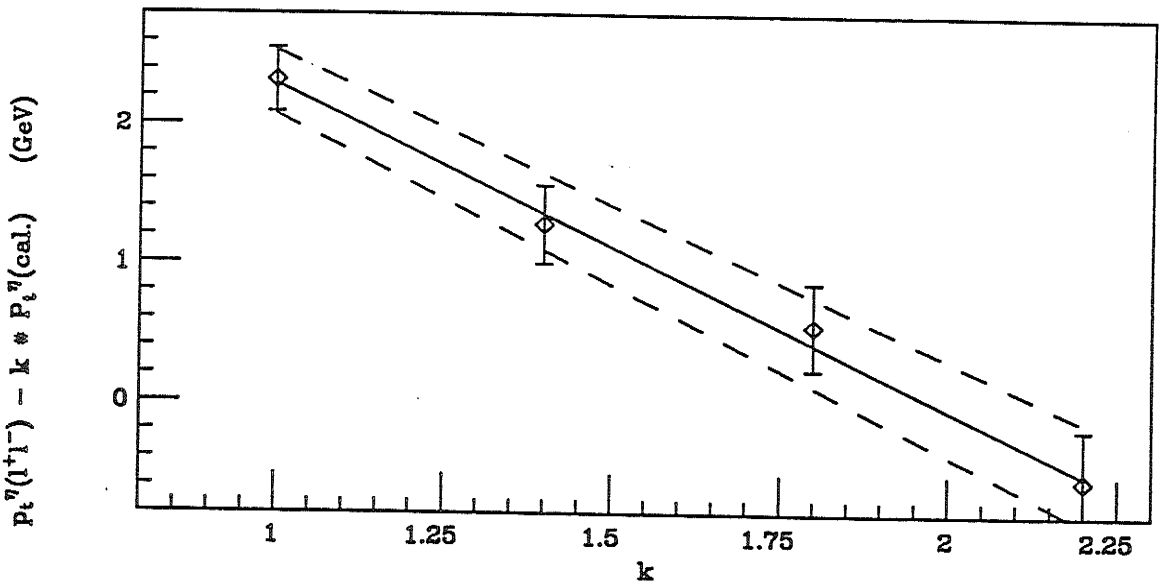

Figure 4.16: The average difference between the di-lepton p_η and the hadronic recoil p_η for $Z \rightarrow e^+e^-$ events as a function of the underlying event energy scaling factor applied. Balance is achieved for a scaling factor of 1.99 ± 0.14. The scaling accounts for calorimeter non-linearities and magnetic sweeping which reduce the observed recoil energy.

measurements, see equation 5.3). Since only part of the underlying event comes from the recoil of the W — the rest coming from the spectator partons — we have a signal-to-noise problem. Boosting the measured underlying event energy by a factor of 2 (to fully compensate for the degradation we observe in Z events) results in the scaling of the random energy associated with underlying event. We scale the underlying event energy up by a factor of 1.4 to partially correct for the degradation at low p_t and match the correction at high p_t required in jet events (see figure 5.4). This recoups much of the lost information, improves the transverse mass resolution, while not overwhelming the measurement of the neutrino with artificially scale spectator parton noise. This scaling is a matter of definition. We have checked that this choice does not affect our measurement of the W mass. Changing it from 1.0 to 1.8 changes the fit mass value of ± 150 MeV/c^2. Since this scaling factor plays a role in determining the detailed shape of the observed transverse mass distribution it is not surprising that such shifts (a fraction of the statistical uncertainty of the measurement, see section 5.4) are observed. Details of this study can be found in section 6.7.

The effect of halving the boson p_t emerges when we attempt to infer the true W p_t, from the measured p_t. Our model based on this analysis results in the W p_t we use agreeing with the p_t seen in our Z data (see figure 4.15b). The description of our model and the extraction of the W p_t distribution used is the subject of the next chapter.

Chapter 5

Measuring the W Mass

As described in section 2.1 we measure the W mass using the transverse kinematics of the candidate events. Since the longitudinal momentum of Ws produced in $p\bar{p}$ collisions is not constrained and we infer the neutrino's momentum from the energy imbalance in the detector we cannot measure the invariant mass of the electron-neutrino system. Instead, we compare various kinematic quantities of the electron-neutrino system to predictions for W decays. To make these predictions we include the physics of W production and decay as well as a simulation of our detector's response. We vary the W mass (and width) hypothesis in the simulation and compare the resulting spectra to the data.

The transverse mass, m_t (see equation 2.16), distribution for our W sample is shown in figure 5.1. As described in section 2.1 the upper edge of the distribution is kinematically constrained by the W mass. The loss of energy into longitudinal motion can only reduce the observed m_t. It is the upper edge which provides most of the information in the mass fit (see section 6.5).

We also study the electron and neutrino E_t spectra as a check of the details of our model. Ws without transverse motion could never produce decay leptons with $E_t^l \geq \frac{1}{2}m_W$. However, the finite p_t of the Ws mitigates this constraint migrating decay leptons to $E_t^l > \frac{1}{2}m_W$ (see figure 5.2). The W p_t distribution is not well measured (especially at low p_t), hence the

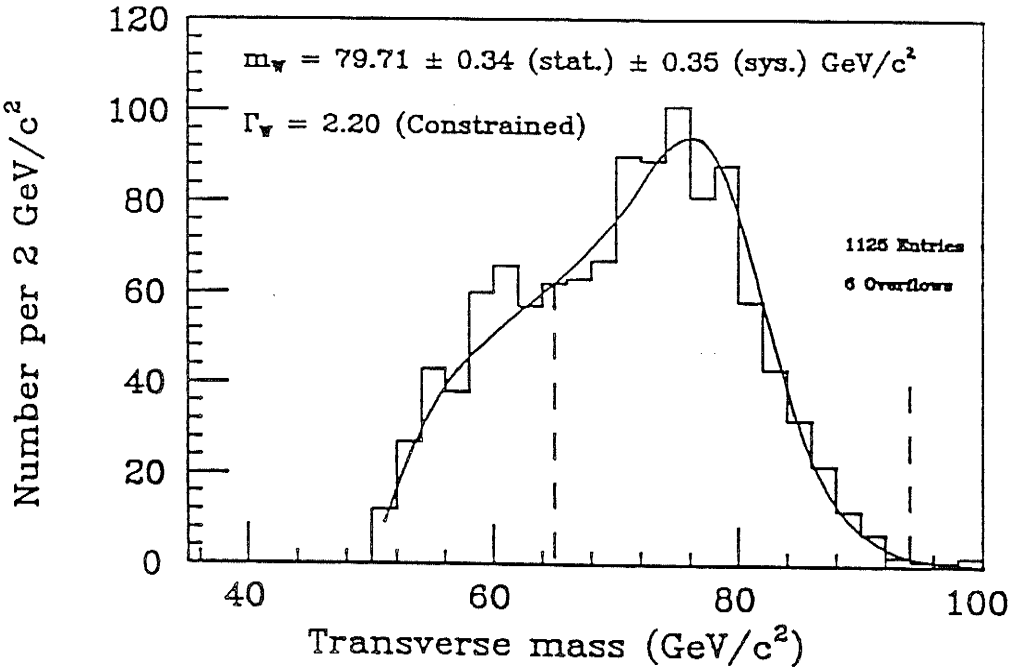

Figure 5.1: The transverse mass distribution for electron W candidates (whose selection is described in chapter 4). Overlaid is the best fit giving a W mass of 79.71 ± 0.34 (stat.) GeV/c^2. The dashed lines show the range of m_ts used in the fit.

prediction of high E_t leptons is problematical. This highlights the principal advantage of m_t. The $\not\!\!E_t$ measurement included in m_t provides information on the W recoil in the underlying event, hence m_t is less sensitive to this recoil.

The following sections describe the model we use to simulate W decay, the constraints we place on this model, the mechanics of comparing the simulated line shapes to the data and the extraction of the W mass.

5.1 The Simulation

Unlike the measurement of the Z mass, which is done by comparing the data to an analytic form, the measurement of the W mass relies on the comparison of the data to Monte Carlo line shapes. Further, the Jacobian shape couples detector resolution to the mass measurement. In the Z case, the invariant mass can be calculated exactly, but the W distributions, described above, are not bounded from below – they depend on the amount

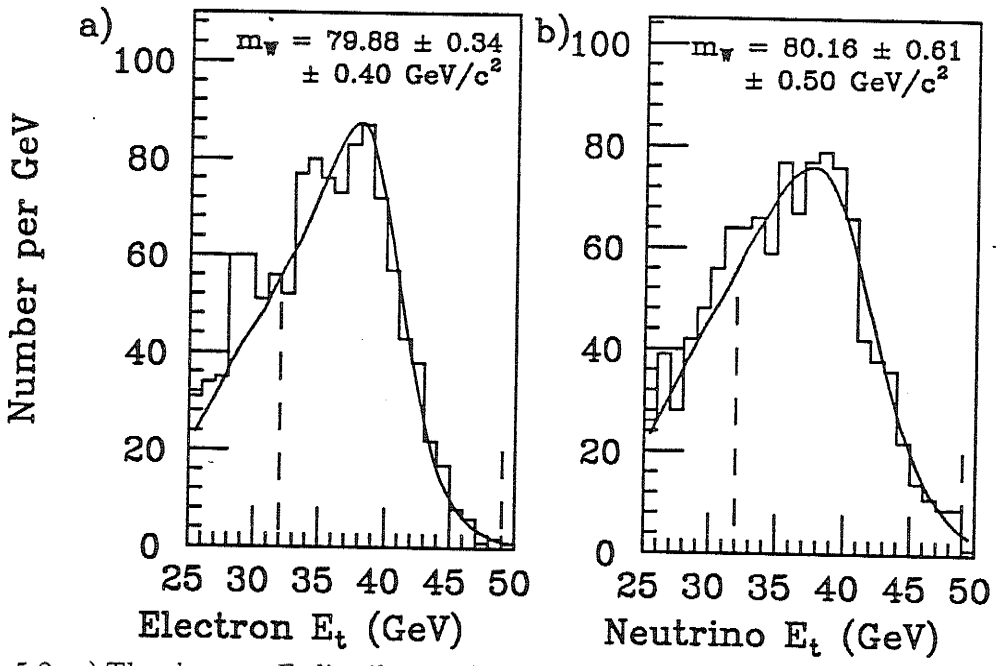

Figure 5.2: a) The electron E_t distribution for electron W candidates, selected for measuring the mass. b) The corresponding neutrino E_t distribution. Overlaid, in both cases, is the best fit to the data (discussed in section 6.7). The dashed lines show the range of E_ts used in the fits.

of longitudinal momentum carried away, undetected, by the neutrino. Changes in the resolution and the longitudinal momentum distribution of the Ws result in shifts of the predicted shape and hence the fit mass.

Following the discussion of section 2.1 we use a Monte Carlo program which generates W decays to electrons from the lowest order QCD quark annihilation. The program includes the W polarization in the electron decay angular distribution [54]. The parton distribution functions, W boson p_t distribution and detector resolutions were easily varied to allow systematic studies of their effect on the shape of the Jacobian.

The simulation begins by generating the W rapidity, mass and polarization distributions for the mass, m_W, width, Γ_W and parton distribution being simulated. The rapidity distribution reflects the parton distribution function we use to model the initial $p\bar{p}$ collision. The mass distribution reflects the convolution of the parton luminosities with an approximate

relativistic Breit-Wigner line shape (taken from [55]):

$$\frac{dN}{dm_W} \sim \frac{s}{(s-m_W^2)^2 + s^2\Gamma_W^2/m_W^2}. \tag{5.1}$$

We model only that part of the Breit-Wigner that is within seven widths (Γ_W) of the requested mass. We include the polarization distribution to model W^+s coming from u quarks in the anti-proton (or W^-s from $\bar{u}$ quarks in the proton) which have the opposite helicity of the more plentiful W^+s coming from a u quark in the proton (see equation 2.10 and figure 2.6). After we generate these basic distributions we begin to make W events. We choose a rapidity, y_i, mass, m_i, and polarization, P_i for the W from the distributions by rejection. We select the decay angle of the electron (θ_i), in the rest frame of the W, from a $(1 + P_i\cos(\theta_i))^2$ distribution. Finally we chose a random electron decay phi, ϕ_i. We then compute the electron and neutrino four-vectors in the lab from m_i, y_i, θ_i and ϕ_i.

After event generation, we simulate detector effects. We vary the event z vertex, simulate the geometry of the detectors, the detector resolution and the finite p_t of the W. Though not a detector effect, we include the p_t of the W at this stage to simplify the study of the effect it has on the line shapes. We pick a z vertex at random from a Gaussian distribution truncated at $\pm$ 60 cm to match the data (see figure 4.2). We propagate the electron from the vertex to the detector where we simulate the fiducial cuts. The rapidity cuts play a role in determining the detailed shape of the Jacobian peak. We smear the electron energy with a Gaussian resolution function whose width (see section 4.2) is equal to:

$$\frac{\sigma_{E_t}^{\text{electron}}}{E_t} = \sqrt{(\frac{a}{\sqrt{E_t}})^2 + b^2} \qquad a = 13.5\% \qquad b = 2.0\%. \tag{5.2}$$

We do not smear the electron's direction, which we measure with the tracking chamber. The chamber's pointing resolution, at $\leq$ 0.5 mrad, is much better than the $\sim$ 50 mrad angular resolution on the neutrino which we do simulate (see below).

Our model of the neutrino breaks down into three pieces: 1) the energy balancing the transverse motion of the W, which we call $\vec{p_t}$(jet), 2) the smearing due to the underlying

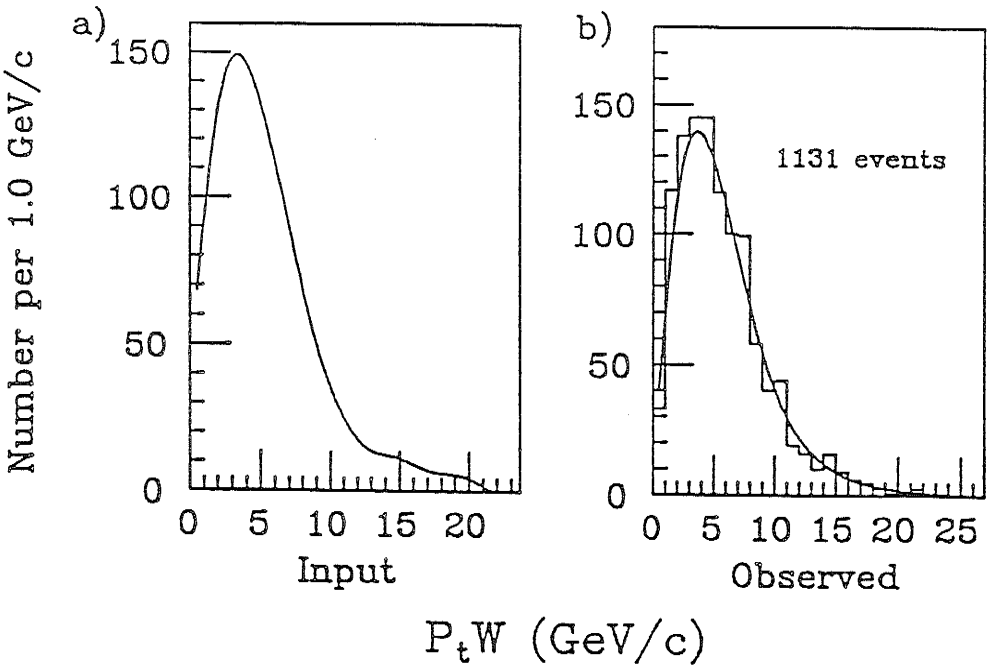

Figure 5.3: a) The p_t distribution of the W candidates unfolded from the observed distribution (figure b) using the model. b) The agreement between the observed W p_t distribution and the model's prediction.

event, $\widetilde{u}$ and 3) the electron measurement, $\widetilde{e}$. We take:

$$\vec{\nu} = -\vec{p_t}(\text{jet}) + \widetilde{u} - \widetilde{e}. \tag{5.3}$$

The model of p_t(jet) starts with the p_t of the W. The W p_t distribution we use is determined iteratively. We start with the shape of the observed p_t distribution (see figure 5.3b) and sculpt it, by adding events in the tail, until our model (described below) returns the observed distribution. In the end we add only 2% more events to match the shape. The sculpting allows us to match both the first and second moments of the observed distribution (within errors). After iterating we arrive at the input distribution shown in figure 5.3a and agreement with the observed distribution shown in figure 5.3b.

To compute p_t(jet), we degrade the W p_t by a momentum dependent factor (see figure 5.4). This degradation accounts for calorimeter non-linearities and magnetic sweeping. It matches the known jet correction above p_t = 30 GeV/c [29]. However, none of the Ws we model have p_t this large. Below 30 GeV we extrapolate linearly (an assumption of our

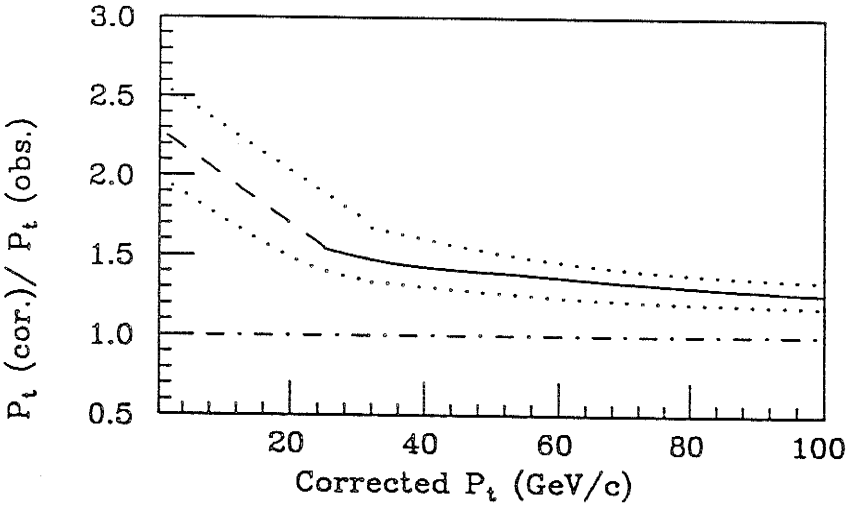

Figure 5.4: The degradation factor used in our model to simulate the effect of calorimeter non-linearities and magnetic sweeping on the measurement of the energy underlying W decays. The solid part of the curve comes from the study of jet events [29], while the dashed line is our extrapolation to lower p_ts. This extrapolation is constrained by the observation of the recoil in di-lepton decays of Zs. (see also figure 4.16). The dotted lines indicate the degree of variation possible on this degradation within the context of our model.

model) to a degradation factor of 2.3 at $p_t = 0$. This model is tuned to provide a consistent picture of the degradation seen in Z events. In figure 4.16 we showed that the average degradation was a factor of 1.99 ± 0.14. When the "curve" in figure 5.4 is folded with the Z p_t distribution this average factor of 2 is returned. After degrading we have a measure of the "jet" opposite the W or Z decay, we then smear the "jet" by:

$$\sigma_{p_t(\text{jet})} = 0.85 \times \sqrt{p_t(\text{jet})} \quad , \tag{5.4}$$

to model the effect of "jet" energy resolution.

Finally, we add $\widetilde{u}$, the underlying event smearing, according to equation 4.9. To compute $\widetilde{u}$ we choose an underlying event energy ($\sum E_t^{\text{data}}$) at random from figure 5.5. We smear the underlying event measurement only with the energy of the spectators, and not the "jet". Thus we correct the $\sum E_t^{\text{data}}$ on average for the presence of the "jet" in our model. We reduce $\sum E_t^{\text{data}}$ by $< E_t(\text{jet}) >$ ($< E_t(\text{jet}) > \equiv 1.4 \times < p_t(\text{jet}) >$). That is we take:

$$\sum E_t^u = \sum E_t^{\text{data}} - 1.4 < p_t(\text{jet}) >, \tag{5.5}$$

and use $\sum E_t^u$ to determine $\widetilde{u}$. The factor of 1.4 accounts for the fact that the energy in a

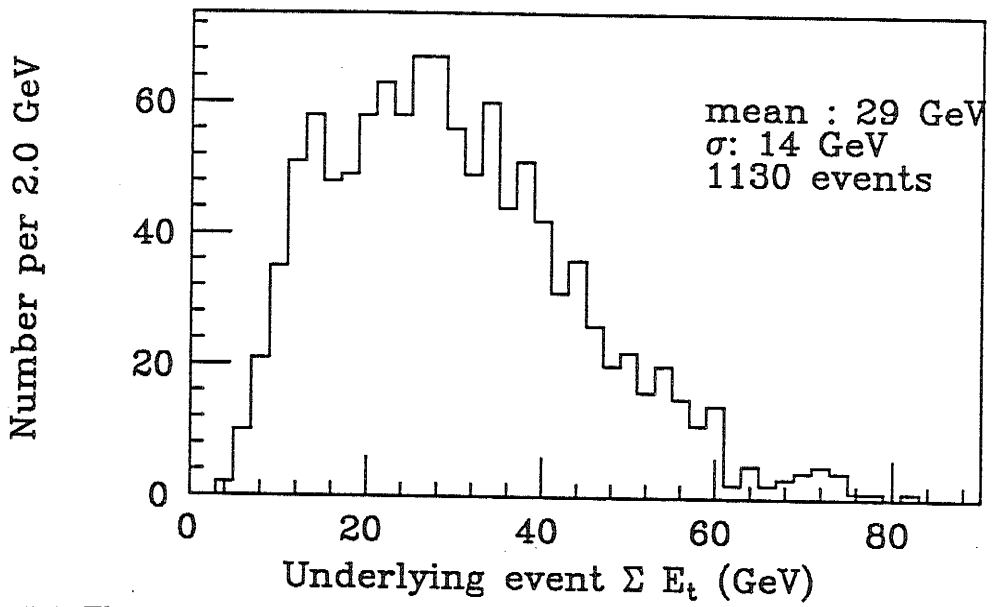

Figure 5.5: The energy observed accompanying the electron in W decay candidate events. This distribution is used as an input to the detector model of the neutrino resolution.

"jet" (especially at these low momenta) is not equal to the momentum of the "jet" because of jet spreading. We vary the scaling factor (between $< p_t(\text{jet}) >$ and $< E_t(\text{jet}) >$) from 1.0 to 2.0 and find that it has little effect on the fit mass. The average p_t(jet) is 3 GeV. Taking $3-6$ GeV from the $\sum E_t$ results in no significant change in the average $\widetilde{u}$ we model. Determining $\sum E_t^u$ in this way ensures that it is uncorrelated with the motion of the W. That is, the energy deposited by spectator partons is unrelated to the motion of the W. We check our dependence on this assumption by choosing $\sum E_t$s from figure 5.5 that *are* correlated to the p_t of the W * and find that this makes less than 60 MeV/c^2 difference to the final fit mass value. Once $\sum E_t^u$ has been determined we choose u_x and u_y independently from Gaussian distributions having sigma:

$$\sigma_{\not{E}_{x,y}} = 0.47\sqrt{\sum_i E_{t\,i}^u}, \tag{5.6}$$

and add them vectorially in equation 5.3.

One further constraint on the event underlying our W decays is the energy flow along the electron direction. We partially correct the individual underlying event measurements

*To do this we choose a $\sum E_t^u$ from the upper half of the distribution for Ws with p_t above the median of the p_t distribution and from the lower half for those with p_ts below the median p_t.

in the data — on average — for detector effects which bias $\not\!\!E_{||}$ as described in section 4.3. However, we do not model the topology of jets in our detector — only their contribution to the underlying event energy flow — thus we cannot directly model the effect of our di-jet cut. This cut anti-selects events with energy back-to-back with the electron. The di-jet cut, along with additional biases in $\not\!\!E_{||}$ leave a residual shift of $< \not\!\!E_{||} >= -76 \pm 115$ MeV (see figure 4.12). W boosts give $< \not\!\!E_{||} > \geq 0$. Our model includes these boosts and predicts $< \not\!\!E_{||} > \sim 80$ MeV. We account for the effect of the di-jet cut and residual biases in our model by subtracting a further 156 MeV from the underlying event (parallel to the electron) in order to match the observed $< \not\!\!E_{||} >$.

Finally, we reconstruct the neutrino transverse momentum using equation 5.3 and the $e\,\nu$ transverse mass using equation 2.16. We require $E_t^e \geq 25$ GeV and $\not\!\!E_t^\nu \geq 25$ GeV to model the kinematic acceptance of our sample. The comparison of these distributions to the data is described in section 5.3.

5.2 Constraints on the Model

Modelling the event underlying W decays allows us to study the effect of mismeasurements on the m_t distribution and hence the W mass. The decomposition described above lends itself to constraints from other CDF data (minimum bias and p_η (Z)). We describe here the limits of reasonable variation on the model parameters. The effect these variations have on the W mass will be described in chapter 6. We use the projections of the W underlying event measurements (figures 4.12 and 4.13), the mean p_t observed in the W decays and the rms of the p_t distribution as possible constraints. In practice these are almost completely correlated so we only use one, the mean p_t, as a constraint on the model, the other constraints come from minimum bias and Z data.

The rms of the underlying event energy measurements are:

$$\sigma_\perp = 3.98 \pm 0.08 \text{ GeV}; \qquad \sigma_{||} = 3.89 \pm 0.08 \text{ GeV}. \tag{5.7}$$

We take $\bar{\sigma} = 3.94 \pm 0.06$ GeV, combining the two observations to sharpen a possible constraint on the model. The observed p_t of the W decays (see figure 5.3) has an average of 5.66 ± 0.11 and rms of 3.67 ± 0.08 GeV/c. We could use any **one** of these measurements to limit the variation of one parameter in our model. We include all of them as a demonstration of their relative strengths (and correlations). Where appropriate we include a table showing the variation of these parameters, even if we have used some other data for the constraint. This allows a comparison of the strengths of the constraints from other data relative to the W data itself.

5.2.1 Electron Resolution

The measurement of a typical electron ($E_t = 35$ GeV) introduces (see equation 5.2) a:

$$\sigma_e = \sqrt{(0.135 \cdot \sqrt{35})^2 + (0.02 \cdot 35)^2} = \sqrt{0.8^2 + 0.5^2} = 1.1 \quad \text{GeV} \tag{5.8}$$

smearing to our measurement. This is small compared to the 3 GeV resolution on the underlying event making the electron contribution negligible in this regard. As a check of the effect it has on the W mass we vary the constant term in the electron resolution from 2.0% to 1.5% and 2.5%. The $\pm 0.5\%$ variation is an upper limit on possible variations of this constant coming from our understanding of the calibrations described in section 4.2.

5.2.2 Underlying Event Resolution

We vary the constant of proportionality in equation 4.9 from 0.47 ± 0.01 constrained by minimum bias data. This constraint comes from measurements of $\sigma_{E_{x,y}}$ in our 300 000 event minimum bias sample. In doing this we see the changes in the observables outlined in table 5.1. The minimum bias data constraint is better than we could have placed on this parameter from the W data itself. Even though σ_{E_x} does not exactly scale with $\sqrt{\sum E_t}$ (there is a slight slope in figure 4.11), 2/3 of the observed W $\sum E_t$s fall in a range that is covered by this ± 0.01 variation in the constant of proportionality.

$\not\!\!E_t$ Smearing	W p_t (σ_{p_t})	$\bar{\sigma}$
Observed in Data	5.66 ± 0.11 (3.67 ± 0.08)	3.94 ± 0.06
$0.46\sqrt{\sum E_t}$ (-1"σ")	5.59 ± 0.01 (3.66 ± 0.01)	3.92 ± 0.01
$0.47\sqrt{\sum E_t}$ (nominal)	5.65 ± 0.01 (3.68 ± 0.01)	3.95 ± 0.01
$0.48\sqrt{\sum E_t}$ ($+1$"σ")	5.71 ± 0.02 (3.70 ± 0.01)	3.98 ± 0.01

Table 5.1: The constraints we place on the $\not\!\!E_t$ smearing from our study of minimum bias data. This table shows that this part of the model could not be constrained as well by the W underlying event measurements. All quantities listed are in GeV.

p_t Degradation (at $p_t = 0$)	W p_t (σ_{p_t})	$\bar{\sigma}$
Observed in Data	5.66 ± 0.11 (3.67 ± 0.08)	3.94 ± 0.06
2.6 ($+1$"σ")	5.42 ± 0.01 (3.52 ± 0.01)	3.86 ± 0.01
2.3 (nominal)	5.65 ± 0.01 (3.68 ± 0.01)	3.95 ± 0.01
2.0 (-1"σ")	5.94 ± 0.02 (3.86 ± 0.01)	4.06 ± 0.01

Table 5.2: The variation in underlying event observables due to the assumed W p_t degradation. These constraints come from our study of Z data. All quantities listed are in GeV.

5.2.3 Detector p_t Degradation

We vary the assumed degradation, at $p_t = 0$, from a factor of 2.3 ± 0.3. This range is limited by our study of Z data where we find varying by more than this results in one sigma disagreement with the Z data (the dotted lines in figure 4.15). Varying this parameter effectively changes the shape of the W p_t distribution used in the model. By varying this parameter we see changes in the underlying event observables outlined in table 5.2. If we could use the W data it would provide a slightly better bound on this parameter, however the correlation among the various underlying event observables means that we get only one constraint from the Ws and we use that constraint below.

5.2.4 "Jet" Resolution

We assume that the "jets" produced in our model behave as higher energy jets with resolutions of: $\sigma_{\rm jet} = 0.85\sqrt{p_t(\rm jet)}$. We study the range over which it is reasonable to vary this constant, 0.85, in the events underlying Zs, where we have a measurement of the true p_t(jet) from the decay di-leptons. We first un-fold (out of quadrature) the underlying event resolution on the activity associated with Z. We find that the resulting spread in p_t(jet) constrains us to $0.85 \pm 0.23(stat.) \pm 0.10(sys.)$ where the systematic uncertainty comes from varying the range of p_t(jet) we study in the Zs. A variation of ± 0.25 on this resolution is entirely adequate for constraining effects on the fit W mass (see section 6.3).

5.2.5 Absolute W p_t Variation

By using the constraints implied by the measurements listed in table 5.3 we limit the variation in the average W p_t to $\pm 4\%$. Changes larger than this drive the average W p_t and its rms into one sigma disagreement with the data (included in table 5.3 for comparison). The $\bar{\sigma}$ is not as sensitive to these variations since it is made up of equal parts spectator parton smearing (not being changed) and W p_t. The average W p_t is the only parameter in our model which we constrain from the W data. This is only a constraint within the context of our model and not (even in principle) a reflection of how well we might hope to measure the W p_t. In particular one sigma variations of the degradation alone (see above) can cause additional $\pm 11\%$ variations in the W p_t inferred from our model.

5.3 Fitting Procedure

We determine the mass (and width) of the W by comparing the transverse mass (see equation 2.16) of the $e\nu$ system to Monte Carlo predictions with m_W and Γ_W as parameters. We generate predictions for m_t, E_t^l, and $\not\!\!E_t^\nu$ (the latter two for checks of the model) for masses, m_W, between 77.8 and 82.3 GeV/c^2 in steps of 0.5 GeV/c^2 and widths, Γ_W, between 0.75

W p_t scaling	W p_t (σ_{p_t})	$\bar{\sigma}$
Observed in Data	5.66 ± 0.11 (3.67 ± 0.08)	3.94 ± 0.06
0.86 (-2.4"σ")	5.36 ± 0.01 (3.39 ± 0.01)	3.86 ± 0.01
0.91 (-1.2"σ")	5.50 ± 0.01 (3.53 ± 0.01)	3.91 ± 0.01
0.96 (nominal)	5.65 ± 0.01 (3.68 ± 0.01)	3.95 ± 0.01
1.01 ($+1.2$"σ")	5.81 ± 0.02 (3.76 ± 0.01)	4.01 ± 0.01
1.06 ($+2.4$"σ")	5.98 ± 0.01 (3.90 ± 0.01)	4.07 ± 0.01

Table 5.3: The constraints we place on the average W p_t used in our model from variation of observed W p_t and underling event energy spread. All quantities listed are in GeV.

and 6.0 GeV/c in steps of 0.75 GeV/c. Roughly 1000 times the number of W decays in the data sample go into the prediction of the line shape for each mass-width combination. The number of events we generate is constant, but the number surviving kinematic and fiducial cuts varies at the 1 % level. We store the distributions in 1 GeV/c^2 intervals, giving an m_t probability distribution, $P(m_W, \Gamma_W)$ as a function of m_W and Γ_W.

We compare the simulated line shapes to the data with an event by event likelihood. We maximize the likelihood:

$$\begin{aligned} L &= \Pi[P_i(m_W, \Gamma_W)], \\ \ln L &= \sum \ln[P_i(m_W, \Gamma_W)] \end{aligned} \tag{5.9}$$

as a function of mass and width with the MINUIT optimization package [56]. The product and sum extend over all events, i, in the W sample. Although we generate line shapes at discrete masses and widths, we interpolate in both quantities to provide a prediction for any mass and width. Several methods of interpolation (bilinear, polynomial, bi-cubic and bi-cubic spline [57]) give the same results. We use the bi-cubic spline, which consists of successive one dimensional interpolations. At each of the four grid points, surrounding the desired mass-width point, we specify the probability, P, the derivative in each direction, $\frac{\partial P}{\partial m_W}$ and $\frac{\partial P}{\partial \Gamma_W}$, and the cross derivative, $\frac{\partial^2 P}{\partial m_W \partial \Gamma_W}$. We determine the derivatives at the grid points with one dimensional splines. We then use a cubic polynomial to find an interpolated

value. Thus, with a finite number of line shape predictions we provide an approximately continuous prediction in m_W and Γ_W.

Naive $\sqrt{n}$ scaling would lead one to expect that the ultimate precision of our line shapes would be ≈ 20 ($\sqrt{400}$) times that of our data sample. This turns out to be not the case. Some precision is lost in the interpolative procedure outlined above. Fits to simulated samples (see chapter 6) of 500 000 events result in statistical uncertainties of $\approx 30 - 40$ MeV/c^2, only an improvement of 10 over the uncertainty on our data. This is one of the primary motivations for using a greatly simplified model of W production and detection to predict the mass. More sophisticated simulations are too slow (factors of 10-100 times slower than our model) to provide the necessary statistics for the fit.

Once we have the line shape for a requested mass and width we compute the probability, $P_i(m_W, \Gamma_W)$, that any individual event comes from this distribution by doing a linear interpolation between the nearest stored (in 1 GeV/c^2 intervals) probabilities. We also try a cubic spline interpolation here and find that it makes less than 20 MeV/c^2 difference to the fit mass. We fit only the shape of the distribution and not the number of events. The stored probabilities, P, are related to the absolute probabilities, P^{absolute}, by an interval normalisation, P^{interval}. This normalisation enters as a constant offset in $\ln L$ as follows:

$$\begin{aligned} -\ln L &= -\sum \ln(P_i^{\text{absolute}}/P^{\text{interval}}) \\ &= -\sum (\ln(P_i^{\text{absolute}}) - \ln(P^{\text{interval}})) \\ -\ln L &= -(\sum \ln(P_i^{\text{absolute}}) - \text{Constant}) \end{aligned} \tag{5.10}$$

The absolute probability is what determines the shape of the likelihood function ($\ln L$). The constant — related to our choice of storage interval in the line shape predictions — plays no role in the fit. The MINUIT package controls the optimization [†], seeking the minimum of $(-\ln L)$ and determining the statistical uncertainties. The shape of the likelihood surface around the minimum is shown in figure 5.6.

[†] For technical reasons we compute $-\ln L$, MINUIT prefers to optimize by finding minima.

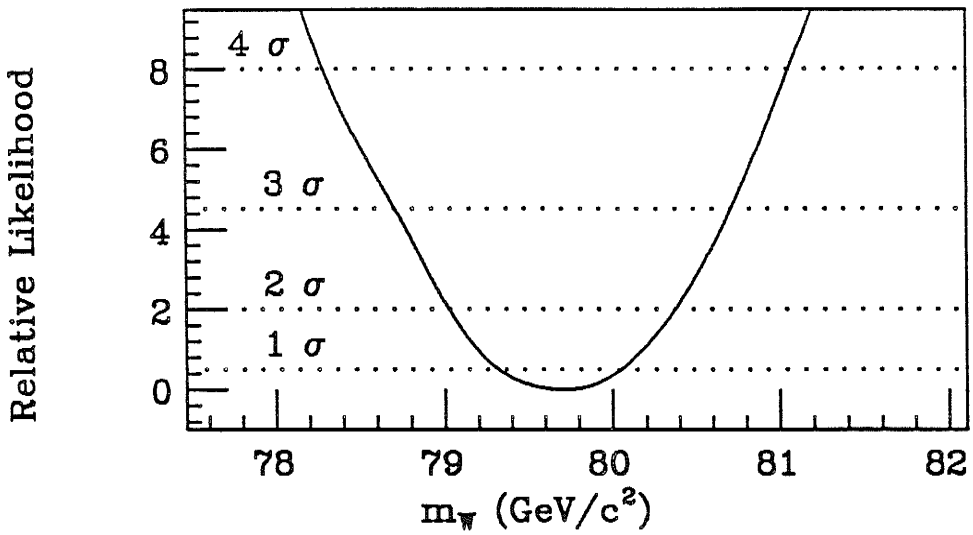

Figure 5.6: The likelihood value versus m_W for our standard m_t fit. The dotted lines show the 1 ($\delta L = 0.5$), 2 ($\delta L = 2$), 3 ($\delta L = 4.5$) and 4 ($\delta L = 8$) sigma statistical uncertainties on the mass measurement.

We define the statistical uncertainty of the fit as the change in fit parameter (mass or width) required to change $\ln L$ by 0.5. When extracting both a mass and a width the MINUIT package re-fits one parameter as it searches for values of the other where:

$$\ln L_{n\sigma} = \ln L_{\min} + 0.5\, n^2 \quad . \tag{5.11}$$

This re-fitting accounts for correlations between mass and width in determining the uncertainties. Further discussion of the statistical properties of our fits is found in section 5.4.

5.4 Checks of the Fit Procedure

Figure 5.7 shows the coupling between the fit mass and width. MINUIT reports a $20-40\%$ correlation between these parameters. This correlation is at the same time a correlation between mass and detector resolution. This is the subject of section 6.3.

We check the properties of our fit in several ways. The scan of the likelihood surface near the minimum shows a slight asymmetry. However the estimated statistical uncertainty is constant (within ± 40 MeV/c^2) out to 4 sigma (see figure 5.6 and table 5.4).

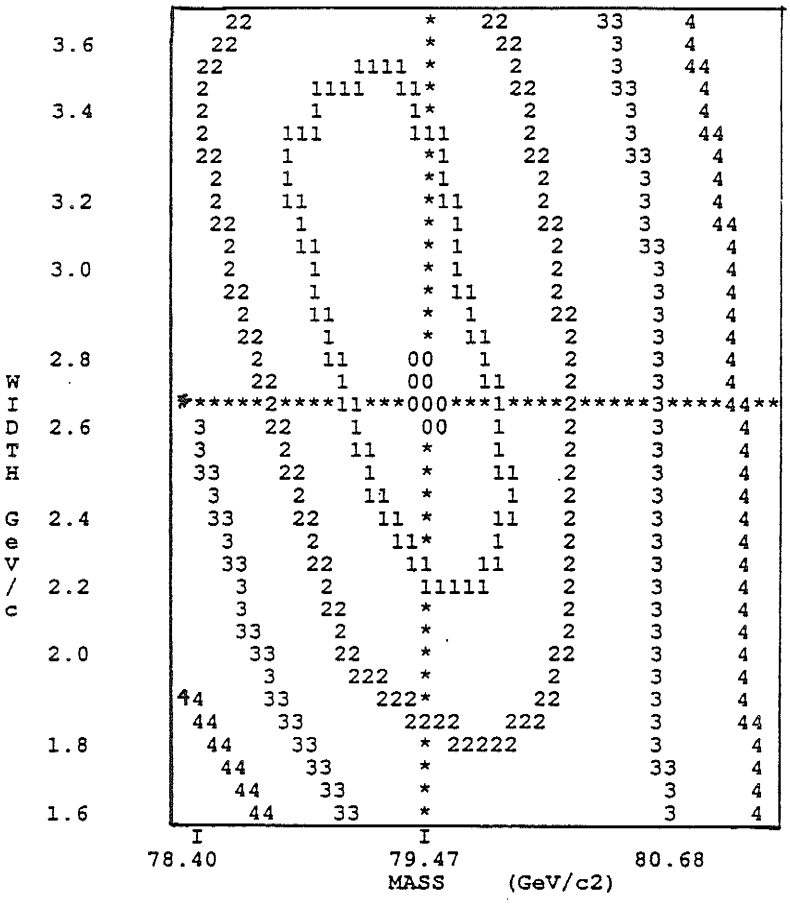

Figure 5.7: The likelihood contours between mass and width. The lack of alignment of the semi-major and semi-minor axes of the "ellipse" with the mass and width axes indicates the correlation between mass and width.

δL	Negative Error	Positive Error	Average
0.5 (1 σ)	-384	+345	363
2.0 (2 σ)	-296	+321	336
4.5 (3 σ)	-317	+335	333
8.0 (4 σ)	-424	+349	346

Table 5.4: Shows the n σ uncertainties above and below the fit mass along with the quadrature sum average of the two. These uncertainties are displayed out to 4σ. All uncertainties are in MeV/c^2.

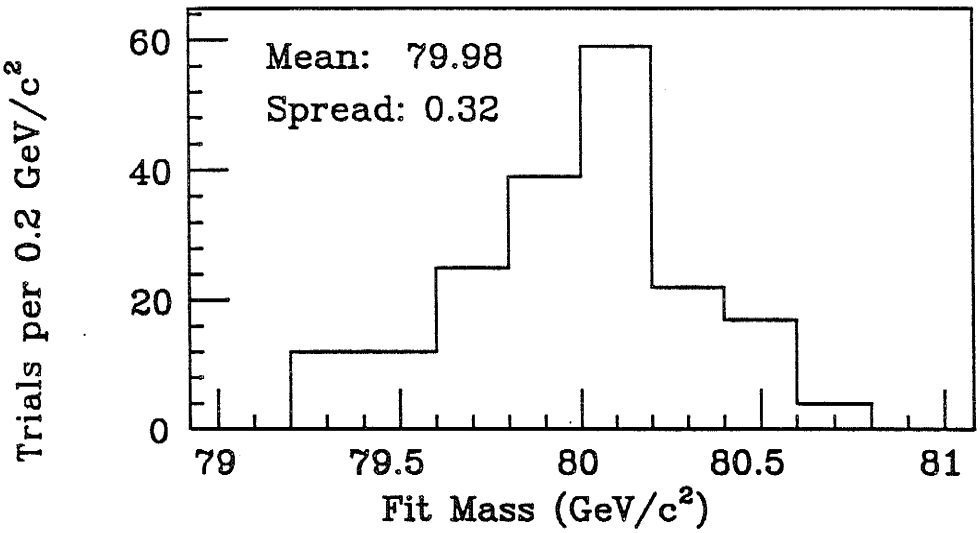

Figure 5.8: The spread in fit masses obtained from 200 trial experiments containing 1131 events (the number in our fit sample) each. We use the spread in this distribution to check the statistical uncertainty obtained from the MINUIT fits.

In another check we generate two hundred simulated samples with 1131 events (the size of our data sample) and fit each one. The mean mass from the fits, relative to the known generated mass (80.0 GeV/c^2) provides a test of the fitting procedure's reliability. The spread in the fit masses reflects the statistical precision of a sample of 1131 events. Figure 5.8 shows the distribution of fit masses when the width is fixed (at the value we generated: Γ_W = 2.2 GeV/c). Our statistical uncertainty, 340 MeV/c^2, is the consistent with the 320 MeV/c^2 spread of fit values seen in figure 5.8.

Chapter 6

Systematic Uncertainties

This chapter describes the systematic uncertainties in the W mass measurement. We include one correction made to the fit mass, and several checks of our fits. We vary the parameters in our line shape simulation, within the limits described in section 5.2, to see what effect they have on the fit mass. In this way we estimate potential systematic uncertainties. Among the parameters we vary are the parton distribution functions, the $\not\!\!E_t$ resolution, the electron resolution, the W p_t distribution and the underlying event energy degradation.

We check for effects of the selection criteria on the fit mass by studying a W sample selected for its electron characteristics. We change the way we limit jet activity, studying the effect of varying the W p_t distribution on our result. We study the effect of several potential backgrounds on our fit mass. We vary the range over which we fit m_t, to better understand how candidates on the high side of the distribution effect the fit. We look at the mass fit to W^+ and W^- separately, as well as time slices of the full data sample. We fit the electron E_t spectrum as well as the neutrino $\not\!\!E_t$ spectrum as a check of parts of the event that go into the transverse mass calculation. These provide checks of our fitting procedure.

Fit Variable	Radiative Shift
Invariant Mass	-70.7 ± 1.7
Transverse Mass	-51.4 ± 1.4
Electron Et	-47.0 ± 1.2
Neutrino Et	-49.6 ± 1.7

Table 6.1: Radiative shift on the fit W mass for various fitting variables. Uncertainties listed are statistical only. Shifts are in MeV/c^2.

6.1 Radiative Correction

Here we compute the radiative correction to the fit mass. We predict the angle and energy of radiated photons [51] in W decay. These photons can lower the observed electron energy — if they do not end up in the same cell of the calorimeter — and possibly effect the underlying event. We perform simple 4 vector calculations of the radiative shift to the fit variables. We check to see if the radiated photon overlaps with the electron adding its 4 vector to that of the electron if it overlaps — as the calorimeter would — and throwing it away if there is no overlap.

Table 6.1 shows the predicted shift to the fitting variables due to internal radiation. We study only the effect of internal radiation. External bremsstrahlung is collinear with the electron and hence measured in the same calorimeter cell — not lost. We included the effect of external radiation in our calibration. We also investigate the effect of stray photons on the neutrino measurement. To do this we assume that photons less than 1 GeV would be lost — this is a worst case assumption. When we make this assumption the neutrino fit mass is most sensitive, moving 2 MeV/c^2, m_t is less sensitive, hence we conclude that such losses alone cannot bias the mass measurement.

Though m_t is lowered an average of 50 MeV/c^2 by wide angle radiation, the fit mass is changed by 70 MeV/c^2 (the shift seen on the invariant mass). The difference reflects the fact that m_t is less sensitive to changes in the mass of the W than the full invariant mass. We

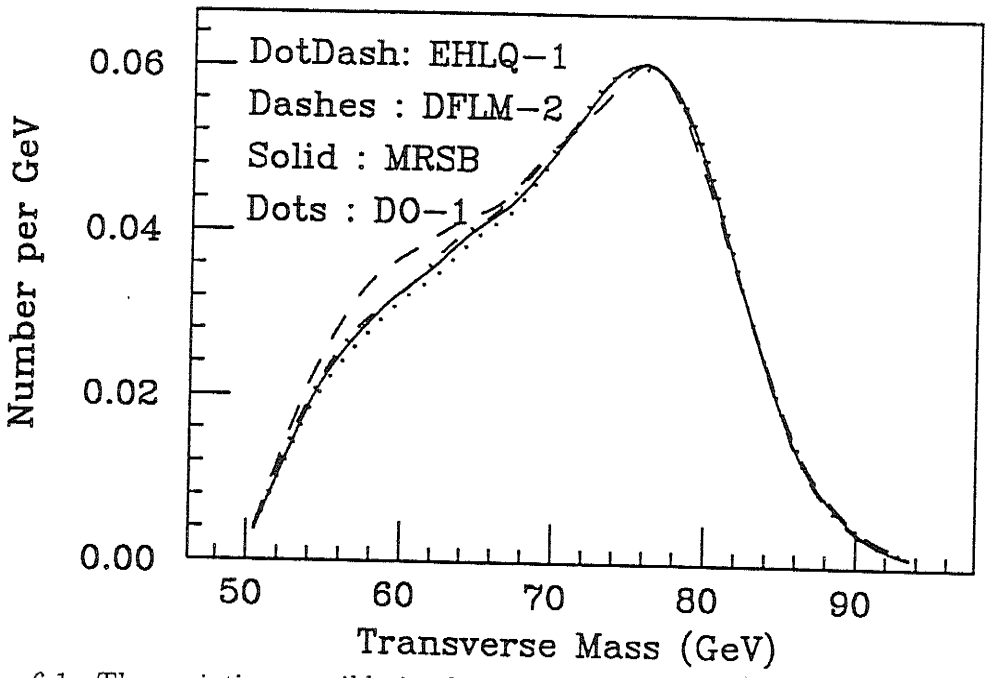

Figure 6.1: The variation possible in the m_t line shape due to changes in the choice of parton distribution function.

take a 10% systematic uncertainty on our radiative calculations. Here that introduces only a further 7 MeV uncertainty. Thus, the W mass, coming from our fits should be shifted up by 70 ± 7 MeV to account for wide angle photons not included in our line shape simulation.

6.2 Parton Distribution Functions

We vary the parton distribution functions used to simulate W production among several reasonable choices. We test EHLQ-1[58], DO-1, DO-2[59], DFLM-1, DFLM-2, DFLM-3[60], MRS-B and MRS-E [61] as a sample of the different possible proton structure assumptions we could make. MRS-B is our standard choice; we use it in all fits except for those described in this section.

Varying the assumed structure of the proton varies the W longitudinal momentum distribution. When coupled to the V-A decay of the W this changes the rapidity distribution of the decay charged leptons. This is one of the factors determining the shape of the Jacobian peak. Figure 6.1 shows how the shape varies with choice of parton distribution. As the W is

Lower cutoff	Data	MRS-B	EHLQ-1	DO-1	DFLM-2
55 GeV	79.65 ± 0.37	80.01 ± 0.03	79.88 ± 0.03	80.07 ± 0.03	79.94 ± 0.03
60 GeV	79.65 ± 0.36	80.02 ± 0.03	79.90 ± 0.03	80.06 ± 0.03	79.96 ± 0.03
65 GeV(nom.)	79.71 ± 0.34	80.01 ± 0.03	79.90 ± 0.04	80.00 ± 0.03	79.94 ± 0.04
70 GeV	79.67 ± 0.40	80.03 ± 0.04	79.89 ± 0.04	79.95 ± 0.04	79.94 ± 0.04

Table 6.2: Comparison of mass fit values for various choices of lower cutoff. The first column shows the effect of varying the lower cutoff on the fit to the data. The last four columns show how varying this cutoff effects fits to large MC samples created with different proton parton distribution functions. All masses listed are in units of GeV/c^2.

PDF choice	Monte Carlo
MRS-B (nominal)	80.01 ± 0.03
MRS-E	80.00 ± 0.03
DFLM-1	79.96 ± 0.03
DFLM-2	79.94 ± 0.04
DFLM-3	79.97 ± 0.03
DO-1	80.00 ± 0.03
DO-2	79.99 ± 0.03
EHLQ1	79.94 ± 0.03

Table 6.3: Monte Carlo comparison of masses fit for different parton distribution functions. All masses listed are in units of GeV/c^2.

boosted along the beam the m_t distribution is washed out. A simulation of the longitudinal motion of the Ws and the detector's θ acceptance is important to understand the shape of the peak.

With O(350) MeV/c^2 statistical uncertainties associated with fits to the data it is hard to quantify systematic effects smaller than a few hundred MeV/c^2. To avoid this we study high statistics Monte Carlo samples. We base the systematic uncertainty estimates in the next few sections on fitting these altered Monte Carlo samples to our nominal line shapes. Here we generate one Monte Carlo sample (with $m_W = 80.0$) for each of the parton distributions tested. We smear this sample with our nominal model of detector resolution and W p_t. We

then fit these samples with our standard line shapes — using the MRS-B parton distribution set as a reference — to give the values in tables 6.2 and 6.3.

Table 6.2 shows that the mass is reasonably insensitive to the choice of lower cutoff. We choose 65 GeV to limit our sensitivity to the choice of parton distribution function and further reduce the potential background in our fits (see section 6.6 below).

The spread in fit masses in table 6.3 is 50 MeV/c^2. The EHLQ-1 set makes the maximum excursion (70 MeV/c^2 lower than the nominal fit — MRSB). We believe that the different u/d quark ratios in these distribution functions are the cause of the mass differences. Recent data [62] disagrees with the predictions of the ELHQ-1 distribution for the u/d ratio at the 2σ level [63]. None the less we conservatively include the EHLQ measurement and take a 60 MeV/c^2 systematic uncertainty to account for our choice of parton distribution function. This is entry (2) in table 6.11.

6.3 Detector Resolution and W p_t Distribution

The Jacobian line shape couples the mass and the detector resolution. Qualitatively, increasing the resolution smears and lowers the upper edge of the m_t distribution. This increases the fit mass necessary to bring the simulated edge into agreement with the data. We described constraints on the observed resolution in section 5.2. An additional complication in the fit of the W mass is the correlation among several "resolution"-like variables. The $\not\!\!E_t$ resolution, the $E_t{}^e$ resolution, the W p_t distribution and the Lorentzian width of the W all broaden the Jacobian peak changing the fit mass.

We vary the assumed $\not\!\!E_t$ resolution, W p_t degradation, mean W p_t, jet resolution and underlying event energy correction in the same way as the parton distribution functions, that is we simulate Monte Carlo samples with each piece of the model separately altered to its extreme. We summarize the results in tables 6.4 through 6.8. Because we have residual fit fluctuations of order 50 MeV/c^2 (see section 6.6) we also study the behaviour of the mass

$\not\!\!E_t$ Smearing	Fit to Monte Carlo
$0.44\sqrt{\sum E_t}$ (-3"σ")	80.10 ± 0.03
$0.46\sqrt{\sum E_t}$ (-1"σ")	80.05 ± 0.03
$0.47\sqrt{\sum E_t}$ (nominal)	80.01 ± 0.03
$0.48\sqrt{\sum E_t}$ ($+1$"σ")	79.99 ± 0.03
$0.50\sqrt{\sum E_t}$ ($+3$"σ")	79.94 ± 0.03
1"σ" variation: 0.027.	

Table 6.4: The comparison of mass fit values for various choices of $\not\!\!E_t$ resolution. All masses are listed in GeV/c^2.

Degradation at $p_t = 0$	Fit to Monte Carlo
1.4 (-3"σ")	79.91 ± 0.03
2.0 (-1"σ")	79.96 ± 0.03
2.3 (nominal)	80.01 ± 0.03
2.6 ($+1$"σ")	80.08 ± 0.03
3.2 ($+3$"σ")	80.18 ± 0.03
1"σ" variation: 0.047.	

Table 6.5: The comparison of mass fit values for various choices of W p_t degradation. All masses are listed in GeV/c^2.

with $\pm 3\,\sigma$ variations of each parameter in the model. A line is fit to the 5 measurements listed, in each table, to determine the mass dependence of each parameter.

We combine the individual mass variations (due to the variation of independent model parameters) in quadrature to conclude that our model of the detector resolution on the underlying event and p_t of the W could result in mass shifts, δ_m:

$$\begin{aligned} \delta_m &= \sqrt{27^2(\text{minb.}) + 17^2(Wp_t) + 47^2(\text{deg.}) + 43^2(\text{jet res.}) + 18^2(\text{jet energy})} \\ &= 73\ \text{MeV/c}^2. \end{aligned} \tag{6.1}$$

Like the $\not\!\!E_t$ resolution we vary the electron energy resolution to see how it affects the fit mass. We assume the electron resolution scales with energy according to equation 5.2. We have studied the term which scales with energy, a, in testbeam measurements and believe it

Fraction of p_tW	Fit to Monte Carlo
0.84 (-3"σ")	79.94 ± 0.03
0.92 (-1"σ")	79.96 ± 0.03
0.96 (nominal)	80.01 ± 0.03
1.00 ($+1$"σ")	79.99 ± 0.03
1.08 ($+3$"σ")	80.04 ± 0.03
1"σ" variation: 0.017.	

Table 6.6: The comparison of mass fit values for various choices of absolute W p_t. All masses are listed in GeV/c^2.

Jet resolution constant	Fit to Monte Carlo
0.10 (3"σ")	79.92 ± 0.03
0.60 (1"σ")	79.96 ± 0.03
0.85 (nominal)	80.01 ± 0.03
1.10 (1"σ")	80.04 ± 0.03
1.60 (3"σ")	80.18 ± 0.03
1"σ" variation: 0.043.	

Table 6.7: The comparison of mass fit values for various choices of modelled jet resolution. All masses are listed in GeV/c^2.

Jet Energy/Momentum const.	Fit to Monte Carlo
1.0 (-3"σ")	80.05 ± 0.03
1.2 (-1"σ")	80.04 ± 0.03
1.4 (nominal)	80.01 ± 0.03
1.8 ($+1$"σ")	79.99 ± 0.03
2.2 ($+3$"σ")	79.95 ± 0.03
1"σ" variation: 0.018.	

Table 6.8: The comparison of mass fit values for various choices of jet energy-momentum proportionality. This effect is non-linear in the constant being varied so the references to $n\sigma$ are notional only. The overall effect is small however, so our overall model systematic is not relying on the details of this notion. All masses are listed in GeV/c^2.

$\sigma_{E_t}^{constant} \equiv b$	Fit to Monte Carlo
0.5% (-3"σ")	79.87 ± 0.03
1.5% (-1"σ")	79.96 ± 0.03
2.0% (nominal)	80.01 ± 0.03
2.5% ($+1$"σ")	80.10 ± 0.03
3.5% ($+3$"σ")	80.29 ± 0.03
1"σ" variation: 0.070.	

Table 6.9: The comparison of mass fit values for various choices of electron resolution. All masses are listed in GeV/c^2.

to be well determined. The constant term, b, is less well constrained. From the calibrations described in section 4.2 we constrain it to $\pm 0.5\%$. This range in b may also model small changes in a.

We vary the electron resolution constant, b from its nominal value ($\sigma_{E_t}^{constant} = 2.0\%$) to an over smeared value at 2.5% and an under smeared one at 1.5%. We summarize the results in table 6.9

We conclude that a one "σ" variation in the electron resolution can shift the fit mass by 70 MeV/c^2. We add this in quadrature with the underlying event component (see equation 6.1) to arrive at our overall uncertainty due to uncertainties in our model of 100 MeV/c^2. This is entry (3) in table 6.11.

6.4 Electron Subtraction Uncertainty

There are effects outside the scope of our model which can shift the fit W mass. The largest of these comes from the separation of the electron from the rest of the event, described in section 4.3. We are able to measure $< \not{p}_{||} >$ with 115 MeV/c^2 accuracy (see figure 4.12). We make a correction to the model for residual biases in this subtraction (the effect of the di-jet cut, etc.). This correction is only determined to ± 115 MeV/c^2 (the accuracy of the data). An uncertainty in $< \not{p}_{||} >$ enters directly into the predicted m_t. As with the radiative

correction, shifts in m_t are smaller than shifts in m_W (by a factor of $\approx 8/7$). Hence we conclude that there is an independent 130 MeV/c^2 uncertainty in the fit W mass. This is not accounted for by the variations in the model, since we made no attempt to predict the $\not\!\!E_{||}$ distribution, but constrained the model to agree with our observed $\not\!\!E_{||}$. This is entry (4) in table 6.11.

6.5 Check of Fit Range

Another potential uncertainty comes from our choice of fit range. The lower cutoff is motivated by our understanding of backgrounds and the effect of varying parton distribution functions. We have 11 electron candidates with $m_t > 94$ GeV/c^2. Our simulation predicts 3. We attribute the excess seen in the data to high p_t Ws in our sample, where all evidence for the jet associated with the boost of the W is lost. We consider this discrepancy evidence for non-Gaussian tails in our $\not\!\!E_t$ and jet resolutions, however we check that at this level ($\leq 1\%$ (or 8 events) of our sample is affected in this way) such tails in the resolution function do not change the W mass. By imposing an upper cutoff (taken nominally to be $m_t = 94$ GeV/c^2) we limit the effect the tails of the resolution functions have on the fit mass. In table 6.10 we display the dependence of the fit mass on the choice of upper cutoff. The comparison to Monte Carlo fits provides an indication of the reliability of the fit when changing the upper cutoff. The variation seen in table 6.10 is simply the result of statistical fluctuations resulting from the inclusion (or exclusion) of events in the m_t tail. This check does not reveal an independent uncertainty in the W mass measurement.

This study also indicates to what extent the various parts of the m_t distribution contribute information to the fit. From the fits with the width floated it is clear that most of the information used to fit the width is in the tail of the distribution. For m_t cutoffs of 92 GeV/c^2 and below the width suffers large fluctuations and the statistical precision deteriorates rapidly. Even the mass values are effected if the cutoff is lowered much below 92 GeV/c^2 as the fits to the Monte Carlo samples indicate. This study emphasizes the

Width Floated				
Cutoff (GeV/^{2})	Fit to Data (m_W; Γ_W)	χ^2/dof		Fit to Monte Carlo
98	79.49 ± 0.38 ; 2.7 ± 0.5	34.2/32		79.98 ± 0.05 ; 2.29 ± 0.07
96	79.47 ± 0.42 ; 2.8 ± 0.6	33.3/30		79.96 ± 0.05 ; 2.31 ± 0.08
94 (nominal)	79.42 ± 0.40 ; 2.9 ± 0.6	31.2/28		79.98 ± 0.05 ; 2.39 ± 0.10
92	79.31 ± 0.38 ; 3.2 ± 0.8	28.4/26		79.95 ± 0.05 ; 2.43 ± 0.11
90	79.31 ± 0.35 ; 3.7 ± 1.0	23.7/24		79.92 ± 0.09 ; 2.59 ± 0.34
Width Constrained				
Cutoff (GeV/c^2)	Fit to Data (m_W)	χ^2/dof		Fit to Monte Carlo
98	79.72 ± 0.36	37.1/33		80.01 ± 0.03
96	79.69 ± 0.36	36.2/31		80.03 ± 0.03
94 (nominal)	79.71 ± 0.34	35.4/29		80.01 ± 0.03
92	79.73 ± 0.38	35.1/27		80.04 ± 0.04
90	79.71 ± 0.36	27.2/25		80.01 ± 0.04

Table 6.10: The comparison of mass and width fit values for various choices of upper cutoff of fit range. All masses are listed in GeV/c^2 and widths in GeV/c.

relative importance of the falling edge and m_t tail (especially above 90 GeV/c^2) to the measurement.

6.6 Other Contributions to the Systematic Uncertainty

We consider other contributions to the W mass systematic uncertainty. We study the potential backgrounds in the sample and the effect they could have on the mass. We also quantify the remaining uncertainty due the mechanics of fitting.

The presence of background in the W sample is a source of concern. We consider several sources of background. The sequential decay of τs (from Ws) into electrons mimics the direct decay into electrons, however, these events are concentrated at low m_t (see figure 6.2a). We simulate a large sample of these sequential decays (using the ISAJET(V6.12) [64] $p\bar{p}$ physics simulation) and conclude that only 4 events should enter our sample, while only 1.5 events enter our fit (having $m_t \geq 65$ GeV/c^2). By subtracting 20 times the predicted τ background

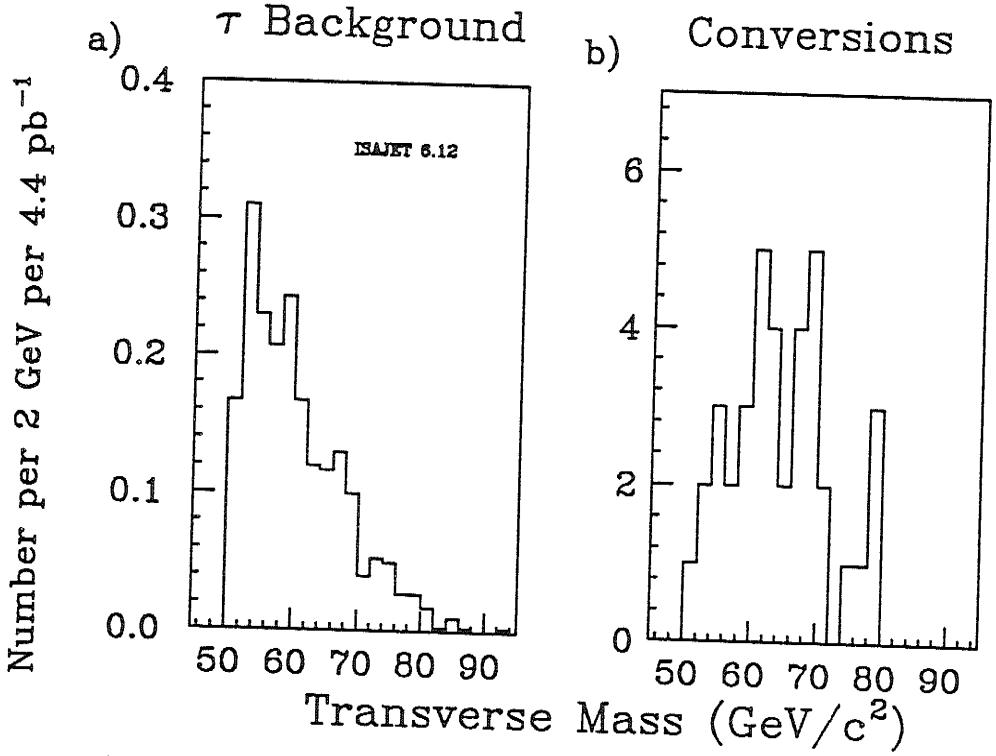

Figure 6.2: a) The ISAJET (V6.12) prediction of the m_t distribution for electrons from the sequential decay $W \rightarrow \tau \rightarrow e$. These exhibit a softer m_t distribution and could shift the mass downwards since they are not included in the fit. However their relative under abundance makes this shift 4 MeV/c^2. b) The m_t distribution of conversion candidates selected by our filter. These are consistent with the over efficiency of our filter (having a 5% probability of identifying real W electrons). When added to the fit sample the mass changes by 40 MeV/c^2.

we find an upwards shift of 80 MeV/c^2 in the fit W mass. This leads us to conclude that τs only cause a 4 MeV/c^2 shift in our fit mass.

A more plentiful source of potential background comes from our photon conversion analysis [39] (see section 4.1.3) which eliminates 3.5% of the events which would otherwise be in our sample (see figure 6.2b). The filter is known to be 5% over-efficient, having that probability of rejecting real electrons. Thus our 3% loss is consistent with none of the events in figure 6.2b coming from photon conversions. The filter under-efficiency is 20% so we believe that less than 1% background remains. To study the possible effect of this background we restore all conversion candidates to our sample: the fit mass is lowered by 40 MeV/c^2.

Another source of background in our sample is Z events where one of the charged leptons is lost. This could be an important background as Z charged leptons can have higher m_ts. However, the cross-section for Z production is 10 times lower than that of W production [41] decreasing the importance of this background dramatically. The jet veto (see section 4.1.3) limits second electrons to E_t less than 7 GeV. This is unlikely for Z decays. We remove two events with second tracks having $p_t \geq 40$ GeV/c and find no other tracks between 10 and 40 GeV/c. We simulate the production and decay of Zs and expect only 1 event to contaminate our W sample. The Zs which survive have low m_t similar to those of the τs. From the study of τ decays we conclude this will have a negligible effect on our fit mass.

Finally we study the effect of a flat background on the fit mass. Adding a 1% background of this form shifts the mass up by 70 MeV/c^2. We believe we have $1 \pm 1\%$ background in our sample. A flat background is a worst case shape — most backgrounds (from QCD for example) fall with m_t reducing the effect they have on the fit mass. We take 50 MeV/c^2 as the potential uncertainty in the W mass due the presence of background. This is entry (5) in table 6.11.

A study of tables 6.4 through 6.9 reveals that jumps of O(50) MeV/c^2 are possible in the fits to large MC samples. These discrepancies are the reason for including 3"σ" variations in the study of the model — an attempt to ensure that the variations exhibited there, truly reflect the physics of varying the model and not the mechanics of fitting. We also generate two statistically independent sets of line shapes which give fits differing by less than 50 MeV/c^2. We vary the spacing between generated masses and widths in our simulation and see changes of less than 50 MeV/c^2. Thus we take an additional 50 MeV/c^2 systematic uncertainty due to the fit mechanics. This is entry (6) in table 6.11.

Uncertainty	Electrons	Muons
Statistical	340 (400)	510 (600)
1. Energy scale		
Tracking chamber	160	160
Calorimeter	260	0
2. Proton structure	60	60
3. Resolution, W p_t	100	100
4. Charged lepton subtraction	130	180
5. Background	50	200
6. Fitting	50	50
Overall Systematic	360	340
Overall	500(540)	620(700)

Table 6.11: Uncertainties in fitting the W mass. All uncertainties are quoted in units of MeV/c^2. In brackets are the statistical (and overall) mass uncertainties if Γ_W is determined in the fit as well. The uncertainties for the muon measurement (where they differ from the electron measurement) come from reference [43].

6.7 Consistency Checks

We check the fits in many ways. We study the effect of the event selection on the fit mass by fitting a sample selected primarily for its electron qualities. We study the effect of the jet cut. We vary our arbitrary choice of underlying event enhancement factor (nominally 1.4) and study the effect of introducing correlations between the underlying event energy and the p_t of the W. Fits to various subsets (charge, date of collection, location of electron) give consistent results. Finally fits to the electron E_t spectrum and neutrino $\not\!\!E_t$ spectrum give similar fit masses. We find no evidence for further systematic uncertainties in any of these fits.

We check for event selection biases by fitting a sample of events selected primarily for its electron characteristics (as opposed to our reference sample based on $\not\!\!E_t$). The event selection described in section 4.1.1 and 4.1.2 is replaced by those used to select the inclusive electron sample (described in section 4.2). To get from the inclusive electrons to a comparable mass sample we apply the selection criteria described in section 4.1.3. This results in a second sample of 1128 W decay candidates. 1018 of these candidates are shared with our original sample. The other 110 are plotted in figure 6.3b. For comparison the 113 events unique to our standard sample are shown in figure 6.3a. We find that this "electron" sample gives a fit mass of 79.81 ± 0.37 GeV/c^2. This is a 100 MeV shift. This change in the fit mass is attributable to the different events in the two samples. This shift is already accounted for in the statistical uncertainty on the measurement. We find no evidence for selection biases in this test.

We study the effect of the jet cut on the measurement. To do this we select another sample from the 1616 events in figure 4.4. Instead of the jet cut, we require the p_t of the W to be less than 20 GeV/c. This results in a 1420 event sample. We repeat the exercise of determining an appropriate input W p_t distribution for this new sample. Figure 6.4 shows input and output p_t distributions. This is to be compared with figure 5.3 for our

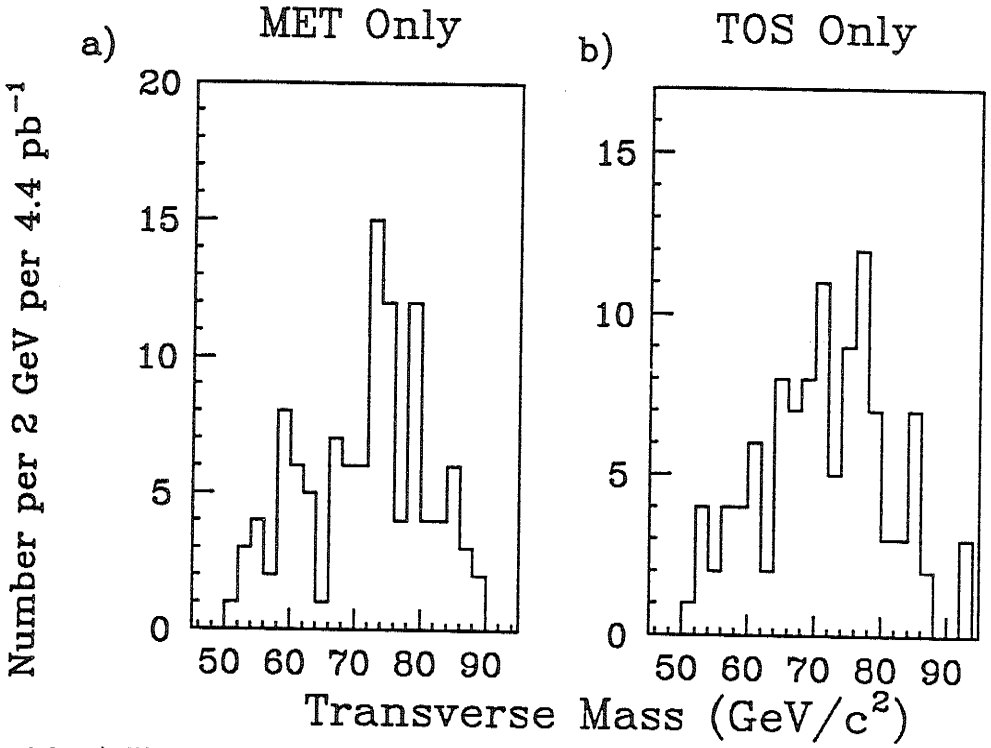

Figure 6.3: a) The W mass candidates found only in the $\not\!\!E_t$ W sample (described in sections 4.1.1 through 4.1.3). b) The W mass candidates found only in the electron W sample.

standard sample. The mean p_t in this case is 6.8 GeV/c (to be compared with 5.6 GeV/c in our standard sample) and the shape of the input distribution is very different. We fit $m_W = 79.63 \pm 0.33$(stat.) GeV/c^2 for this sample and model. Again we find no evidence in this shift for additional systematic effects and ascribe the difference to the inclusion of 300 new events in our sample. The systematic variations possible within this model are larger than in our standard model increasing the overall systematic uncertainty slightly. Hence we choose not to do the final analysis in this way.

We study the effect of scaling the underlying event energy by a factor of 1.4 (see section 4.3) by changing the factor from 1.0 to 1.8. When we use the raw (uncorrected) underlying event energy (an enhancement factor of 1.0) we find a fit mass value of 79.87 ± 0.35 GeV/c^2. When we try to better match the mean p_t of the W (by including an enhancement factor of 1.8) we find a fit mass value of 79.86 ± 0.44 GeV/c^2. We note that re-scaling the underlying event has the effect of rearranging the events as m_t changes differently (with

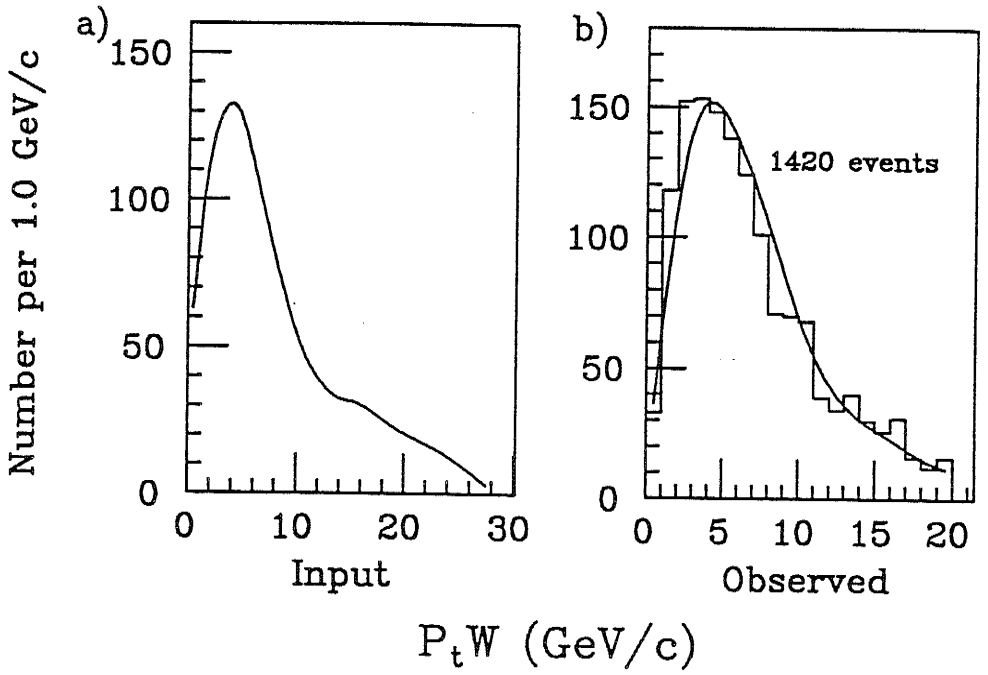

Figure 6.4: a) The p_t distribution of the W candidates (with $p_t \leq 20.0$ GeV/c rather than those having jets smaller 7.0 GeV) unfolded from the observed distribution (figure b) using the model. b) The agreement between the observed W p_t distribution and the model's prediction for this alternate sample.

more or less underlying event enhancement) for each event depending on the angle between the W and the electron. Again we ascribe the changes in fit mass to statistical fluctuations coming from the different underlying event rearrangements. The choice of underlying event enhancement factor is arbitrary — our model describes the physics of the uncorrected and corrected underlying events equally well. Studies of simulated samples with different enhancement factors show no change in the fit mass when we change this enhancement. We take no additional systematic uncertainty for the shifts in fit mass observed in the above fits.

We split the data into sub-samples by charge, detector sub-section and date of collection to see if this brings any systematic shifts to light. The W^+ candidates give a fit mass of 79.64 ± 0.48 GeV/c^2 while the W^- candidates fit 79.44 ± 0.52 GeV/c^2. Ws depositing their decay electron in the east half of the detector give a fit mass of 79.85 ± 0.53 GeV/c^2, while those in the west give 79.38 ± 0.39 GeV/c^2. Data from the first half of the run gives a mass

of 79.63 ± 0.47 GeV/c^2, while the second half gives a mass of 79.71 ± 0.41 GeV/c^2. All uncertainties quoted here are statistical only. We find no evidence for systematic shifts in these fits.

The electron E_t spectrum is shown in figure 5.2a. The best fit (shown as an overlay) is for a mass of 79.88 ± 0.34(stat.) GeV/c^2, however the shape of the electron spectrum is sensitive to the assumed W p_t distribution. Studying the effect of different W p_t distributions is a two step process. Our entire model is used to unfold the input p_t distribution of the Ws. Tests like those described in section 6.3 vary only one parameter of the model at a time. The electron is entirely insensitive to all parts of the model except the W p_t and the electron resolution. To get a true representation of the systematic uncertainty we must first vary other parameters in the model * and then extract a new input W p_t distribution (as was done to arrive at figure 5.3a). Finally we vary the p_t as described above for the m_t fits and find changes of 250 MeV/c^2 in the fit mass from the electron E_t spectrum. The calibration, proton structure, background and fitting uncertainties effect the electron E_t fit in the same way as the m_t fit. The electron energy subtraction (from the underlying event) does not effect the fit to the E_t spectrum. Thus we get a 400 MeV/c^2 overall systematic uncertainty on the electron E_t fit. We conclude:

$$m_W^e(\text{fit}) = 79.88 \pm 0.34(\text{stat.}) \pm 0.40(\text{sys.}) \text{ GeV/c}^2. \tag{6.2}$$

We also fit the neutrino $\not\!\!E_t$ spectrum. Here we conclude:

$$m_W^\nu(\text{fit}) = 80.16 \pm 0.61(\text{stat.}) \pm 0.51(\text{sys.}) \text{ GeV/c}^2. \tag{6.3}$$

The neutrino distribution is much more sensitive to the modelling of the underlying event and detector resolution, thus the overall systematic uncertainty of this measurement is larger. We see variations of ± 200 MeV/c^2 between the fits to these three different kinematic projections of the W decays (m_t, E_t and $\not\!\!E_t$). The consistency of these fits lend credibility

*It turns our varying the degradation factor has the largest effect. In practice we vary only this before extracting a new W p_t distribution.

to the m_t result. We attribute the discrepancies to the larger systematic uncertainties of the lepton E_t fits, rather than uncertainties in the W mass obtained from the fit to the m_t distribution.

6.8 Final Electron W Mass Measurement

We make one correction to our best fit W mass. The radiative correction described in section 6.1. We add 70 MeV/c^2 (see table 6.1) to the final fit value: 79.71 ± 0.34 GeV/c^2 (see figure 5.1). Thus we arrive at our final result from the fit to the W electron m_t distribution:

$$m_W = 79.78 \pm 0.34(\text{stat.}) \pm 0.19(\text{sys.}) \pm 0.30(\text{scale}) \quad \text{GeV/c}^2. \tag{6.4}$$

The combination of this result with the muon result as well as other electroweak data is the subject of the final chapter of this thesis.

Chapter 7

Results

This chapter describes the extraction of our final W mass value and the Standard Model parameters which depend on it. A discussion of the combination of the muon and electron results is included with a description of the treatment of correlated uncertainties. $\mathrm{Sin}^2\theta_W$ (see equation 2.4), the m_{top} it implies (see figure 2.3) and their uncertainties are extracted.

7.1 Combined W Mass

Although this thesis has concentrated on the description of the W mass measurement made with the $W \rightarrow e\nu$ candidates we make a similar measurement with $W \rightarrow \mu\nu$ candidates. Table 6.11 lists the uncertainties on each measurement following the discussion of chapter 6. From table 6.11 we can also see the correlations between the measurements. For example, the calibration of the tracking chamber enters both measurements at the 0.2% level (160 $\mathrm{MeV/c^2}$). By the same token the parton distribution function uncertainties and those on the neutrino resolution are common to both measurements. The uncertainty on the charged lepton subtraction comes from independent measurements hence we treat this as an independent uncertainty. Similarly the backgrounds are very different for the two sample hence we treat these uncertainties as independent. These are combined (for the muon and electron measurements) in the last column of table 7.1. We account for these correlations

Measurement	Mass	CTC	CEM	ν	ind. W
$m^e_{l\nu}$ (CDF)	79.78 ± 0.34	0.16	0.26	0.13	0.14
$m^\mu_{l\nu}$ (CDF)	79.60 ± 0.51	0.16		0.13	0.27
m^e_Z (CDF)	91.18 ± 0.34	0.18	0.30		
m^μ_Z (CDF)	90.70 ± 0.41	0.18			
m_Z (LEP)	91.10 ± 0.06				

Table 7.1: Summary of the vector boson mass measurements and uncertainties. All numbers listed are in units of GeV/c^2. No correlation between the CDF measurements and the LEP measurement is implied.

in combining the two measurements.

One further piece of information which might have been useful in extracting our best W mass is the LEP Z mass. It turns out to be unhelpful (see equations 7.1 and 7.2). We measure the Z mass with the CDF detector [44]. By comparing our measurement of m_Z to the measurements of the LEP experiments ([45, 46, 47, 48]) * we override our calibration uncertainties on the W mass in favour of the other uncertainties — primarily statistical — in the CDF Z mass measurement. Table 7.1 lists all the measurements of interest and summarizes the correlations among the uncertainties. The statistical uncertainties are not correlated. The column labelled 'CTC' includes the tracking chamber mass scale uncertainty. This uncertainty is common to the four CDF measurements. The column labelled 'CEM' includes only that part of the calorimeter calibration due to the E/P matching (see section 4.2) and hence is only applicable to the electron measurements. The column labelled 'ν' includes all common uncertainties to the muon and electron measurements of the W mass (namely uncertainties 2, 3 and 6 in table 6.11). The last column indicates uncertainties which are unique to each W mass measurement (uncertainties 4 and 5 in table 6.11), these are treated

*The LEP measurement is a weighted average of the four Z mass measurements.

as independent uncertainties.

We combine these numbers in two ways. First, from the CDF measurements alone, we conclude:

$$m_W^{e,\mu} = 79.71 \pm 0.42 \text{ GeV/c}^2 \qquad (\text{with } m_Z = 90.92 \pm 0.35 \text{ GeV/c}^2). \tag{7.1}$$

The uncertainties on m_W and m_Z are a combination of statistical and systematic uncertainties. They are partially correlated due the presence of common scale uncertainties. We elaborate on this correlation below when we extract the weak mixing angle.

In order to compare our result to the UA2 measurement we extract a W mass in another way. We include a constraint to the Z mass from LEP. The constraint is only as good as the CDF measurement of the Z mass (non-scale errors). When we include the LEP constraint we find:

$$m_W^{\text{CDF+LEP}} = 79.79 \pm 0.44 \text{ GeV/c}^2 \qquad (\text{with } m_Z = 91.10 \pm 0.06 \text{ GeV/c}^2). \tag{7.2}$$

For comparison UA2 find [9]:

$$m_W^{\text{UA2+LEP}} = 80.43 \pm 0.50 \text{ GeV/c}^2, \tag{7.3}$$

when they constrain their data in the same way. We can combine our result with that of UA2 to improve (slightly) on the measured W mass [†]. We find:

$$m_W^{CDF+UA2+LEP} = 80.04 \pm 0.33 \text{ GeV/c}^2. \tag{7.4}$$

There is not much difference between the results in equations 7.1 and 7.2. The Standard Model physics we extract either way is identical. Taking the result in equation 7.1 we conclude that:

$$m_W^{\text{CDF}} = 79.71 \pm 0.42 \text{ GeV/c}^2. \tag{7.5}$$

[†]Assuming as much as 100 MeV/c^2 of the individual W mass uncertainties are common (for the parton distributions and underlying event models) makes no difference to the combined result.

7.2 Standard Model Parameters

Following the discussion in chapter 2 there are two parameters of the Standard Model which we can extract from the W mass measurement.

The first is the mixing angle of the electroweak sector of the Standard Model (θ_W). Knowing the W and Z masses we extract the mixing angle from equation 2.4. $\mathrm{Sin}^2\theta_W$ is the most often quoted number. The uncertainty on this quantity can be derived with elementary calculus to be:

$$\sigma_{\sin^2\theta_W} = \frac{2\,m_W^2}{m_Z^2} \sqrt{(\frac{\sigma_W}{m_W})^2 + (\frac{\sigma_Z}{m_Z})^2} \tag{7.6}$$

where σ_W and σ_Z are the uncorrelated parts of the W and Z mass uncertainties, respectively. An error in the calibration of the detector would shift the W and Z masses the same amount. This would not change the mass ratio, leaving $\sin^2\theta_W$ (see equation 2.4) unchanged. We include (in the electron case) an uncertainty of 0.0045 on $\sin^2\theta_W$ to account for calorimeter calibration non-linearity [‡] which could change the mass ratio.

First we combine the e and μ measurements separately using equation 2.4 and cancelling the correlated scale uncertainties (following equation 7.6) to get:

$$\sin^2\theta_W^e = 0.2344 \pm 0.0104, \tag{7.7}$$

and

$$\sin^2\theta_W^\mu = 0.2298 \pm 0.0135. \tag{7.8}$$

Properly treating the correlated uncertainties in equations 7.7 or 7.8 [§] we combine them and find:

$$\sin^2\theta_W^{\mathrm{CDF}} = 0.2327 \pm 0.0084. \tag{7.9}$$

[‡] Ws produce electrons with an average of 40 GeV of energy, while Zs produce 45 GeV electrons. Testbeam studies indicate that the calorimeter calibration is linear to 0.15% over this range of energy. We conservatively include an 0.3% uncertainty on the electron mass ratio.

[§] ± 0.002 of the uncertainty in equations 7.7 and 7.8 comes from W mass uncertainties common to the e and μ measurements.

	Case	1	2
	m_W	79.71 ± 0.42	80.04 ± 0.33
	m_Z	90.92 ± 0.35	91.10 ± 0.06
	$\sin^2\theta_W$	(0.233)	0.229 ± 0.007
m_H			
30.		90 ± 85	110 ± 55
100.		110 ± 75	130 ± 50
1000.		140 ± 70	155 ± 40

Table 7.2: $m_{\rm top}$ values consistent with each scenario and the prediction of the radiative corrections from the Minimal Standard Model. All masses are in units of GeV/c^2. In the first case the $\sin^2\theta_W$ shown is just that from the ratio of masses. No additional constraint on $m_{\rm top}$ is assumed for it. The $m_{\rm top}$ uncertainties quoted are one sigma values from the combined χ^2 fits. The two scenarios are discussed in the text.

Using equation 2.5 and figure 2.3 we can also extract the top quark mass consistent with the predictions of the Minimal Standard Model electroweak radiative corrections. Here again, we can proceed in several ways depending on how much information we incorporate from outside the CDF experiment.

The simplest is to use the CDF measurements alone. We minimize a χ^2 describing the Minimal Standard Model prediction for the radiative corrections as a function of m_W, m_Z, $\sin^2\theta_W$, $m_{\rm top}$ and $m_{\rm Higgs}$. These are only over-constrained within the context of the Minimal Standard Model. The columns of table 7.2 gives the best fit top quark mass for each of three choices of Higgs mass. We investigate two scenarios: 1) Using the CDF measurements alone (taking $\sin^2\theta_W$ from equation 7.9) and 2) using both the CDF and UA2 W mass measurements (taking the W mass from equation 7.4) and neutrino scattering measurements of $\sin^2\theta_W$ [65] ¶.

Table 7.2 shows that the constraints on the top quark mass are loose. They are consistent with CDF direct searches for the top quark in Standard Model decays [35, 40] which have ruled out $m_{\rm top} < 77$ GeV/c^2 (at the 95% C.L.). Taking the CDF measurement of the W

¶We take $\sin^2\theta_W = 0.229 \pm .007$ for the neutrino scattering result. This result depends very weakly on the top quark mass having different radiative corrections [17]. For simplicity we include it as a constraint independent of $m_{\rm top}$.

and Z masses (case 1) we find $m_{\rm top} < 280$ GeV/c^2 at the 95% C.L. , while incorporating the UA2 and neutrino scattering measurements (case 2) lowers this to $m_{\rm top} < 220$ GeV/c^2 at the 95% C.L. In both cases we set the limit on $m_{\rm top}$ using $m_{\rm Higgs} = 1$ TeV/c^2 to give an upper bound. From table 7.2 it is clear that no useful limit can be placed on the Higgs mass with these data.

In the future, it is expected that CDF will collect enough Ws and Zs to determine the W mass or the W/Z mass ratio directly with sufficient precision to measure $\sin^2\theta_W$ to ± 0.002. This will require 20$\times$ the data presently available, something which is planned over the course of the next two Tevatron runs, in the next five years. The methods described in this thesis can be extended with the larger statistics samples to improve on the detector calibration (E/P), neutrino systematics (by studying Z decays) and the statistical uncertainty on the fit. The goal is an overall W mass uncertainty of 100 MeV/c^2. The second phase of LEP, scheduled for 1994, will provide a comparable measurement of the W mass. At LEP the limitation will be W event statistics, since the W pair cross-section is 1 000 times smaller than the Z cross-section currently being explored at LEP.

Other tests of the electroweak Standard Model will take place during the first phase of LEP. The decay asymmetry of the Z and τ polarization in the decay $z \rightarrow \tau\tau$ should provide independent measurements of $\sin^2\theta_W$ with ± 0.001 accuracy. Each of these measurements require understanding electroweak radiative corrections (like those described in chapter 2) since they involve subtly different couplings in the Standard Model. If the top quark is not observed directly in the next five years, these measurements, taken together, should allow a 30 GeV/c^2 determination of $m_{\rm top}$ with the largest remaining uncertainty coming from the unknown Higgs mass.

Bibliography

[1] E. Fermi. Tentativo di una Teoria dei Raggia β. *Nuovo Cimento*, 11:1, 1934.

[2] S.L.Glashow. Partial-Symmetries of Weak Interactions. *Nuclear Physics*, 22:579, 1961.

[3] S. Weinberg. A Model of Leptons. *Physical Review Letters*, 19(21):1264, 1967.

[4] A.Salam. *Elementary Particle Theory*, page 367. Almqvist & Wiksell, Sweden, 1968.

[5] P.W. Higgs. Broken Symmetries and the Masses of Gauge Bosons. *Physical Review Letters*, 13:508, 1964.

[6] G. Arnison *et al.* (UA1 collaboration). Experimental Observation of Isolated Large Transverse Energy Electrons with Associated Missing Energy at $\sqrt{s}$ = 540 GeV. *Physics Letters*, B(122):103, 1983.

[7] F. Abe *et al.* (CDF collaboration). Measurement of W-Boson Production in 1.8-TeV $\bar{p}p$ Collisions. *Physical Review Letters*, 62(9):1005, 1989.

[8] G. Arnison *et al.* (UA1 collaboration). Intermediate Vector Boson Properties at the CERN Super Proton Synchrotron Collider. *Europhysics Letters*, 1(7):327, 1986.

[9] J. Incandela (UA2 collaboration). Recent Results of 1989 SppS running. In *Proceedings of the Division of Particles and Fields Meeting*, Houston, Tx. January 1990.

[10] E.D. Commins and P.H. Bucksbaum. *Weak Interactions of Leptons and Quarks*, chapter 3, page 102. Cambridge University Press, 1983.

[11] A. Blondel (CDHSW Collaboration) *et. al.* Electroweak Parameters from a High Statistics Neutrino Nucleon Scattering Experiment. Technical Report EP/89-101, CERN, 1989. Submitted to Z. Physik C.

[12] J. Blietschau *et al.* (Gargamelle Collaboration). Determination of the Neutral to Charged Current Inclusive Cross-Section Ratio for ν and $\bar{\nu}$ Interactions in the "Gargamelle" Experiment. *Nuclear Physics*, B(118):218, 1977.

[13] P. Wanderer *et al.* (HPWF Collaboration). Measurement of the Neutral Current Interactions of High-Energy Neutrinos. *Physical Review*, D(17):1679, 1978.

[14] F. Merritt *et al.* Neutral-Current Coupling in High-Energy Neutrino Interactions. *Physical Review*, D(17):2199, 1978.

[15] A. Sirlin. Radiative Corrections in the SU(2) x U(1) Theory: A Simple Renormalization Framework. *Physical Review*, D22(4):971, 1980.

[16] L. Hall. *Decoupling and Grand Unification.* PhD thesis, Harvard University, May 1981.

[17] P. Langacker. Implications of Recent $m_{W,Z}$ and Neutral Current Measurements for the Top-Quark Mass. *Physical Review Letters*, 63(18):1920, 1989.

[18] W. Marciano and A. Sirlin. Radiative Corrections to Neutrino-Induced Neutral-Current Phenomena in the SU(2) x U(1) Theory. *Physical Review*, D22(11):2695, 1980.

[19] S.L. Wu (ALEPH collaboration). Search for New Particles with ALEPH. In *Proceedings of the Division of Particles and Fields Meeting*, Houston, Tx. January 1990.

[20] V. Barger, J. Hewett, and T. Rizzo. Radiative Corrections to W, Z Masses. Technical Report MAD/PH/514, University of Wisconsin - Madison, 1989.

[21] E.L. Berger, F. Halzen, C.S. Kim, and S. Willenbrock. Weak Boson Production at Fermilab Tevatron Energies. *Physical Review*, D(40):83, 1989.

[22] G.Altarelli and R.K.Ellis and M.Greco and G.Martinelli. Vector Boson Production at Colliders: A Theoretical Reappraisal. *Nuclear Physics*, B(264):12, 1984. For a more recent non-calculation of this effect see also: Arnold and Reno, *NuclearPhysics* B(319):38,1989.

[23] P. Chiappetta and M. Le Bellac. Angular Distribution of Lepton Pairs in Drell-Yan-Like Processes. *Zeitschrift fur Physik*, C(32):521, 1986.

[24] L. Balka *et al.* The CDF Central Electromagnetic Calorimeter. *Nuclear Instruments and Methods*, A(267):272, 1988.

[25] F. Abe *et al.* (CDF Collaboration). The CDF Detector: An Overview. *Nuclear Instruments and Methods*, A(271):387, 1988.

[26] F. Snider *et al.* The CDF Vertex Time Projection Chamber System. *Nuclear Instruments and Methods*, A(268):75, 1988.

[27] F. Bedeschi *et al.* Design and Construction of the CDF Central Tracking Chamber. *Nuclear Instruments and Methods*, A(268):50, 1988.

[28] S. R. Hahn *et al.* Calibration Systems for the CDF Central Electromagnetic Calorimeter. *Nuclear Instruments and Methods*, A(267):351, 1988.

[29] S. Behrends *et al. Track Corrections to Jets and Jet Resolution.* CDF Note 1015.

[30] M. Franklin. Peformance of the Gas Calorimetry at CDF. In *Proceedings of the 7th Topical Workshop on Proton-Antiproton Collider Physics*, June 1988.

[31] D. Brown. *A Search for Multi-Parton Scattering at* $\sqrt{s} = 1.8$ *TeV.* PhD thesis, Harvard University, June 1989.

[32] D. Amidei *et al.* A Two Level FASTBUS Based Trigger System for CDF. *Nuclear Instruments and Methods*, A(267):51, 1988.

[33] G.W. Foster *et al.* A Fast Hardware Track-Finder for the CDF Central Tracking Chamber. *Nuclear Instruments and Methods*, A(269):93, 1988.

[34] H.J. Frisch. *Trigger Studies on W and Z Samples.* UC Analysis note #1, 1989.

[35] F. Abe *et al.* (CDF collaboration). Search for New Heavy Quarks in Electron-Muon Events at the Fermilab Tevatron Collider. *Physical Review Letters*, 64(2):147, 1990.

[36] L.Nodulman and W.Trischuk. *A Description of the 1988* $\not\!\!E_t$ *Triggers.* CDF Note 832.

[37] F. Abe *et al.* (CDF Collaboration). Limits on the Masses of Supersymmetric Particles from 1.8-TeV $p\bar{p}$ Collisions. *Physical Review Letters*, 62(16):1825, 1989.

[38] C. Campagnari, P. Derwent, P. Tipton, and B. Winer. *A Search for Heavy Top in the Inclusive W Sample.* CDF Note 922.

[39] M. Gold. *Identification of Conversion Electron Pairs.* CDF Note 913.

[40] F. Abe *et al.* (CDF Collaboration). Search for the Top Quark in the Reaction $p\bar{p} \rightarrow$ electron + jets at $\sqrt{s} = 1.8$ TeV. *Physical Review Letters*, 64(2):142, 1990.

[41] F. Abe *et al.* (CDF Collaboration). Measurement of the Ratio $\sigma(W \rightarrow e\nu)$ / $\sigma(Z \rightarrow ee)$ in $p\bar{p}$ Collisions. *Physical Review Letters*, 64(2):152, 1990.

[42] W. Trischuk *et al. A Determination of the CEM Energy Scale.* CDF Note 883.

[43] P. N. Schlabach. *W Mass Measurement with Muons at* $\sqrt{s} = 1.8$ *TeV.* PhD thesis, University of Illinois, August 1990. In preparation.

[44] F. Abe *et al.* (CDF Collaboration). Measurement of the Mass and Width of the Z^0 Boson at the Fermilab Tevatron. *Physical Review Letters*, 63(7):720, 1989.

[45] B. Adeva *et. al.* Determination of the Properties of the Neutral Intermediate Vector Boson Z^o. *Physics Letters*, B(231):509, 1989.

[46] D. Decamp *et. al.* Determination of the Number of Light Neutrino Species. *Physics Letters*, B(231):519, 1989.

[47] M. Akrawy *et. al.* Measurement of the Z^o Mass and Width with the OPAL Detector at LEP. *Physics Letters*, B(231):530, 1989.

[48] P. Aarnio *et. al.* The Mass and Width of the Z^o-Particle from Multihadronic Final States Produced in e^+e^- Annihilations. *Physics Letters*, B(231):539, 1989.

[49] K. Yasuoka *et al.* Response Maps of the CDF Central Electromagnetic Calorimeter with Electrons. *Nuclear Instruments and Methods*, A(267):315, 1988.

[50] J. Proudfoot. Electron Identification in the CDF Central Calorimeter. In *Proceedings of the Workshop on Calorimetery for the SSC*, Tuscaloosa, AL. March 1989.

[51] R. G. Wagner. Unpublished, based on calculations by F. Berends. *et al.*, Z. Phys. C (27):155, 1985; F. Behrends and R. Kleiss, Z. Phys. C (27):365, 1985.

[52] B.Flaugher and S.Kuhlmann. *Underlying Event Energy in Clusters.* CDF Note 685. See also CDF583, and CDF883.

[53] W.Trischuk and L.Nodulman. $1988-89\,\not\!\!E_t$ *Centering and Resolution.* CDF Note 948.

[54] C. Campagnari. *A Fast W and Z Monte Carlo.* CDF Note 1025.

[55] R.N. Cahn. Analytic Forms for the e^+e^- Annihilation Cross Section Near the Z Including Initial-State Radiation. *Physical Review D*, 36(9):2666, 1987.

[56] F. James and M. Roos. *Function Minimization and Error Analysis*, 1983. CERN Program Library Documentation.

[57] W. Press, B. Flannery, S. Teukolsky, and W. Vetterling. *Numerical Recipes*, chapter 3, pages 97–101. Cambridge University Press, 1986.

[58] E. Eichten, I. Hinchliffe, K. Lane, and C. Quigg. Supercollider Physics. *Reviews of Modern Physics*, 56:579, 1984.

[59] D. Duke and J. F. Owens. Q^2-Dependent Parameterizations of Parton Distribution Functions. *Physical Review*, D(30):49, 1984.

[60] M.Diemoz, F.Ferroni, E.Longo, and G.Martinelli. Parton Densities from Deep Inelastic Scattering to Hadronic Processes at the Super Collider. *Z. Phys.*, C(39):21, 1988.

[61] A.D. Martin, R.G. Robert, and W.J. Stirling. Structure Function Analysis and ψ, Jet, W, and Z Production. *Physical Review*, D(37):1161, 1988.

[62] J. Nassalski. New parton distribution function measurements. In *Proceedings of the Europhysics 1989 Conference*, September 1989.

[63] J. Stirling. Parton Distribution Uncertainty in the Measurement of m_W in $p\bar{p}$ Collisions. Technical Report DTP/89/50, University of Durham, October 1989.

[64] F. Paige and S.D. Protopopescu. Technical Report BNL 38034, Brookhaven National Laboratory, 1986. (unpublished).

[65] U. Amaldi *et al.* Comprehensive Analysis of Data Pertaining to the Weak Neutral Current and the Intermediate-Vector-Boson Masses. *Physical Review*, D(36):1385, 1987.